

Title	Statistical analysis of positron emission tomography data
Authors	Mou, Tian
Publication date	2018
Original Citation	Mou, T. 2018. Statistical analysis of positron emission tomography data. PhD Thesis, University College Cork.
Type of publication	Doctoral thesis
Rights	© 2018, Tian Mou. - <a href="http://creativecommons.org/licenses/by-nc-nd/3.0/">http://creativecommons.org/licenses/by-nc-nd/3.0/</a>
Download date	2023-05-05 20:17:22
Item downloaded from	<a href="http://hdl.handle.net/10468/6282">http://hdl.handle.net/10468/6282</a>



# UCC

**University College Cork, Ireland**  
Coláiste na hOllscoile Corcaigh

# Statistical Analysis of Positron Emission Tomography Data

Tian Mou

**Thesis submitted for the degree of  
Doctor of Philosophy**



NATIONAL UNIVERSITY OF IRELAND, CORK

DEPARTMENT OF STATISTICS

May 2018

Supervisors: Dr. Jian Huang  
Prof. Finbarr O'Sullivan

Head of Department: Dr. Michael Cronin



# Contents

List of Figures . . . . .	iv
List of Tables . . . . .	viii
Acknowledgements . . . . .	xi
<i>Abstract</i> . . . . .	xii
<b>1 Thesis Introduction and Overview</b>	<b>1</b>
1.1 Introduction . . . . .	1
1.2 Main Contributions . . . . .	2
1.3 Structure of the Thesis . . . . .	3
<b>2 Background</b>	<b>4</b>
2.1 Medical Imaging Modalities . . . . .	4
2.1.1 Morphological Imaging . . . . .	5
2.1.2 Functional Imaging . . . . .	8
2.1.3 Hybrid Imaging Modalities . . . . .	10
2.2 Positron Emission Tomography . . . . .	13
2.2.1 History . . . . .	13
2.2.2 The Physics of PET . . . . .	14
2.2.3 Image Reconstruction . . . . .	16
2.2.4 Radiotracers . . . . .	18
2.3 Noise in PET Image . . . . .	19
2.3.1 The Poisson Nature of Emission Process . . . . .	19
2.3.2 Sources of Noise in PET Image . . . . .	20
<b>3 Spatial Statistical Characteristics in Clinical PET scanners</b>	<b>23</b>
3.1 Background . . . . .	23
3.1.1 PET Scanner Quality Assurance . . . . .	23
3.1.2 Uniform Cylindrical Phantom . . . . .	23
3.1.3 ACRIN Data . . . . .	24
3.2 Empirical Analysis of Spatial Characteristics of 3-D PET Image	25
3.2.1 Introduction . . . . .	25
3.2.2 Methodology . . . . .	26
3.2.3 Results . . . . .	27
3.3 Conclusions . . . . .	30
<b>4 The Gamma Characteristic of Reconstructed PET Data</b>	<b>32</b>
4.1 Introduction . . . . .	32
4.1.1 Gamma Distribution . . . . .	34
4.1.2 Likelihood Ratio Test . . . . .	36
4.1.3 Preliminary Analysis with ACRIN Series . . . . .	37
4.2 Methodological Development . . . . .	38
4.2.1 Inference for Multiplicative Models in the Gamma Setting	39
4.2.2 Probability Transformed Normalised Residuals . . . . .	43
4.3 Experimental Methods . . . . .	44
4.3.1 Physical Phantom Data . . . . .	44



4.3.2	Numerical Phantom Study . . . . .	48
4.3.3	Numerical Simulation with the Gamma Model . . . . .	48
4.4	Results . . . . .	48
4.4.1	Physical Phantom Data . . . . .	48
4.4.2	Numerical Phantom Simulation . . . . .	51
4.4.3	Numerical Simulation with the Gamma Model . . . . .	52
4.5	Discussion . . . . .	53
4.5.1	Theoretical Interpretation of MSE Characteristics . . . . .	54
4.5.2	Discriminating Between the Log-normal and Gamma Dis- tributions . . . . .	56
4.5.3	Generalisability to Other PET Scanners . . . . .	58
4.5.4	Implication of Gamma Model for Kinetic Modelling . . . . .	58
4.6	Concluding Remarks . . . . .	60
<b>5</b>	<b>Spatial Auto-correlation and Simulation Analysis</b>	<b>62</b>
5.1	Introduction . . . . .	62
5.1.1	Auto-correlation Function . . . . .	64
5.1.2	Inconsistency of Least Squares Estimation for Spatial Au- toregressive Model . . . . .	66
5.2	Methodological Development . . . . .	67
5.2.1	Spatial Autoregressive Model . . . . .	68
5.2.2	Estimation of SAR Model Coefficients Using Likelihood- based Approach . . . . .	69
5.2.3	Computational Considerations . . . . .	71
5.2.4	Validation of the Likelihood-based Estimation Using 1-D Simulation . . . . .	71
5.2.5	Neighbourhood Structure . . . . .	72
5.2.6	Simulation of PET Data . . . . .	72
5.3	Experimental Methods . . . . .	73
5.3.1	Normalised Physical Phantom Data Analysis . . . . .	73
5.3.2	SAR Model Simulation . . . . .	76
5.3.3	Numerical Phantom Simulation . . . . .	76
5.4	Results . . . . .	77
5.4.1	Physical Phantom Data . . . . .	77
5.4.2	SAR Model Simulation . . . . .	77
5.4.3	Numerical Phantom Simulation . . . . .	78
5.4.4	Impact of Spatial Covariance . . . . .	83
5.5	Concluding Remarks . . . . .	87
<b>6</b>	<b>Discussion, Conclusions and Future Work</b>	<b>88</b>
6.1	Discussion . . . . .	88
6.2	Conclusions . . . . .	92
6.3	Future Work . . . . .	92
6.3.1	Generalisation to other medical imaging modalities . . . . .	92
6.3.2	Generalisation to non-uniform PET images . . . . .	93
6.3.3	Using SAR model to analysis the auto-correlation structure in FBP reconstructed PET data . . . . .	93

6.3.4	Explore the robustness of the methods . . . . .	93
6.3.5	Explore alternative parametrizations . . . . .	94
<b>A</b>	<b>List of Publications and Presentations by the Author</b>	<b>96</b>
A.1	Conference Proceedings related to Chapter 3 . . . . .	96
A.2	Publications related to Chapter 4 . . . . .	96
A.3	Publications related to Chapter 5 . . . . .	96
A.4	Other Publications . . . . .	97
A.5	Conference Presentations . . . . .	97
<b>B</b>	<b>R code</b>	<b>100</b>
	<b>Nomenclature</b>	<b>128</b>
	<b>Bibliography</b>	<b>B1</b>

## List of Figures

2.1	(a) CT scanner, GE Brivo CT325. (b) Chest CT (lung window) in a patient with lung tumour in red circle <sup>1</sup> . . . . .	6
2.2	(a) MRI scanner, Optima <sup>TM</sup> MR450w GEM-70cm. (b) MRI image of a brain showing a pituitary tumour <sup>2</sup> . . . . .	8
2.3	The example of EEG and ECG images. . . . .	8
2.4	(a) SPECT scanner, Siemens Symbia <sup>TM</sup> S. (b) SPECT image showing normal brain activity <sup>3</sup> . . . . .	10
2.5	PET/CT scan generated on a GE Advance scanner of a lung cancer patient <sup>4</sup> , showing from left to right, transverse, coronal and sagittal view in AMIDE [61]. The tumour was indicated by the arrows. .	11
2.6	Schematic of PET scan procedure. Left: Illustration of the annihilation process of a positron and an electron. Middle: Detection of both 511 keV photons in coincidence by the ring detector array in PET camera [60]. Right: Signal collecting and processing procedure. . . . .	15
2.7	Schematic of a block detector (left) and a ring of a PET scanner (right) <sup>5</sup> . . . . .	15
2.8	Illustration of the filtered backprojection computation process. .	16
2.9	Conceptual illustration of iterative image reconstruction methods.	17
3.1	Illustration of uniform cylindrical phantom. . . . .	24
3.2	Sample Phantom data in the ACRIN set. . . . .	25
3.3	Estimated temporal ( $\sigma_t$ ), axial ( $\sigma_k$ ) and radial ( $\sigma_r$ ) bias and standard deviations (SD) in the PET measurement. $\sigma_t$ is adjusted for effects of frame duration and isotope decay. . . . .	27
3.4	Left: Boxplots of the distribution of voxel-level $z$ -data classified by acquisition time (top), axial (middle) and radial position (bottom). Right: Boxplots of the distribution of normalised data. . . . .	28
3.5	Top: Estimated transverse and axial autocorrelation functions (ACF). The red and green lines in the transverse ACF represent autocorrelation in the row, column directions. Bottom left: Histogram of the standardised data and comparison with normal quantiles (blue). Bottom right: Histogram of square root transformed data classified by time and axial position. . . . .	29
3.6	Estimated axial ( $\sigma_k$ ) and radial ( $\sigma_r$ ) bias and standard deviation for 28 sites classified by 2 different manufacturers. (21 GE, 7 Siemens) Small plots: Average bias and SD for GE and Siemens scanners.	30
3.7	Boxplots of trans axial and axial autocorrelation on lag 2 to 9. .	31
4.1	A uniform cylindrical phantom in PET/CT scanner. . . . .	34
4.2	Reconstructed images from the uniform phantom. . . . .	35
4.3	Densities of $\text{Gamma}(\tau, 1/\tau)$ for different $\tau$ -values. . . . .	35
4.4	Gamma and Normal model fits for ACRIN physical phantom data.	37

4.5	Kolmogorov–Smirnov test $p$ -values of 43 ACRIN sets. . . . .	38
4.6	Theoretical probability transformation of a Gamma random variable ( $Z$ ) with distribution function $F$ to a Normal random variable $R$ . . . . .	43
4.7	3D dynamic PET study on a cylindrical phantom using FBP ( <b>A,C</b> ) and EM (IR) ( <b>B,D</b> ) reconstructed methods. The ROI data within white outline are used in analysis. <b>Figure A and B:</b> Left: The cross-section and sagittal image of the phantom data (24th time frame of slice 23). Right: Histograms generated from ROIs on different time frames and slices. The lines on the plots are Gamma (red), Log-normal (green) and Normal (blue) model fits for particular time and slice combinations of ROI data. <b>Figure C and D:</b> Top: $\chi^2_2$ $p$ -values (log-scale) calculated for each time and slice combinations and plotted by time frame and slice location. The green lines indicate the significant level—0.05. Bottom: Histograms and normal Q-Q plots of Pearson residuals (left blue) and normalised Gamma residuals (right red) for entire phantom data. . . . .	45
4.8	Multiplicative model fit on FBP ( <b>A,C</b> ) and EM (iterative) ( <b>B,D</b> ) reconstructed PET data. <b>Figure A and B:</b> Multiplicative model estimates of bias and variance using Least Square (LS) versus Maximum Likelihood (ML) estimation. <b>Figure C and D:</b> show multiplicative model residuals and the Q-Q plot of normalised Gamma residuals with and without the multiplicative constraint. . . . .	47
4.9	Results of numerical phantom simulation study. Top: Phantom image and EM reconstructed images for two count rates ( $N = 10^5$ and $N = 10^6$ ). Middle and bottom: Histograms of pixel values for different count rates. The Gamma and Log-normal model fits are shown in red and green, respectively. . . . .	51
4.10	Histograms and normal Q-Q plots (dots) of the Pearson (top) and Gamma-transformed residuals (bottom) for different $\tau$ values. . . . .	52
4.11	Initial (LS) and multiplicative (ML) estimates for $\mu_t$ , $\alpha_k$ , $\phi_t$ and $\beta_k$ when $\tau = 1$ . . . . .	54
4.12	The log MSE of the parameter estimation evaluated as function of dose $\tau$ and ROI size $N$ . The log MSE for initial (LS) estimates are shown in blue and multiplicative model (ML) estimates are shown in red. . . . .	55
4.13	The likelihood ratio of Gamma model compare to Log-normal. Choose the Gamma distribution if the value is greater than 1, otherwise the Log-normal distribution is preferred. . . . .	57
4.14	The Kolmogorov-Smirnov test $p$ -values of Gamma and Normal model for numerical phantom simulation data with different iteration numbers (4, 16, 64) and counts (1e+5, 5e+5, 1e+6). . . . .	60

5.1	Top: Estimated transverse and axial auto-correlation functions (1-D ACF) for iterative reconstructed phantom data. The red and green lines in the transverse plot represent auto-correlation in row and column directions, respectively. Bottom: 3-D ACF for the same phantom. 1-D profiles through the centre of the phantom, showing from left to right, horizontal, vertical, and axial profile.	65
5.2	Top: Time series generated from the 1-D spatial AR(2) model. Bottom: Least squares auto-regression estimation results. . . . .	67
5.3	Results of likelihood-based estimation of 1-D simulation data. .	72
5.4	Diagram of first (red) and second (blue) order neighbours for a selected voxel (black) with a set of coefficients for each neighbour.	73
5.5	Graphical representation of the PET analysis and simulation process	74
5.6	Top: The transverse and sagittal image of 3-D dynamic PET study on a cylindrical phantom using iterative (3D-IR) reconstructed methods (24th time frame of slice 23). The ROI data within white outline are used in analysis. On the right is the histogram of the data generated from ROIs. Bottom: Images and histogram of the probability transformed/normalised data generated by the previous study. . . . .	75
5.7	3-D ACF of the ROI data shown in the top of Fig. 5.6 . . . . .	76
5.8	Top: Comparison between the ACF of reconstructed PET phantom data and the modelled ACF. Bottom: 3-D ACF patterns of SAR model residuals. . . . .	78
5.9	Comparison of the 3-D ACF between the physical phantom data and the model simulated data on each direction. . . . .	79
5.10	Log mean squared errors (MSE) of the estimated parameters based on simulation study with different sample sizes (20 repetitions for each size). $N_0$ corresponds to the size of the phantom ROI in the CUH data. . . . .	79
5.11	Images of the VSK phantom and EM reconstructed VSK phantom (top row). Image and one dimensional profiles of 2-D ACF of the normalised EM reconstructed VSK phantom (middle row). Image and one dimensional profiles of 2-D ACF of the fitted SAR model residuals (bottom row). The 2-D ACF were assessed for each replicate. Shown is the averaged ACF over 20 replicates. .	80
5.12	Images of the uniform phantom and EM reconstructed uniform phantom (top row). Image and one dimensional profiles of 2-D ACF of the normalised reconstructed uniform phantom (middle row). Image and one dimensional profiles of the fitted SAR model residuals. The 2-D ACF were assessed for each replicate. Shown is the averaged ACF over 20 replicates. . . . .	81
5.13	Images of average $\mu(n)$ and $\phi(n)$ based on 1,000 simulation studies involving the VSK and uniform phantom. . . . .	82

5.14	Estimated the SAR model parameters of the normalised EM reconstructed VSK phantom (blue and red) and uniform phantom (green) based on 1,000 simulation studies involving different count levels. . . . .	82
5.15	Top: 3-D ACF of FBP and IR physical phantom. Bottom: One dimensional profiles of 3-D ACF of FBP and IR reconstruction physical phantom images through the centre of the phantom, showing from left to right, horizontal, vertical and axial profile. . . . .	83
5.16	Parameter estimation for <i>i.i.d.</i> simulation versus correlated simulation. . . . .	84
5.17	The log MSE of the parameter estimation for auto-correlated data evaluated as a function of dose $\tau$ and ROI size $N$ . The log MSE for initial (LS) estimates are shown in blue and multiplicative model (ML) estimates are shown in red. . . . .	85
6.1	The Kolmogorov-Smirnov test $p$ -values of Gamma and Log-normal model for numerical phantom simulation data with different iteration numbers (4, 16, 64) and counts (1e+5, 5e+5, 1e+6). . . . .	90
6.2	Top: Estimated transverse and axial autocorrelation functions (1-D ACF) for FBP reconstructed phantom data. The red and green lines in the transverse plot represent auto-correlation in row and column directions, respectively. Bottom: 3-D ACF for the same phantom. 1-D profiles through the centre of the phantom, showing from left to right, horizontal, vertical, and axial profile. . . . .	94
6.3	Gamma model estimation result for Gaussian simulated data with corresponding mean squared error for each estimate. . . . .	95

## List of Tables

2.1	The most commonly used radioisotopes in PET, adapted from [58].	19
3.1	Analysis of Axial, Radial and Temporal bias and standard deviations . . . . .	28
4.1	Empirical MSE estimation characteristic for $\mu_t$ and $\alpha_k \log(\text{MSE}) \sim a_0 + a_1 \log(N) + a_2 \log(\tau)$ . . . . .	53
4.2	Empirical MSE estimation characteristic for $\phi_t$ and $\beta_k \log(\text{MSE}) \sim a_0 + a_1 \log(N) + a_2 \log(\tau)$ . . . . .	53
5.1	Non-linear Regression Coefficients . . . . .	77

I, Tian Mou, certify that this thesis is my own work and has not been submitted for another degree, either at University College Cork or elsewhere. All external references and sources are clearly acknowledged and identified within the contents. I have read and understood the regulations of University College Cork concerning plagiarism.



*Tian Mou*



*This thesis is dedicated to my beloved parents.*

## Acknowledgements

First and foremost, I would like to express my sincere gratitude to my supervisors Dr. Jian Huang and Prof. Finbarr O’Sullivan for their continuous support of my Ph.D. study. I would like to thank Jian for introducing me to the world of biomedical imaging and for encouraging me to do scientific research. It has been a great honour to be his first Ph.D. student. He has been a tremendous mentor for me not only in research but also every aspect in my life. I also would like to thank Finbarr for giving me this opportunity to join his project. His patience, enthusiasm and immense knowledge made my Ph.D. journey unforgettable, enjoyable and valuable.

I would like to thank my external examiner Prof. Maria Luz Durbàn Reguera and internal examiner Dr. Tony Fitzgerald for brilliant suggestions and insightful comments.

I would especially like to thank our local collaborators in Cork University Hospital and Alliance Medical for providing PET images and medical support, thanks to Peter Murphy, Kevin O’Regan, Stephen Stone and Nicola Hughes. Appreciation should also be given to our oversea collaborators at University of Washington for providing ACRIN data which allows me to do cross-centre research as discussed in chapter 3, thanks to Mark Muzi, Paul Kinahan and Adam Opanowski.

The members of the diagnostic imaging group have contributed immensely to my personal and professional time at UCC. We have a friendly, loving, supportive working environment which made my life and work here so enjoyable and productive. I’m grateful to all the past and present group members that I have had the pleasure to work with, they are Eric Wolsztynski, Janet O’Sullivan, Francisco Hernandez-Fernandez, Sarah Murphy, Zhaoyan Xiu, Fengyun Gu, Ran Ren, Xianguyu Meng, David Hawe and Yanhui Zhang. I would also like to thank Michael Cronin for teaching me modelling courses. Many thanks to the colleagues who are or have been working in the lab 2.11 WGB, in particular Paula Harrison, Anthony Joseph Sheerin and Aodhán Francis O’Leary for their kindly help.

A special thanks goes to my boyfriend Fanghui Fan for his support, time, love, and especially the encouragement for helping me to overcome the difficulties during the past four years.

Finally, I would like to thank my beloved parents for their love and selfless dedication. They raised me with a love of science and supported me in all my pursuits. Thank you.

Tian Mou  
Stockholm  
May, 2018

## Abstract

*Positron emission tomography (PET) is a noninvasive medical imaging tool that produces sequences of images describing the distribution of radiotracers in the object. PET images can be processed to evaluate functional, biochemical, and physiological parameters of interest in human body. However, images generated by PET are generally noisy, thereby complicating their geometric interpretation and affecting the precision. The use of physical models to simulate the performance of PET scanners is well established. Such techniques are particularly useful at the design stage as they allow alternative specifications to be examined. When a scanner is installed and begins to be used operationally, its actual performance may deviate somewhat from the predictions made at the design stage. Thus it is recommended that routine quality assurance (QA) measurements could be used to provide an operational understanding of scanning properties. While QA data are primarily used to evaluate sensitivity and bias patterns, there is a possibility to also make use of such data sets for a more refined understanding of the 3-D scanning properties. Therefore, a comprehensive understanding of the noise characteristics in PET images could lead to improvements in clinical decision making.*

*The main goals of this thesis are to develop model-based approaches for describing and evaluating the statistical properties of noise and a practical approach for simulation of an operational PET scanner. We began with the empirical analysis of statistical characteristics—bias, variance and correlation patterns in a series of operational scanning data. A multiplicative Gamma model had been developed for representing the structure of reconstructed PET data. The novel iteratively re-weighted least squares (IRLS) techniques were proposed for the model fitting. These included the use of a Gamma-based probability transform for normalising residuals, which could be used for model diagnostics. Building on the Gamma based modelling and probability transformation, we developed a 3-D spatial autoregressive (SAR) model to represent the 3-D spatial auto-covariance structure within the normalised data. Auto-regressive coefficients were also estimated based on the minimisation of difference between 3-D auto-correlations calculated from the normalised data and model. Both traditional filtered back-projection (FBP) and expectation-maximisation (EM) reconstructions were considered. Numerical simulation studies were carried out to evaluate the performance of the above models.*

*The proposed models led to a very trivial process for simulation of the scanner—one that can be implemented in R. This provided a very practical mech-*

*anism to be routinely used in clinical practice—assessing error characteristics associated with quantified PET measures. Moreover, this fast and simplified approach has a potential usage in enhancing the quality of inferences produced from operational clinical PET scanners.*

# Chapter 1

## Thesis Introduction and Overview

### 1.1 Introduction

Medical imaging is the technique of revealing internal structures of a body which is often thought of viewing anatomical structures, *e.g.*, computed tomography (CT), however, medical imaging also includes the imaging of physiologic function rather than anatomy, *e.g.*, positron emission tomography (PET) [79]. PET is a nuclear medical imaging modality which detects positron emitted photons and produces tomography images of a subject. In recent years, PET seems to become the most advanced application of nuclear medical imaging and no other imaging technique can be compared. It has been widely used in the clinical management in oncology, cardiology and neurology. Normally, a PET scan starts with the injection of radio-labelled molecules (radiotracer) into a subject, this is followed by the detection and imaging of the tracer distribution [96]. Depending on the biological property of the injected radiotracer, PET is quite versatile as the various clinical processes can be considered in PET study. Unlike the morphological imaging techniques, PET measures the metabolic processes of the body in vivo. These measurements are derived from the reconstructed images which describe the distribution of the injected tracer. The images are displayed as a series of 2-D cross-sectional images. The noise level in PET images is relatively higher due to the lower radiation dose used compared to CT [44]. The noise behaviours in the PET images are also affected by many factors such as machine type, correction procedures, reconstruction methods, injection dose, and etc [88, 109]. The high magnitude and the unknown structure of noise limit the utilisation of PET technique.

The PET or PET/CT imaging centres have been spread all over the world.

The number of PET related sites is large and continues to grow. There is an extensive literature on the use of physical models to simulate the performance of PET scanners. Often these techniques are particularly useful at the design stage, allowing innovations in various aspects to be examined. When a scanner is installed and begins to be used operationally, its actual performance may deviate from the predictions made by the physical simulation model. Thus it is recommended that routine quality assurance (QA) measurements be used to provide an operational understanding of scanning properties. Phantom study is one of the most common and important measurement assessing imaging quality of PET scanners. The data used in this thesis are uniform cylindrical phantom data obtained either from the American College of Radiology Imaging Network (ACRIN) [98] or a local hospital—Cork University Hospital (CUH). While phantom data are typically used to evaluate sensitivity and bias patterns, there is a possibility to make more elaborate use of such data sets in order to develop an empirical representation of scanning.

This thesis aims to understand in a profound way how to describe the non-Gaussian nature of PET data and based on that understanding develop frameworks and methods for estimation of bias and variance as well as the 3-D spatial auto-covariance in PET imaging, and thus develop a practical approach for simulation of an operational PET scanner. We provide a statistical point of view in analysing the performance of PET scanners, make the sophisticated use of QA data and hopefully enhance the quality of inferences produced from operational clinical scanners.

## 1.2 Main Contributions

The main contributions of this thesis are as follows:

- The quality variation in the reliability of PET data has been demonstrated across many PET centres and scanners.
- The applicability of Gamma distribution for representing PET measurements has been investigated.
- An Gamma model based approach to estimate local bias and variance in an operational scanner has been developed and the method is demonstrated and evaluated by using both QA data and numerical simulation study.
- We construct a 3-D spatial auto-regressive model to represent the auto-covariance structure of PET measurements.

- Our work provides a very practical mechanism for routinely generating some assessments of error characteristics associated with quantified PET measures.
- R [86] programme to implement the above analysis has been developed.

## 1.3 Structure of the Thesis

This thesis is structured as follows: Chapter 2 is an introductory review of medical imaging tools, PET technique and image noise. In Chapter 3, general noise—bias, variance and spatial correlation are discussed using empirical method, a collection of 3-D PET scanners are considered. Chapter 4 provides a multiplicative Gamma model to represent reconstructed PET data and discusses the model fitting in detail. Chapter 5 considers a spatial auto-regressive model to analyse the spatial autocorrelation structure of the noise in PET images. Finally, the results of this thesis are discussed in Chapter 6, followed by the perspectives for future work.

# Chapter 2

## Background

### 2.1 Medical Imaging Modalities

Medical imaging is the technique and process of creating visualisation of body parts, tissues, or organs, for use in clinical diagnostics, medical intervention and disease monitoring. The aim of this technique is to produce images noninvasively of the internal structures of human body. In modern medicine, medical imaging has achieved a great progress. Over the years, many kinds of medical imaging have been developed, such as X-ray, computed tomography (CT), magnetic resonance imaging (MRI), ultrasound imaging and positron emission tomography (PET), each with their own clinical or medical purposes and applications. Up to 2010, more than 5 billion medical imaging investigations had been conducted worldwide [92]. The increase use of medical imaging has undoubtedly been of patient benefit. Today, accurate diagnostics and appropriate treatment decisions are highly rely on these technologies, without them, both diagnosis and treatment can be very difficult to achieve with any level of accuracy.

Although this thesis is focus on PET, it is worthwhile to discuss some other medical imaging modalities before discussing PET. It would be helpful to understand the importance and particularity of PET. This section begins with describing some of the most widely used medical imaging modalities and then emphatically introduces PET scan. Most of the medical imaging techniques could be classified into two types—morphological and functional. The morphological imaging focuses on the representation of the body’s structures while the functional imaging detects and measures the changes in metabolism, blood flow, etc. We will first discuss the morphological imaging techniques, *e.g.*, CT and MRI, which are in contrast to the functional imaging techniques, *e.g.*, SPECT and PET.



### 2.1.1 Morphological Imaging

Back to the end of the 19<sup>th</sup> century, seeing the skeleton of a living person was unexpected and beyond world's imagination until Wilhelm Röntgen showed his first X-ray image of his wife's hand [31]. This was an explosive news and directly made him become the first winner of Nobel Prize in physics. Since three months after his announcement, the use of X-ray in medical imaging continues to this day. Nowadays, when people talk about X-ray scan, it often refers to projectional radiography which produces two-dimensional images using X-ray radiation and involves examining the amount of X-rays reaching the detector. Different body parts have different effect of attenuation on X-rays. Depending on tissue density, each tissue absorbs varying degrees of radiation, producing different shadows on the image. For example, bones may absorb more of the radiation and thus, appear whiter on the image, while the lung tissue is mostly composed of air and results in darker appearance. Traditional plain X-rays are very useful in the detection of skeleton system, lung diseases as well as bowel diseases, but they are less useful in the imaging of brain or muscle. Although X-ray is the cheapest, the most convenient and widely used method in the world, it still has some weaknesses such as exposure to radiation and limitation of diagnostic accuracy.

## Computed Tomography

Since the traditional plain X-rays generate images as a projection of human body, overlapping tissues are hard to distinguish in this technique. To get a better look inside the body without the interference from different organs and tissues, computed tomography (CT) was invented independently by Sir Godfrey Hounsfield and Dr. Alan Cormack, both of whom awarded the Nobel Prize in 1979 [31]. CT scans take the transmission readings of X-rays through the body at multitude of angles, calculate the absorption values from these readings and present cross-sectional images (slices) of the body on a computer [42], see Figure 2.1. Modern CT scanners allow this 2-D tomographic data to be represented in volumetric (3-D) objects of patient body, see Figure 2.5 (b) as an example.

By the nature of CT, it involves larger radiation doses than plain X-rays and provides higher resolution images with improved anatomical details in two or three dimensions. One of the main advantages of CT compared to the other medical imaging techniques is the low structural noise magnitude in the images. This reduction in noise and efficient dose utilisation has made the visualisation of low-contrast objects (similar density) a reality [30]. Therefore, CT is widely used all



Figure 2.1: (a) CT scanner, GE Brivo CT325. (b) Chest CT (lung window) in a patient with lung tumour in red circle<sup>1</sup>.

around the world and the application areas are varying from emergency medicine to cancer diagnosis, such as detection of broken bones in head, heart diseases, abdominal diseases and lung cancer. The use of CT has increased rapidly, there are more than 62 million CT scans obtained in the United States every year [14].

Although CT is a fast and accurate medical imaging method, it has some drawbacks and limitations. It can be misinterpreted, for example, it is difficult to distinguish pathological and healthy structures especially in bones [32]. Another considerable issue is that the exposure of radiation and then raising the risk of radiation induced cancer—one abdominal CT scan gives an equivalent radiation dose to at least 50 conventional abdominal X-ray examinations [14]. Many patients even need to undergo several CT scans in the same day. Thus, the problem of how to reduce the dose of CT examinations without sacrificing accuracy has been a great challenge for both clinicians and manufacturers. Some analyses associated with the radiation exposure of CT show that the use of CT is related to a nonnegligible risk of radiation induced cancer, especially for women and children [28, 66, 32, 14, 92]. The radiation problem of CT scan should be considered more carefully when selecting patients and examining scan protocols.

Since CT provides high resolution images and accurate anatomic information within the body, the combination of CT and other functional imaging techniques is used which allows the information from two different exams to be correlated and interpreted on one image, for example, single photon emission computed tomography/computed tomography (SPECT/CT) and positron emission tomography/computed tomography (PET/CT). The combined (hybrid) imaging techniques will be introduced in 2.1.3 except SPECT/CT which is less relevant to

<sup>1</sup>Case contributed by Prof. Xiuhua Guo, Capital Medical University, Beijing, China.

this thesis and thus the reader is refer to [64] for more information.

## Magnetic Resonance Imaging

Nuclear magnetic resonance (NMR) also called magnetic resonance (MR) is a type of medical imaging that works without using ionising radiation and has specific uses in the diagnosis of disease. The basic principles of NMR spectroscopy are described by Friebolin [33] as a bio-magnetic nuclear spin imaging technology which has been developed rapidly in the last two decades. When a subject is placed in the strong magnetic field in an NMR system, it is irradiated with appropriate electromagnetic waves to change the rotational direction of hydrogen atoms, and the released electromagnetic signals are processed to form an image of the subject. The contrast between different types of tissue is determined by the relaxation time—the time it takes of excited atoms to return to equilibrium. A picture of MRI scanner and a brain MRI image are shown in Figure 2.2.

MRI is superior to CT in the scanning and detection of abnormalities in the brain, spine, joints and other soft tissue body parts. More importantly, this imaging technique avoids radiation exposure to the patient which averts the radiation problem described in the previous section. However, the disadvantages of MRI scan can not be ignored. MRI scans are more expensive than CT scans and the acquisition time is longer which leads to an issue of patient's comfort. Furthermore, some disturbing factors such as motion artefacts and hardware artefacts, could cause blurring of the entire image [88]. Additionally, MRI scanning is not applicable for patients with some metal implants.

Another limitation of MRI is that it provides little functional information of the subject. This could be remedied by combining MRI with an functional imaging modality such as PET. However, PET/MRI is not commonly used in clinical diagnoses because of technical difficulties and high expenses. A brief introduction of PET/MRI is given in 2.1.3. Another functional imaging technique using MRI technology is functional MRI (fMRI) which was developed to visualise neural activity in the brain [78]. Due to the special and complex structures of the human brain, imaging of the activities in brain was quite challenging until fMRI appears. It is a functional neuroimaging procedure using MRI technology to detect changes of blood flow in the brain which relies on the fact that the blood flow is associated with brain activity [48]. As the development of science and technology, an increasing number of functional imaging modalities are invented for various purposes. Some representative modalities of functional imaging will be introduced in the following section.

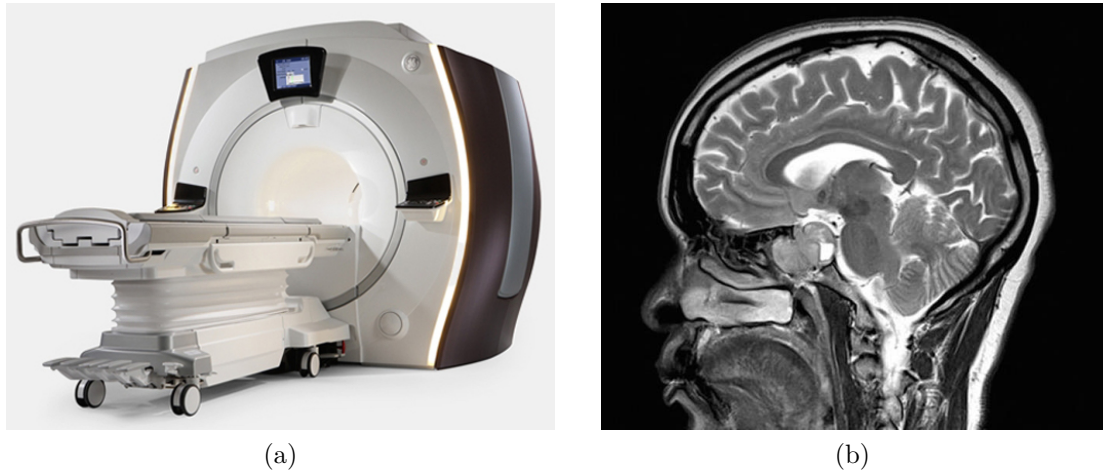


Figure 2.2: (a) MRI scanner, Optima™ MR450w GEM-70cm. (b) MRI image of a brain showing a pituitary tumour<sup>2</sup>.

### 2.1.2 Functional Imaging

As opposed to morphological imaging, functional imaging is focused on detecting physiological activities within a human tissue or organ, such as Electroencephalography (EEG), Electrocardiography (ECG), functional Magnetic Resonance Imaging (fMRI), Positron Emission Tomography (PET), Single Photon Emission Computer Tomography (SPECT), and etc.

EEG [75] records the electrical impulses of the brain by using electrodes attached to the scalp and ECG [41] records the electrical activity of the heart by using electrodes placed on the skin. These two techniques are quite different to the medical imaging modalities described in 2.1.1, they don't provide the structural information of the subject but only record the electric signals and show the signals as lines on paper or screen, as shown in Figure 2.3. EEG has a high temporal resolution (milliseconds) as it continuously measures the electrical activity in the brain, but a poor spatial resolution [82]. It is often used for diagnosing seizure disorders, tumours, degenerative disorders and metabolic disturbances that could affect the brain.

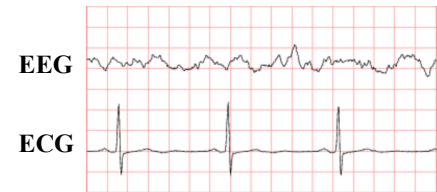


Figure 2.3: The example of EEG and ECG images.

ECG is similar to EEG, but its diagnosis area is the heart. ECG is often used to measure the rate of heartbeats and heart chamber positions. In contrast to EEG, fMRI has low temporal but relatively high spatial resolution. Thus,

<sup>2</sup>URL: <https://bigpictureeducation.com/brain-imaging-images>

acquiring EEG and fMRI simultaneously has the potential for monitoring the joint inferences of brain activities, but also poses many technical challenges, such as the artefacts problem [91, 73].

Nuclear medicine is a branch of medicine which uses small amounts of radioactive materials called radiotracers to diagnose and treat diseases. The main difference between nuclear medicine imaging and other imaging modalities mentioned previously is that the emphasis of nuclear medicine imaging techniques is the physiological function but not the anatomy or structure of the subject. For such reason, nuclear medicine imaging could be classified as functional imaging or physiological imaging. The two most widely used imaging modalities in nuclear medicine are SPECT and PET. Since the main focus of this work is on PET, the detailed discussion about PET will be introduced in Section 2.2. SPECT is similar to PET as it uses radiotracers and detects gamma rays, but the gamma radiations emitted by SPECT tracers are measured directly by two gamma cameras, whereas PET tracers emit positrons that annihilate with electrons and generate two gamma photons in opposite directions simultaneously. As shown in Figure 2.4 (a), the two gamma cameras are placed on opposite sides of the patient and are rotated around the patient. Then the projections are acquired during the rotation which can be reconstructed either analytically by filtered backprojection (FBP) or iteratively by ordered subset expectation-maximisation (OSEM). These reconstruction methods are similar to the methods used in PET, which will be discussed in Section 2.2.3. SPECT is capable of a much wider range of radioisotopes than clinical PET, such as  $^{123}\text{I}$ ,  $^{99\text{m}}\text{Tc}$ ,  $^{111}\text{In}$ ,  $^{155}\text{Tb}$ ,  $^{67}\text{Ga}$ ,  $^{90}\text{Y}$ , etc., each with its own diagnostic purposes. A recent review of the radionuclides used in SPECT is available in [64]. SPECT is often used to diagnose or monitor brain disorders, heart diseases and bone problems. Although this kind of scanning tool is eclipsed after PET appears, it is far from being obsolete [64]. Both of these two techniques have their strengths and weaknesses. The most competitive advantage of SPECT is that the test is less expensive and more readily available, but the low resolution (which is about 1 cm resolution) is the main weakness.

As this brief review of medical imaging modalities shows, each modality has their advantages and disadvantages. The hybrid imaging technique offers an opportunity to provide the fused images of two (or more) imaging modalities. Some hybrid imaging modalities will be discussed in the following section.

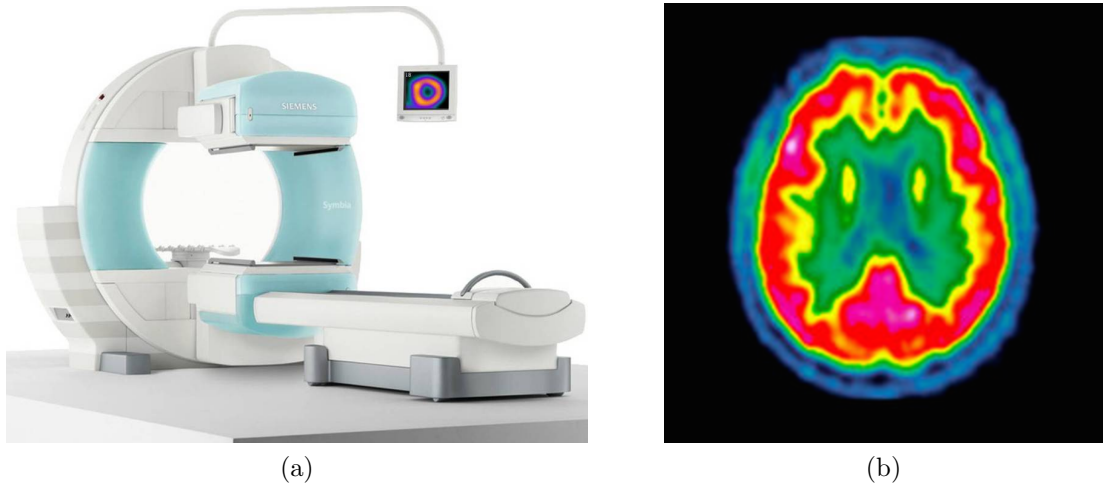


Figure 2.4: (a) SPECT scanner, Siemens Symbia<sup>TM</sup> S. (b) SPECT image showing normal brain activity<sup>3</sup>.

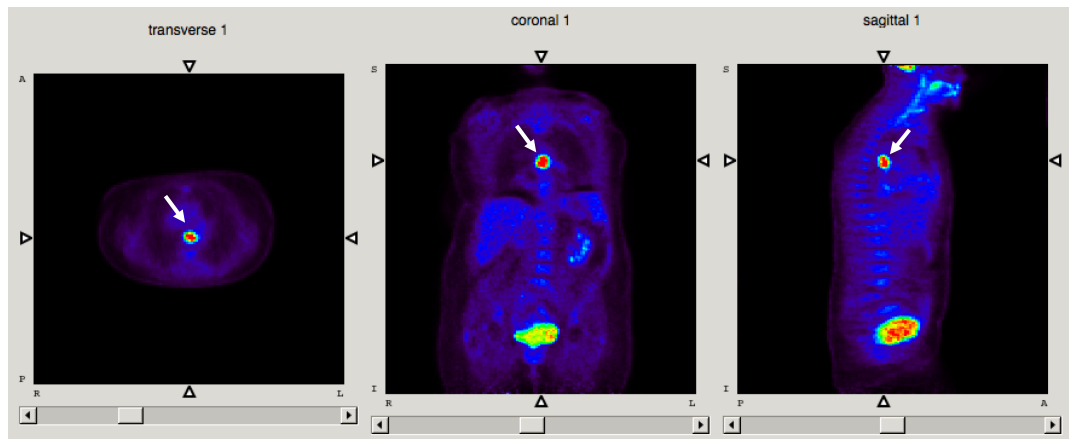
### 2.1.3 Hybrid Imaging Modalities

Historically, medical imaging devices of either morphological or functional imaging have been developed, more or less, independently [110]. Nevertheless, the pre-clinical designs and early prototypes of the combined imaging modalities, in particular PET/CT, has received with enthusiasm because of the significant diagnostic advantages they can offer. As already mentioned, hybrid imaging is defined as the fusion of two or more imaging technologies, it is not only the summation of different techniques but also more powerful to show the molecular processes *in vivo* within more accurate anatomic images [43]. We begin by presenting the outstanding technique—PET/CT, this is followed by a newly introduced scanner—PET/MRI.

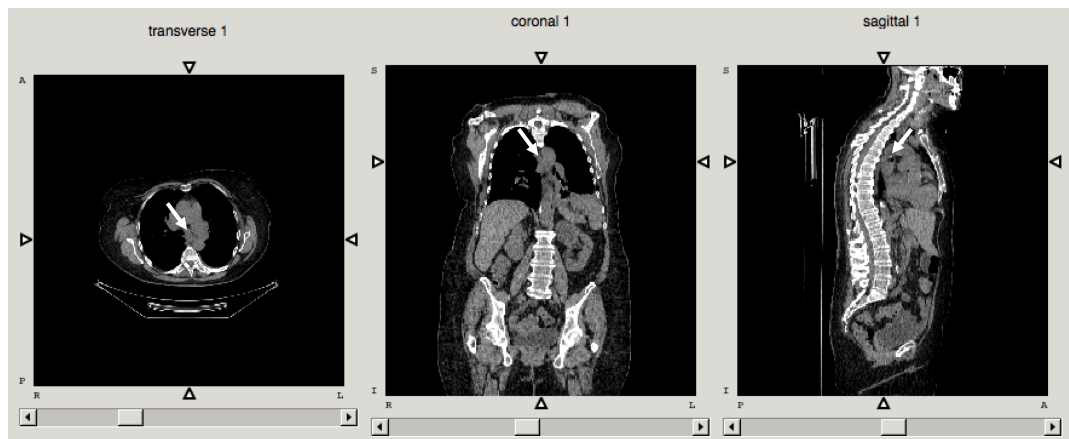
### PET/CT

The combined PET/CT scanner was named the “Medical invention of the year” in 2000 by Time Magazine. The first prototype PET/CT was installed in 1998 at the University of Pittsburgh Medical Center and scanned more than 300 patients from 1998 to 2001 [9, 112], then the demand of commercial PET/CT grew rapidly because of the advantages of this technique for oncology imaging [113]. PET/CT is a combination of PET and CT and acquires aligned functional and anatomical images simultaneously. In addition, the CT scanning provides the correction of PET data for attenuation. Kinahan et al [55] provided an algorithm for attenuation corrections associated with scaling the CT images from

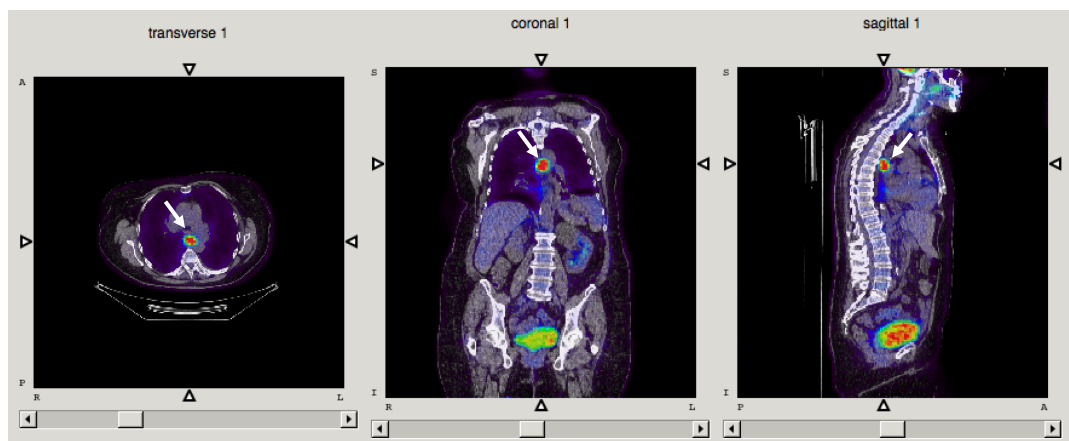
<sup>3</sup>URL: <http://www.sciencephoto.com>



(a) PET images



(b) CT images



(c) Fused images

Figure 2.5: PET/CT scan generated on a GE Advance scanner of a lung cancer patient<sup>4</sup>, showing from left to right, transverse, coronal and sagittal view in AMIDE [61]. The tumour was indicated by the arrows.

<sup>4</sup>Case contributed by Dr. Peter Murphy, Cork University Hospital, Cork, Ireland.

X-ray energy (from 40 keV through 140 keV) to PET annihilation photon energy (511 keV). Essentially, using CT scan for attenuation correction reduces the noise in PET and saves the scan time by at least 40% [113]. Until recent years, CT-based attenuation correction is still an active research area [53, 97]. After calculations, the attenuation-corrected and reconstructed PET images are available for viewing—see Figure 2.5 as an example. Figure 2.5 shows that the PET image is highly noisy and has low resolution, but it highlights the tumour which is indicated by the arrow. In contrast, CT image has high resolution and provides accurate anatomical information, but the tumour region is inconspicuous. While the fused image provides an high quality anatomical reference for the tumour region. This is a powerful example to show that the hybrid PET/CT scan is an effective approach to provide precise localisation of regions of interest (ROI) within a morphological framework. Addition of CT component not only improves correction for attenuation, but also helps with localisation of the structures. Moreover, the combined PET/CT brings confidence to the reader, whether radiologist or nuclear physician [12].

Actually, since the first commercial PET/CT reached the market by 2001, the sales of stand-alone PET scanners in the United States declined to zero by 2006 [110] and only 13% of PET studies was performed by using stand-alone PET in 2008 which used to be 30% in 2005 [43]. Up to 2009, more than 2,000 PET/CT scanners have been installed in the United States [16]. The widespread use of PET/CT is not only in the United States but also worldwide. For example, in mainland China, there were 240 PET/CT scanners until 2015 and the total number of PET studies was 469,364 [22]. At present, there are 8 PET/CTs in Ireland—1.7 scanners per million inhabitants, and more than 400 scanners in all of Europe [29].

Our analysis in Chapter 3 is based on a rich collection of phantom measurements assessing imaging quality which acquired in a number of PET clinical centres in the US, and the work described in Chapter 4 & 5 are motivated by a recently acquired physical phantom dataset from a PET/CT scanner at a local hospital.

## PET/MRI

Compared with the rapid development of PET/CT and SPECT/CT, PET/MRI system has remained in the pre-clinical arena for a decade until 2006—the first combined PET and MRI scan was performed [101]. Since the phototubes, utilised in PET, are sensitive to magnetic fields, an PET/MRI configuration is more



challenging and more complex than the previously discussed hybrid modalities [110]. While the need for simultaneous PET/MRI scanner is still in debate, the competitive advantage of this modality is widely agreed. For example, in PET/MRI scanner, MR imaging provides excellent soft tissue contrast which can be combined with the physiologic information provided by PET. On the other hand, the lack of ionising radiation offered by MRI allows the reduction of the exposed radiation dose, it is important for the paediatric imaging and the patients who need to undergo repeated imaging [52].

## 2.2 Positron Emission Tomography

Positron Emission Tomography (PET) is a widely used medical imaging technique which generates three-dimensional images based on the detection of photons emitted by a positron-emitting radionuclide within a volume or body. In recent times, PET plays an essential role in oncology, cardiology as well as in neurology. This section will give a brief review of this incredible technique from various aspects.

### 2.2.1 History

The early medical application of the positron can be traced back to 1951. The first brain probe using positron data was reported by William Sweet at Massachusetts General Hospital (MGH) [106]. The patient was positioned between two opposing sodium iodide (NaI(Tl)) detectors, and the results were printed as a 2-D image of the positron source. In the same year, Frank Wrenn published the study of the localisation of brain tumours by detecting the coincidence scintillation of annihilation pairs [125]. Image reconstruction techniques were developed subsequently in the 1960s and 1970s, and the invention of filtered back projection reconstruction by David Chesler accelerated the progress of reconstruction technique [24, 25, 26]. Chesler tested filtered back projection by computer simulation and then applied this type of reconstruction to PET and CT data. In 1973, the first PET tomography (PETT I) was built by Michael Phelps at Washington University. Phelps named it as Positron Emission Transaxial Tomography (PETT), and later reduced the name to PET [77]. Although this first tomography marks the beginning of modern PET technology, it was failed in producing proper reconstructed images due to the lack of attenuation correction, etc. In the following years, refinement of PET devices were being developed very fast, mainly by Phelps, Hoffman and Ter-Pogossian et al., such as PETT II and PETT III [83, 84, 108]. The PETT III system consisted a hexagonal array with eight

NaI(Tl) detectors on each side and detected the coincidences with the detectors on the opposing sides. Another step in the development of the PET technique was the use of ring systems instead of hexagonal array of detectors [10], this ring system has become the prototype of the current shape of PET. In 1984, Burnham et al. [17] developed a complicated detector ring that individual small scintillator detectors were placed ahead of photomultipliers with a circular lightguide between them, after which multi-crystal detectors with position-sensitive photomultiplier tubes, so called the “Block” detector, were constructed to reduce the cost without sacrificing performance [20]. The majority of present tomographies are using some form of the “Block” detector which is conceived as a means to simplify the Burnham detector—see Figure 2.7.

During the period from 1987 to 1990, some major imaging companies, such as Siemens and General Electric (GE), started to distribute commercial PET devices [77]. Ever since, PET has been validated for clinical applications and not just research oriented. As development continued, a system with Lutetium Oxyorthosilicate (LSO) scintillation crystals, which has high light output, was used to improve the resolution of detectors [21].

### 2.2.2 The Physics of PET

Based on the discovery of the positron in 1933 by Carl D. Anderson [4], PET is a medical imaging technique that detects and quantifies the spatial distribution of a positron-emitting radiopharmaceutical (radioisotopes/radiotracer), which is chosen to mark a specific metabolic activity/physiological process in the body. Once the positron is emitted from the radiotracer, it annihilates with a nearby atomic electron, then produces two 511 keV photons traveling in opposite directions. More specifically, radioisotopes may decay via positron emission, in which a proton ( $p$ ) in the atomic nucleus decays to a positron ( $e^+$ ), a neutron ( $n$ ) and a neutrino ( $\nu$ ) with release of energy (Eq. 2.1).

$$p \xrightarrow{\text{trans.}} n + \nu + e^+ + \text{energy} \quad (2.1)$$

As shown in Figure 2.6, a positron is emitted from the nucleus and travels randomly through the surrounding matter for a few millimetres—depending on its energy. When it loses enough energy, the positron interacts with a single electron ( $e^-$ ) and produces two 511 keV photons travelling in an antiparallel direction, this process is called annihilation. Once the two annihilation photons are detected by a pair of detectors within a predefined coincidence time window (6 ~ 12 ns) [128],

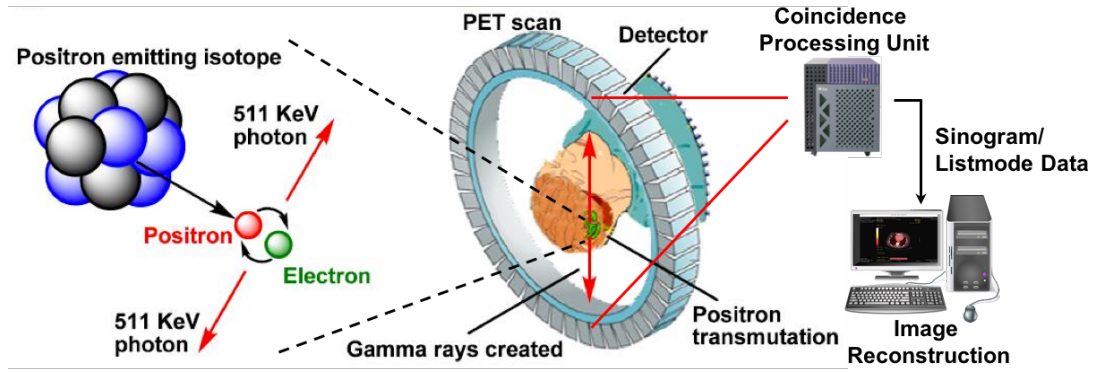


Figure 2.6: Schematic of PET scan procedure. Left: Illustration of the annihilation process of a positron and an electron. Middle: Detection of both 511 keV photons in coincidence by the ring detector array in PET camera [60]. Right: Signal collecting and processing procedure.

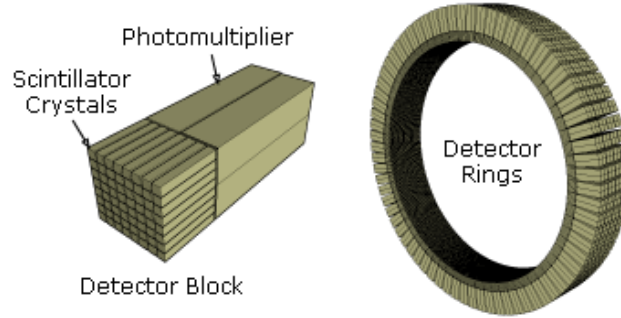


Figure 2.7: Schematic of a block detector (left) and a ring of a PET scanner (right)<sup>5</sup>.

a “true” coincidence is registered along the line between the detector cells, which is called the Line of Response (LOR). There are other types of coincidence events such as scattered, randoms and multiples. Scattered coincidence is the event that one or both of the detected annihilation photons undergoes Compton scatterings during its traveling, which could lead to the wrong registration and overestimation of the activity. When two independent photons, *i.e.* photons from different annihilation event, are detected within the same time window, the coincidence is random or accidental coincidence. Random coincidences reduce the accuracy of detection and produce undesired background in the PET images [8]. If more than two photons are detected within the same time window, multiple coincidence occurs. This type of coincidence would be rejected since the determination of which annihilation should be assigned is impossible [128].

After the corrections of scattered, random coincidences and attenuation, the

<sup>5</sup>URL: [https://commons.wikimedia.org/wiki/File%3APET-detectorsystem\\_2.png](https://commons.wikimedia.org/wiki/File%3APET-detectorsystem_2.png)

data collected in many orientations are then resorted and rebinned to form the projection view that is called a sinogram. Sinograms are referred to as raw data in PET, and are used in image reconstruction.

### 2.2.3 Image Reconstruction

Image reconstruction aims to provide images of distribution of injected radiotracers in a subject. Over the last four decades, lots of methods have been developed for reconstruction of PET images. Reconstruction methods are either analytical or iterative approach. Analytic reconstruction offers a direct and simple mathematical solution for the reconstruction problem such as filtered backprojection (FBP). Iterative reconstruction methods are more complicated and provide more accurate solution such as expectation maximisation (EM) method. Both methods are described below.

#### Filtered Backprojection

Filtered backprojection (FBP) is the simplest and most widely used analytical, sometimes called Fourier-based, reconstruction method in PET imaging. In the early 1960s, the simple backprojection technique was introduced [56], it was based on the straight backprojection (inverse 2-D Fourier transform) of its multiple projections to a common image plane. However, this simple backprojection can not recover the true image due to the oversampling in the centre of the Fourier transform [38]. A new approach proposed by David Chesler [25, 26] solved this problem by filtering the projection data before performing backprojection, see Figure 2.8 for a brief illustration.

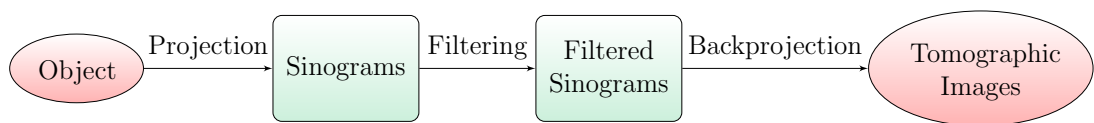


Figure 2.8: Illustration of the filtered backprojection computation process.

Today, a number of filters have been designed and used in the reconstruction of PET images. A common well known filter is the ramp filter which convolved with the angular projections in the frequency domain before backprojection. Use of the ramp filter removes the blurring effect of the simple backprojection, but it amplifies the the high-frequency noise and produces noisy reconstructed images. Therefore, various filters have been developed to eliminate the high-frequency

noise such as Hanning filter which is a low-pass filter that limits the high frequencies. In fact, there is no perfect filter, even though PET has been in use for decades, thus the performance examine of filters is normally done by trial [96].

## Iterative Reconstruction

The analytical reconstruction such as filtered backprojection (FBP) has limitations and weaknesses, such as particularly remarkable artefacts near high intensity regions. Iterative reconstruction is an alternative to the analytical reconstruction, which is more accurate in representing structures in image but has greater computational costs. In 1977, Dempster et al. [27] proposed an expectation maximisation (EM) algorithm to numerically determine a maximum likelihood estimate (MLE). Five years later, the ML-EM algorithm, introduced to the field of image reconstruction by Shepp and Vardi [103], provides the foundation for today's most popular reconstruction methods.

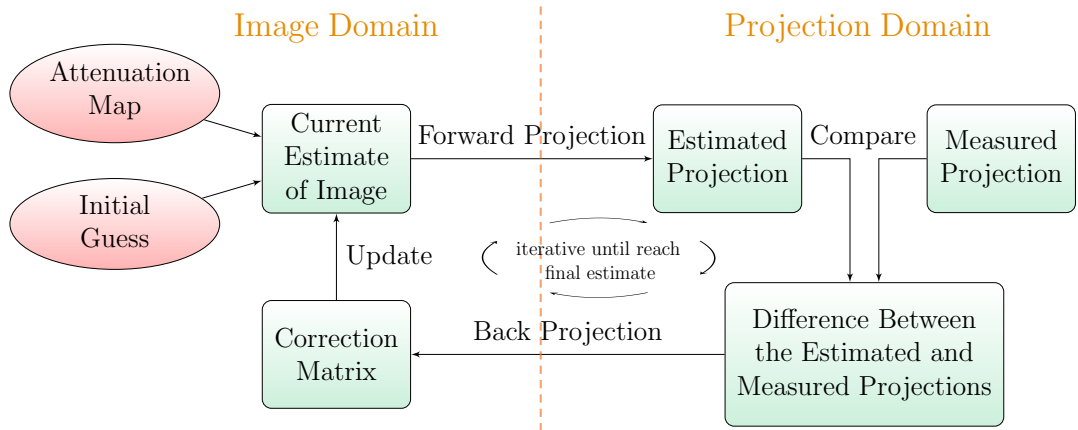


Figure 2.9: Conceptual illustration of iterative image reconstruction methods.

The flowchart in Figure 2.9 shows the basic procedure of using an iterative algorithm. It begins with an initial estimate, which may be a uniformly distributed image incorporated with attenuation correction, then the projections of the initial estimate can be accomplished. The difference between the projections on the base of the initial estimate and the ones actually measured can be used to generate additive or multiplicative corrections for the initial estimate (usually via backprojection). This modified estimate then becomes the starting point for the next iteration until an acceptable agreement between the estimated and measured projections is achieved. The above process is the core of all iterative reconstruction algorithms. If the multiplicative corrections are used, the method is the ML-EM, and if the additive corrections are used, the method is the additive

simultaneous iterative reconstruction technique (ASIRT). The ASIRT method is not of interest since it is not commonly used. The main disadvantage of the ML-based iterative reconstruction is the difficulty in determining the number of iterations—too many iterations can amplify the noise in the image [38]. Another drawback of ML-EM algorithm is the low convergence rate—approximately 20–50 iterations to reach an acceptable convergence level. Since each iteration contains one forward projection and one backprojection, the overall processing time of the ML-EM algorithm is considerably more than the FBP.

To reduce the computation time, an acceleration approach called the ordered subsets expectation maximisation (OSEM) algorithm was introduced by Hudson and Larkin in 1994 [45]. The OSEM approach can be considered as a modified version of the ML-EM, which divides the entire data set into subsets for each image update and applies standard ML-EM iteration to each subset. Suppose there are  $n$  subsets, each containing equal angular intervals of projections, the ML-EM iteration is performed on each subset, thus the OSEM estimate approaches to the final estimate is  $n$  times faster than the conventional ML-EM.

In general, iterative reconstruction methods greatly reduce the streak artefacts and provide more accurate reconstructions than analytical methods. All iteratively reconstructed values are positive due to a positive constraint which ensures that, as the reconstructed data are supposed to represent tracer distribution, the produced image data are always positive [111]. The distribution of positively constrained data is discussed in greater details in Chapter 4. The ML-EM and OSEM iterative algorithms are currently used in many PET and SPECT systems.

## 2.2.4 Radiotracers

The radiotracer plays an essential role in PET because it has a fundamental effect on image quality and clinical interpretation. The radiotracers bear two responsibilities which are participating in metabolism activities within the organism and emitting signals that are detectable [117]. The applied tracers should have the same biological and physiological functions as the substance to be labelled.

$^{18}\text{F}$  is one of the most commonly used radionuclides in clinical PET imaging and often used to make up Fluorodeoxyglucose (FDG) by substituting for hydrogen.  $^{11}\text{C}$ -labeled glucose behaves in the same way as normal glucose (unlabelled) which allows it to provide the information of how glucose behaves exactly, but it is rarely used in clinical applications due to the short half-life which makes it expensive [37]. The ten-minute half-life of  $^{13}\text{N}$  limits its clinical usage—routinely

Table 2.1: The most commonly used radioisotopes in PET, adapted from [58].

Radioisotope	Half-life (min)	Energy (MeV)
$^{18}\text{F}$	110	0.63
$^{11}\text{C}$	20.4	0.97
$^{13}\text{N}$	9.96	1.19
$^{15}\text{O}$	2.07	1.72

used in simple procedures such as using  $^{13}\text{N}$ -ammonia to measure myocardial blood flow.  $^{15}\text{O}$ -labeled tracer with short half-life can be used in a process with short biological half-life, for example,  $^{15}\text{O}$ -water is commonly used to study the blood flow in brain [68].

## 2.3 Noise in PET Image

PET images are recognised as high noise level images compared to other medical images such as CT and MRI. The noise in PET images affects their geometric interpretation as well as quantitative interpretation. Some post-processing techniques may be employed to reduce the noise in PET images. The estimation accuracy of the parameters which characterise the noise is crucial to improve the efficiency of image noise reduction. However, the statistical properties of noise in reconstructed PET images are often not well characterised. In Chapter 4, we examine the role of Gamma distribution in representing clinical PET data, and provide a novel view of describing the statistical characteristics of noise. In this section, the Poisson nature of emission process and some sources of noise in PET data are discussed.

### 2.3.1 The Poisson Nature of Emission Process

The basic emission process associated with PET imaging is Poisson in nature. As mentioned in 2.2.2, two photons are emitted when the annihilation occurs and detected by a pair of detectors coincidentally. Then the signals detected by detectors can be considered as the count of detected photons. However, it should be note that the total number of emissions is typically much bigger than the detectors count, because all of those photons that do not hit the detectors would not be detected, for example some photons traveling along lines that are not crossing the detector rings and some are attenuated by surrounding tissues and organs [115]. Suppose a trial that the observation of an emission within a small

time interval,  $t$ , within  $T$ , is a success. One emission of a pair of photons does not affect the probability of the occurrence of the second emission, i.e. events occur independently. Thus, the number of events observed in some time period,  $T$ , follows a Poisson distribution.

Since the emission process follows a Poisson distribution and the noise in conventional planar emission images, *e.g.*, blood pool ventriculography [40], is Poisson distributed, many would deem that the Poisson or approximately equivalent Gaussian model is appropriate to describe projection data. However, it is not the case. Many factors could affect the noise distribution of projection data. Furthermore, the corrections and reconstructions applied for projection data are not only amplify the magnitude of the noise, but also induce spatial correlations resulting on clinical PET images [95]. The following section will discuss some of these factors in detail.

### 2.3.2 Sources of Noise in PET Image

***Scatter and random coincidences:*** Image noise is the random variations or uncertainties in pixels across the image. Two major sources of noise in PET are scatter and random coincidences which have been defined in 2.2.2. These two types of coincidences can reduce image quality and their effects need correction. In the case of scatter event, photons deviate from their original directions and result in false counts in the PET images which may cause visible artefacts. Some photons scattered outside the field of view (FOV) without being detected are resulted in count losses. In the case of random coincidences, photons from two independent annihilations are detected in the same time window and registered wrong LOR in projection. These random events may produce a relatively uniform background across the reconstructed image [8].

***Poisson statistic noise:*** Since PET scanning process is based on the detection of annihilation photons and radioactive decay obeys Poisson statistics, the number of counted photons ( $N$ ) in a certain period of time (time frame) should has Poisson noise which is given by  $1/\sqrt{N}$ . It can be reduced by increasing the total counts in the image, such as increasing the scanning time, injecting larger dose of tracers, or improving the sensitivity and efficiency of detectors. However, these factors have limitations, *e.g.*, longer scanning time gives rise to discomfort of the patient and causes increasing movements. Too much activity could lead to the exposure of radiation and then raise the risk of radiation induced cancer. Additionally, more tracers produce more photons, which not only



increase the true coincidence counts but also random and scatter coincidences as well as dead-time loss (the factor of dead-time will be introduced shortly). The sensitivity and efficiency of detectors may be limited by the crystal performance and the design of device.

**Dead-time loss:** Dead-time is defined as the short interval between each detection of photon during which the detector is incapable of further response. The dead-time loss of counts increases for the high activity situations and induces more noise in PET images. The faster and smaller crystals can be used in the detector rings in order to minimise the dead-time.

**Correction procedure:** Although the corrected images are generally more truthful representations, the correction procedure itself may produce undesirable artefacts. The corrections applied for attenuation, scatter and random coincidences may amplify the magnitude of the noise in projection data, and may also induce spatial correlations [95]. Inaccurate correction procedures add more noise in PET images and degrade the image quality.

**Applied reconstruction method:** Different noise levels appear in the different reconstructed images depending on which reconstruction method was applied. For example, FBP reconstruction produces more global noise distribution compare to iterative reconstruction, *i.e.*, FBP spreads noise from high intensity regions to low intensity regions that makes the noise more uniform over the image. While iterative reconstructions, such as ML-EM and OSEM, show that little noise is spread from hot regions to cool regions [7, 90, 123]. Thus low noise level is indicated in low intensity regions. For the images using OSEM reconstruction, the signal-to-noise ratio (SNR) is better than using FBP at equivalent resolution [90]. Our analysis in Chapter 4 compares the difference of noise properties between FBP and iterative reconstructed PET images.

**Sources of noise correlation:** As already mentioned, the positron emission itself is a Poisson point process, there is no correlation between either the true coincidence of detected data or the scatter and random noise. But different post-processing methods could lead to different autocorrelation structures in PET images. For instance, the filtering and smoothing process in FBP reconstruction can introduce significant noise correlations (“streaks” artefacts) in the reconstructed image [80], *i.e.*, the ramp filter used in FBP amplifies the high

frequencies and creates spatial autocorrelation to the pixel data. Correlation between the pixels affects the image quality and disturbs the prediction of scanner performance—images with equal signal-to-noise ratio (SNR)<sup>6</sup> may have different autocorrelation structures [74]. Thus signal-to-noise ratio becomes an inadequate measure of PET image quality when images of different structures and degrees of noise correlation are involved. Therefore, correlations in PET images can not be ignored.

In Chapter 5, an empirical assessment of 3-D auto-correlation functions is introduced and auto-regressive (AR) type models are used to represent spatial correlation structure. We also suggests a very practical way to simulate PET data with noise characteristics associated with operational PET scanners.

---

<sup>6</sup>Signal-to-noise ratio is the simplest form to characterise image quality.

# Chapter 3

## Spatial Statistical Characteristics in Clinical PET scanners

### 3.1 Background

This chapter describes the empirical assessment of spatial statistical characteristics—bias, variance and covariance—in a rich collection of PET phantom measurements assessing imaging quality. The work has been published in the volumes of conference proceedings [71, 72].

#### 3.1.1 PET Scanner Quality Assurance

The number of PET or PET/CT imaging sites is growing up rapidly, thus quality assurance (QA) procedure is necessary to ensure that the produced images meet performance requirements [51]. Quality control (QC) is a critical component of routine clinical PET practice which is an established procedure focused on monitoring the performance of operational scanner on a periodic basis (daily, monthly or yearly), especially for image quality. For technical information on QA including further details on QC procedures and clinical practice protocols, the reader is referred to [51, 129].

#### 3.1.2 Uniform Cylindrical Phantom

Uniformity of the reconstructed image is an important measure of PET scanner, which measures the system response to a homogenous distribution of radioactivity. The uniform cylindrical phantom is commonly used for routine QA and calibrations in assessing transverse and axial uniformity across image planes [51]. The cylinder does not have any internal structure and is filled with a known

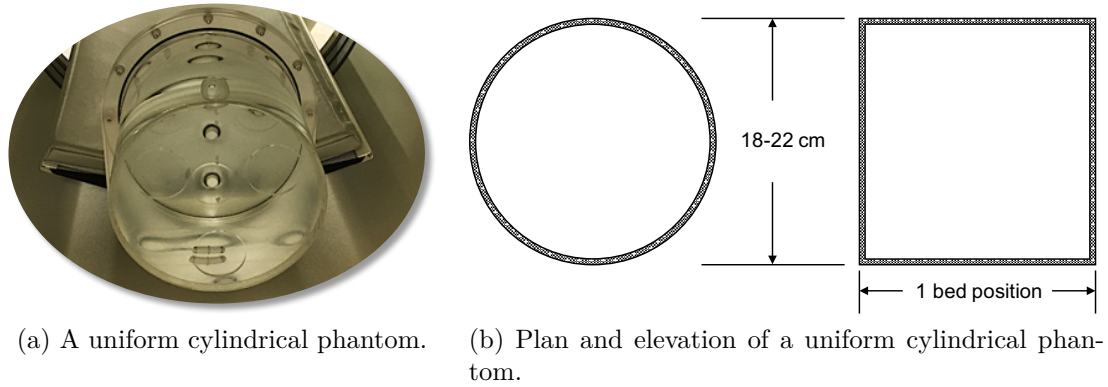


Figure 3.1: Illustration of uniform cylindrical phantom.

amount of radioactivity<sup>1</sup>—as shown in Figure 3.1a. The diameter of the phantom should be 18–22 cm and the length should be greater than the axial field of view (FOV) of the scanner—as shown in Figure 3.1b. After the preparation of the phantom, it is scanned using standard acquisition and reconstruction protocols in PET or PET/CT scanners. Then the evaluation of uniformity should be made on the reconstructed data. More specifically, the systematic deviations between the actual activity value in the phantom and its measurement can be evaluated by an average of PET-recorded voxel values in the region of interest corresponding to the phantom in the scanner.

### 3.1.3 ACRIN Data

The American College of Radiology Imaging Network (ACRIN) was developed to ensure that PET scanners were being operated properly and to qualify PET sites for use in multi-centre cancer clinical trials [100]. A National Cancer Institute (NCI)-sponsored program—the Centres for Quantitative Imaging Excellence (CQIE) program—has created a data set to allow qualification of PET imaging sites for use in cancer clinical trials. The data have been assembled and maintained by ACRIN, with a rich collection of PET phantom measurements assessing imaging quality. The CQIE program was initiated in 2010 to pre-qualify imaging facilities (including PET, CT and MRI) at all NCI-designed cancer centres for oncology trials. An overview of the CQIE program is provided in [93] and the CQIE PET/CT qualification process and results are reviewed in [99].

ACRIN imaging protocol carried out a series of dynamic phantom studies on PET scanners used by a set of institutions engaged in clinical cancer imaging.

<sup>1</sup>For the physical phantom data used in this thesis, the injected radionuclide for uniform cylindrical phantom is FDG.

Scans were acquired and reconstructed in 3-D mode using site-specific choices for various algorithm parameters. These measurements offer an opportunity to obtain an empirical understanding of the statistical characteristics—bias, variance and correlation patterns—of operational scanning data, and to explore factors that may be associated with variation in these attributes. Our study uses voxel-level data sampled in the interior of the phantom volume to develop estimates for bias, variance and spatial correlation. Figure 3.2 shows typical data of a particular scanner. Voxel-level data in a cylindrical volume, within white outline, are used in analysis.

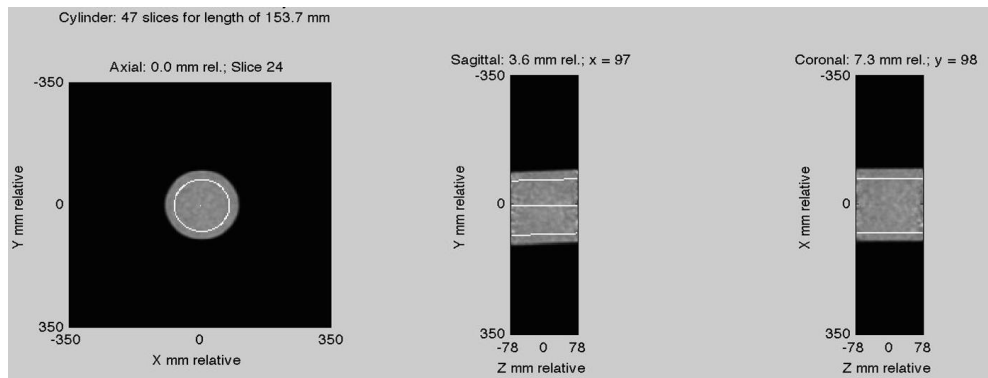


Figure 3.2: Sample Phantom data in the ACRIN set.

## 3.2 Empirical Analysis of Spatial Characteristics of 3-D PET Image

### 3.2.1 Introduction

Previous work with the data has focused on systematic deviations between the actual activity value in the phantom and its measurement by an average of PET-recorded voxel values in the region of interest corresponding to the phantom in the scanner. But the data also allow for more detailed evaluation of imaging characteristics. Our work focuses on components of random variation. Dynamic data considered are obtained from 3-D sequential scanning, typically with variations on OSEM for reconstruction, of a uniform cylindrical phantom over a 25-minute period. We evaluate axial, transaxial and temporal patterns in variance and covariance. Variance characteristics are dominated by effective counts—these are lower over short time frames and in the axial extremes of the scanner bed. After adjustment for variance the spatial auto-correlation patterns in 3-D are

evaluated. Auto-correlation is decomposed as a product of axial and trans-axial effects. The trans-axial pattern follows the structure generally associated with standard 2-D filtered back-projection reconstruction, *i.e.*, largely determined by the impulse response. Having a phantom based measurement of the variance and auto-correlation patterns gives the possibility to make more efficient use of region of interest data from patient scans. Usual regional averages can be replaced by weighted averages, with weights inversely proportional to the local variance. In addition, an approximate standard error for an ROI average can take account of the phantom derived measurement of the auto-correlations. Thus information from routine phantom scanning would practically enhance the value of information recovered for patient studies.

### 3.2.2 Methodology

The voxel-level data in the  $(i, j)$ 'th pixel of the  $k$ 'th slice at time  $t$  is represented by  $z_{ijkt}$ . These values are decay corrected activity per mL values, normalised by the injected dose per mL of the phantom. In the absence of measurement error, the  $z$ -values should be unity. The mean deviation of the  $z$ -data from unity represents bias.

We model the mean of the  $z$ -data as a product of a radial ( $u_r$ ), axial ( $u_k$ ), and temporal ( $u_t$ ) effects. The radial and axial effects are a function of the radial and axial distance of the voxel from the centre of the scanner. An iterative procedure is used to estimate these effects. For assessment of variance, we rescale the  $z$ -data to remove bias to give values

$$e_{ijkt} = z_{ijkt} / (\hat{u}_t \hat{u}_k \hat{u}_r) - 1$$

and model the variance as a product of a radial ( $\sigma_r^2$ ), axial ( $\sigma_k^2$ ) and temporal ( $\sigma_t^2$ ) effects. These are again estimated by an iterative procedure. The standardised data are produced as

$$\tilde{e}_{ijkt} = \frac{z_{ijkt} / (\hat{u}_t \hat{u}_k \hat{u}_r) - 1}{\sigma_t \sigma_k \sigma_r}$$

Spatial auto-correlation of the  $\tilde{e}$ -values is assessed in the axial (slice-to-slice) as well within-slice (in the transverse x- and y-directions).

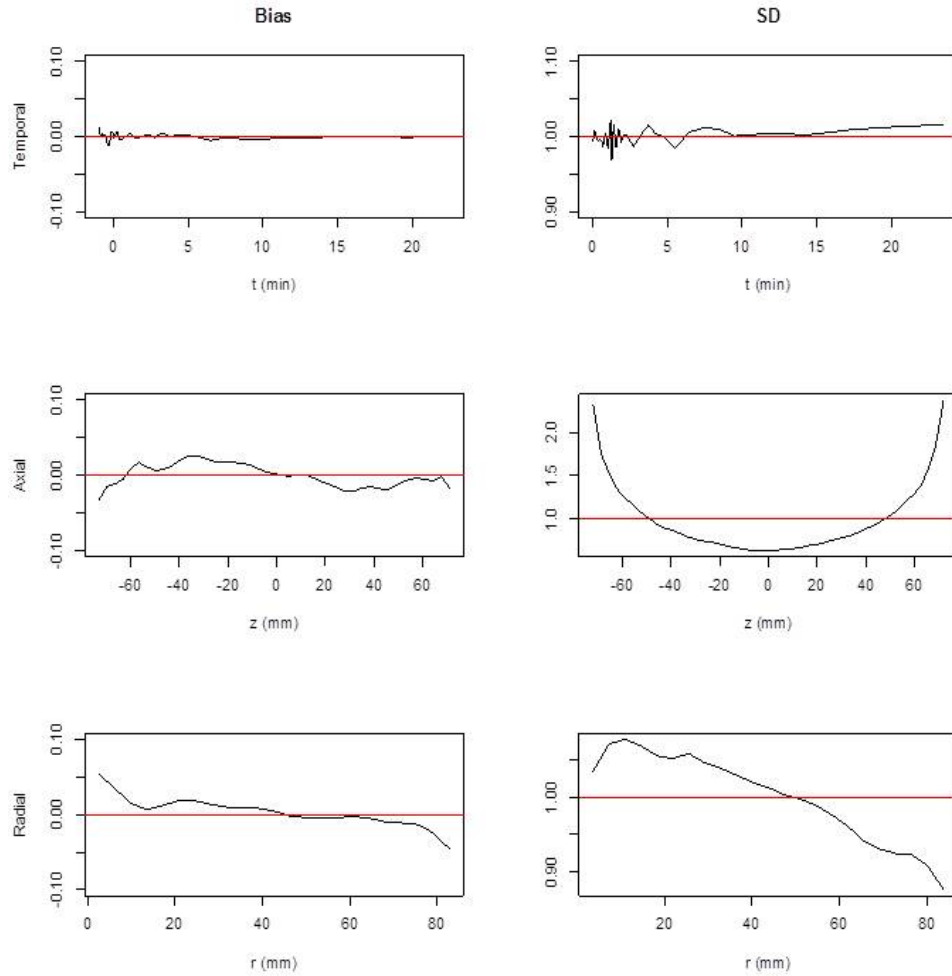


Figure 3.3: Estimated temporal ( $\sigma_t$ ), axial ( $\sigma_k$ ) and radial ( $\sigma_r$ ) bias and standard deviations (SD) in the PET measurement.  $\sigma_t$  is adjusted for effects of frame duration and isotope decay.

### 3.2.3 Results

The estimated bias and standard deviation (SD) for a particular scanner are shown in Figure 3.3. The top row shows that both bias and SD increase with the measurement time. The middle row shows a strong axial pattern of SD—low SD in axial centre and high SD in axial edge. Bias shows no axial pattern. The bottom row shows that SD decreases slightly from the slice centre to the edge. The standardised data are shown in Figure 3.4 (right column), as comparison, the raw data are shown in the left column.

The estimated 1-D autocorrelation as a function of axial and trans-axial distance is shown in the top row of Figure 3.5, respectively. Histogram of square root

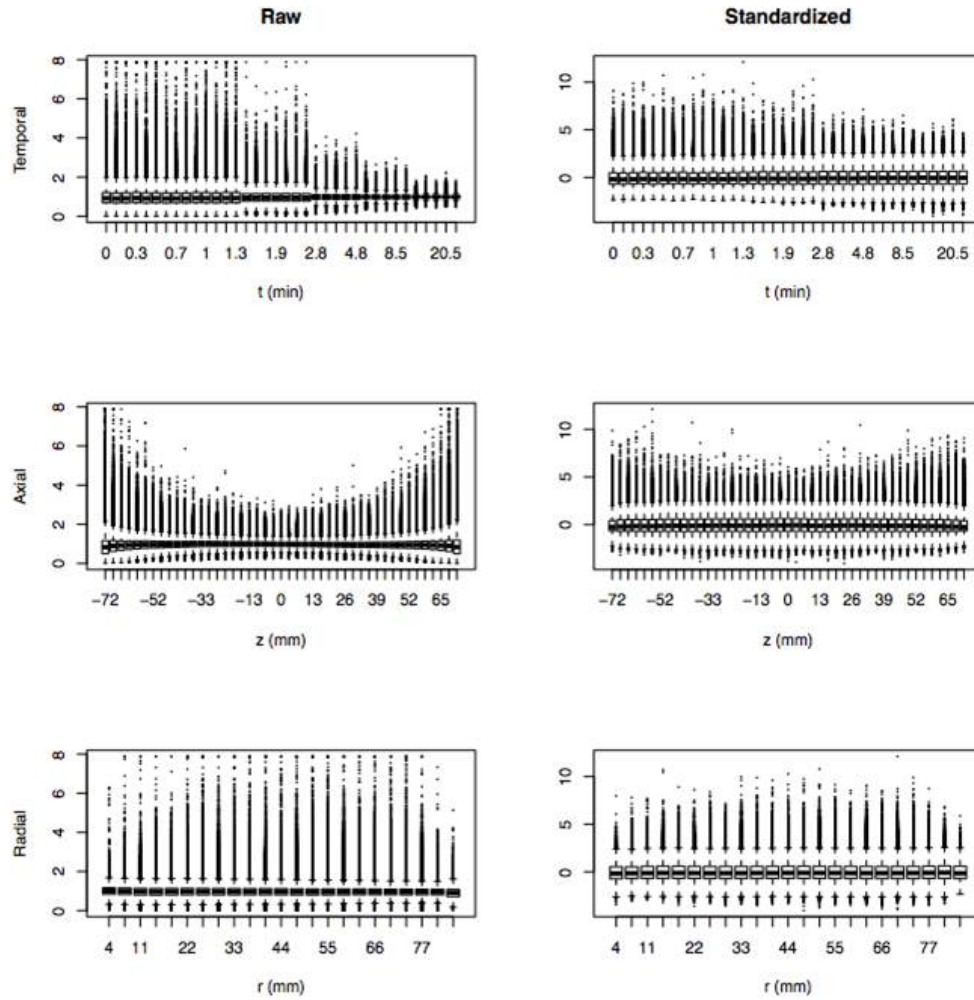


Figure 3.4: Left: Boxplots of the distribution of voxel-level  $z$ -data classified by acquisition time (top), axial (middle) and radial position (bottom). Right: Boxplots of the distribution of normalised data.

Table 3.1: Analysis of Axial, Radial and Temporal bias and standard deviations

Effect	Axial (%)		Radial (%)		Temporal (%)	
	Bias	SD	Bias	SD	Bias	SD
Overall	0.76* (0.09)	27.41* (1.86)	0.81* (0.14)	5.03* (0.11)	0.42* (0.03)	1.56* (0.17)
GE vs. Siemens	-0.42* (0.08)	7.40 (4.56)	-0.26 (0.32)	-4.23 (2.16)	-0.17 (0.15)	0.73 (1.12)
Profile	0.76* (0.11)	25.57* (1.59)	0.80* (0.13)	4.77* (0.16)	0.42* (0.03)	1.28* (0.30)
Interaction	-0.42* (0.09)	6.40 (3.37)	-0.27 (0.28)	-4.01* (1.54)	-0.17 (0.11)	0.62 (0.81)

\* denotes significant.



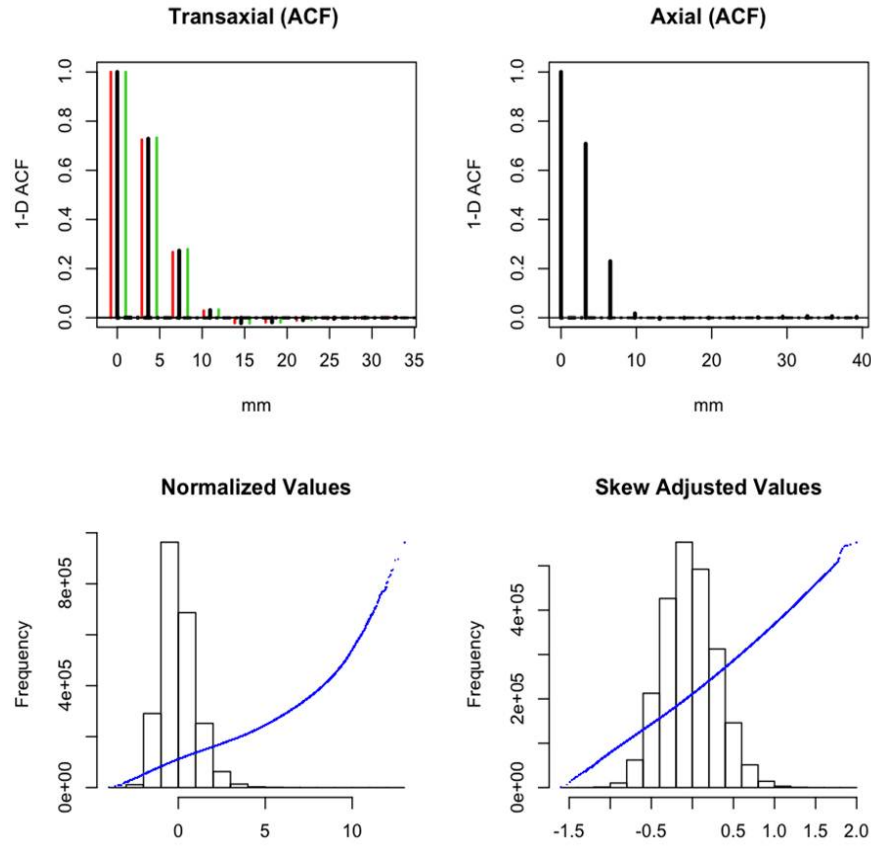


Figure 3.5: Top: Estimated transverse and axial autocorrelation functions (ACF). The red and green lines in the transverse ACF represent autocorrelation in the row, column directions. Bottom left: Histogram of the standardised data and comparison with normal quantiles (blue). Bottom right: Histogram of square root transformed data classified by time and axial position.

transformed standardised data also shown in Figure 3.5. The square root transformed data show good agreement with the Normal distribution as one would expect for Poisson variables. Figure 3.6 shows bias and SD of 28 Siemens (red) and GE (blue) scanners as function of normalised axial and radial location. Box-plots of 28 Siemens (red) and GE (blue) autocorrelation as function of normalised axial and trans-axial distance. Axial, Radial and Temporal, Bias and SD profiles are analysed across scanners (Table 5.1). Note as in Figure 3.3, the temporal profiles are adjusted for frame duration and decay. To reduce the impact of outliers we use median statistics in summarising effects. Standard errors and tests are generated by the bootstrap in R. Figure 3.7 shows boxplots of 28 Siemens (red) and GE (blue) autocorrelation as a function of normalised axial and trans-axial distance. The correlation within planes is similar in both manufacturers but the correlation between adjacent slices is significantly different between the GE and

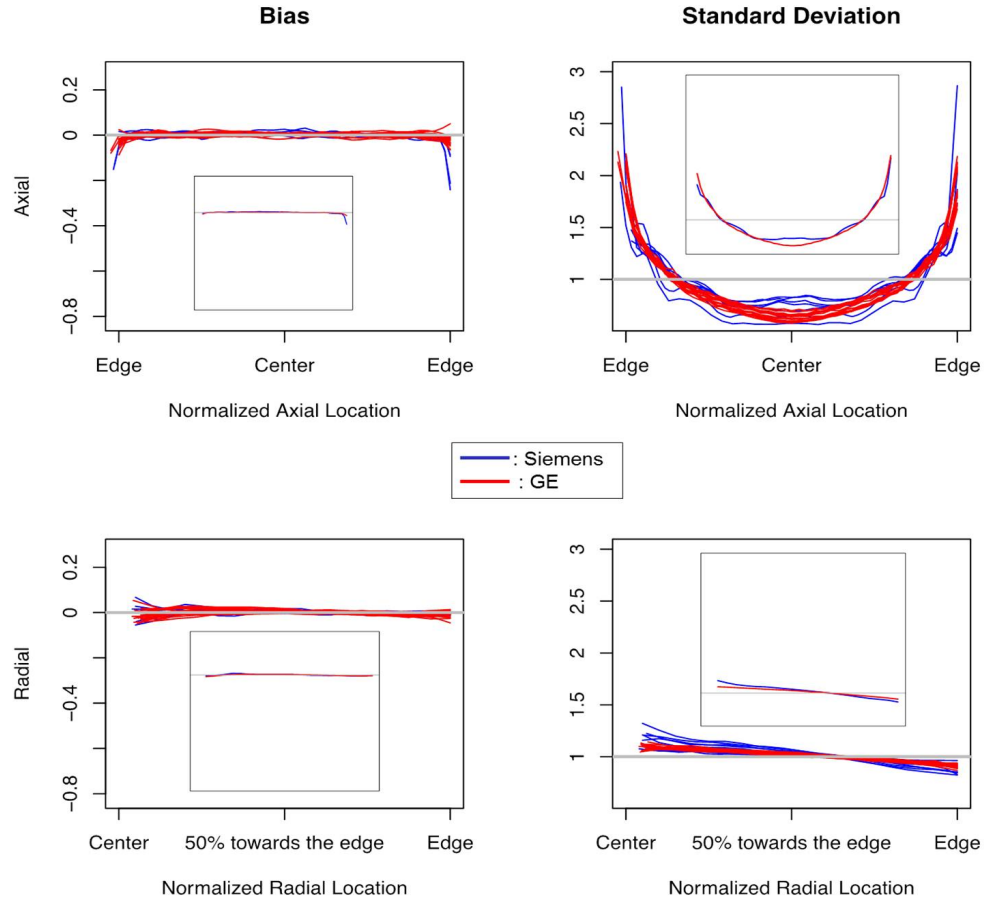


Figure 3.6: Estimated axial ( $\sigma_k$ ) and radial ( $\sigma_r$ ) bias and standard deviation for 28 sites classified by 2 different manufacturers. (21 GE, 7 Siemens)  
Small plots: Average bias and SD for GE and Siemens scanners.

Siemens scanners.

### 3.3 Conclusions

The ACRIN data demonstrate appreciable temporal, axial, and radial variation in the reliability of reconstructed scan data. The temporal effects are mostly a function of decay and frame duration. Axial variation corresponds to reduction in the available numbers of cross-planes towards to the edge of the scanner. The radial effects are perhaps mostly a function of attenuation correction. Phantom based bias and variance profiles provide the opportunity to enhance the statistical basis for summarising ROI data, particularly whenever the ROI has a significant axial or radial extent. In such cases, a weighted mean of the ROI would be more reliable. While there is little overall difference between the axial, radial and

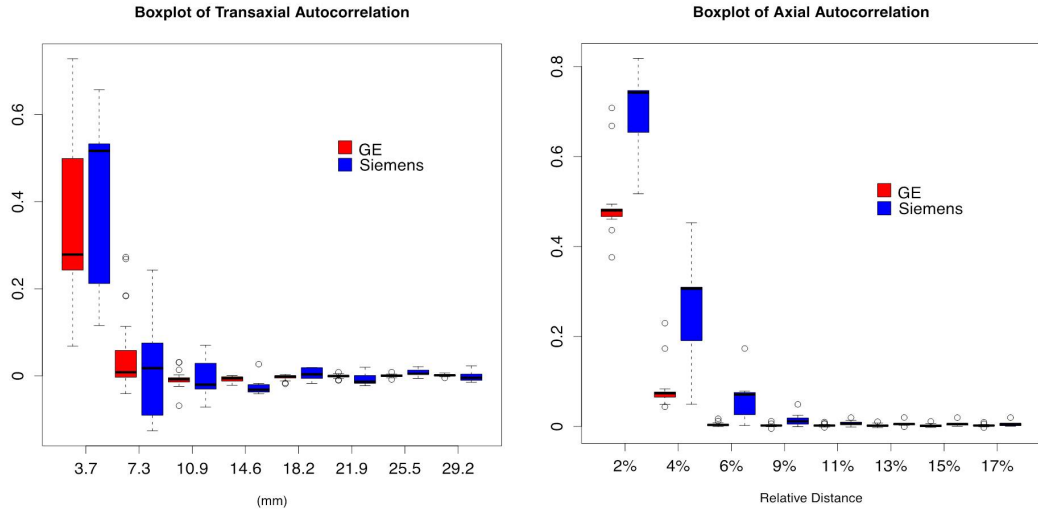


Figure 3.7: Boxplots of trans axial and axial autocorrelation on lag 2 to 9.

temporal variance patterns of the GE and Siemens scanners, we see a marked difference in the degree of persistence in the axial auto-correlation patterns. More detailed investigation of this phenomenon in the context of operationally used ACRIN type scanners is certainly warranted.

# Chapter 4

## The Gamma Characteristic of Reconstructed PET Data

### 4.1 Introduction

Positron emission tomography (PET) is widely used in the clinical management of many cancers—for staging, therapy planning and evaluation of therapy response. Improved understanding of the characteristics of PET imaging measurements could benefit clinical decision making. The analysis of statistical variation in PET data, and specifically the problem of approximating standard errors for regional means, has received considerable attention [2, 19, 46, 50, 62, 107]. Most of this work has necessarily concentrated on classical filtered-backprojection (FBP) reconstruction. With the widespread use of positivity constrained EM [115] reconstructions in clinical practice, the nature of the distribution of such reconstructions is receiving more careful attention. A basic result in probability is that sums of independent Poisson random variables are also Poisson. With PET the emission process can be viewed as a realisation of a Poisson process, and so the local weighted-averaging nature of classical reconstruction kernels theoretically implies a relation between the mean and variance of reconstructed values [46, 107]. This is a familiar characteristic of the Poisson and other distributions such as the Gamma and Log-normal. Many factors impact on the noise characteristics of reconstructed PET images and might lead to a deviation from the Poisson distribution: most obviously scaling but attenuation and scatter corrections add further complexities. Barret et al. [7] and Li [59] used simulations to examine noise characteristics of iterative algorithms and suggested that the probability density function for noise in iterative EM reconstructions could be approximated by a Log-normal law. Teymurazyan et al. [109] reported measurements on a

GEMINI PET/CT scanner comparing FBP and iterative EM reconstructions. While Gaussian characteristics were reasonable for FBP reconstructed data, the EM-reconstructed data were typically skewed. Their work suggested consideration of the Gamma distribution for representation of measurements. In cases where the reconstructed data are further analysed or quantitatively interpreted, as is the case in kinetic studies, the procedures used should ideally incorporate a good understanding of the statistical characteristics of the measurements in order that they be efficient [87]. In this context least-squares (or weighted least squares), which is efficient for Gaussian data, may not be efficient/optimal for Gamma or Log-normal data.

Motivated by experience with our own scanner, this work explores the Gamma model in greater detail and provides inference implications associated with such a representation of PET data. Post-reconstruction inference—model fitting and diagnostics for regions of interest—is of particular interest. Although the relevant Gamma parameterization is not within the framework of generalised linear models (GLM), iteratively reweighted least squares (IRLS) techniques, which are often used to find the maximum likelihood estimates of a GLM, can be adapted for analysis in this setting. IRLS techniques are described to implement likelihood inference based on the Gamma assumption. This makes essential use of approximations for the di-gamma and tri-gamma functions [1]. The development highlights use of the Gamma probability transform for creation of normalised residual diagnostics associated with such analyses. The methods are illustrated in the context of routine Quality Assurance (QA) studies used to evaluate the temporal and axial imaging characteristics of a scanner. Results are reported for data from a physical phantom imaging in an operational clinical scanner—a GE Discovery STE PET/CT. Figure 4.1 shows the picture of the phantom, which was taken by Dr. Stephen Stone at the PET/CT department in Cork University Hospital (CUH). Both traditional filtered back-projection (FBP) and EM reconstructions of the data are considered. Figures 4.2 (a) and (b) show images from all time frames for slice 23 in uniform phantom, reconstructed using FBP and OSEM methods. FBP data are quite Gaussian but the EM reconstruction exhibit Gamma-like skewness. Observed spatial covariance in this scanner is also used to guide numerical simulation studies.

Our work highlights the use of a Gamma-based probability transform in producing normalised residuals as statistical diagnostics. The approach is demonstrated for quality assurance analyses associated with physical phantom studies—recovering estimates of local bias and variance characteristics of an operational

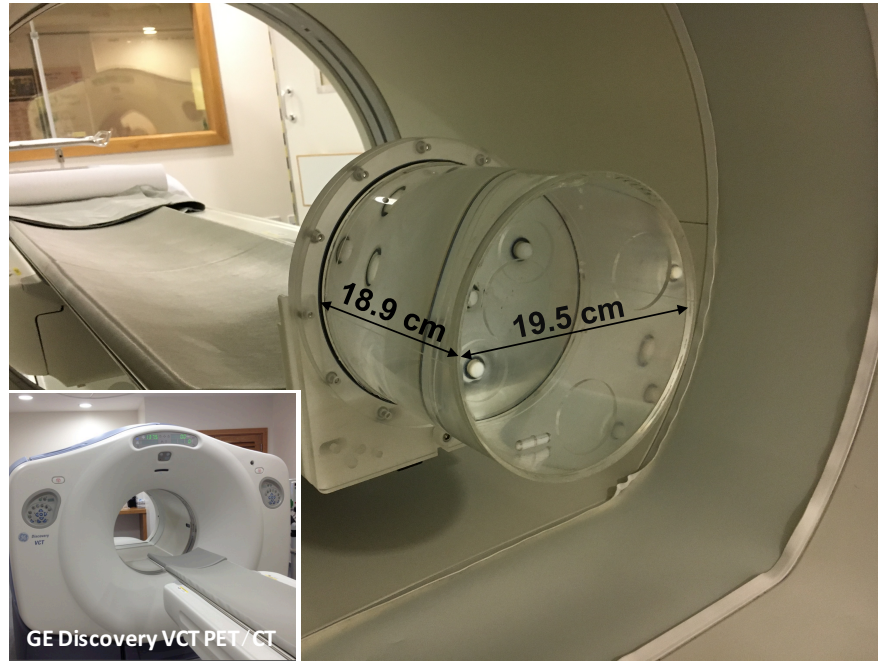


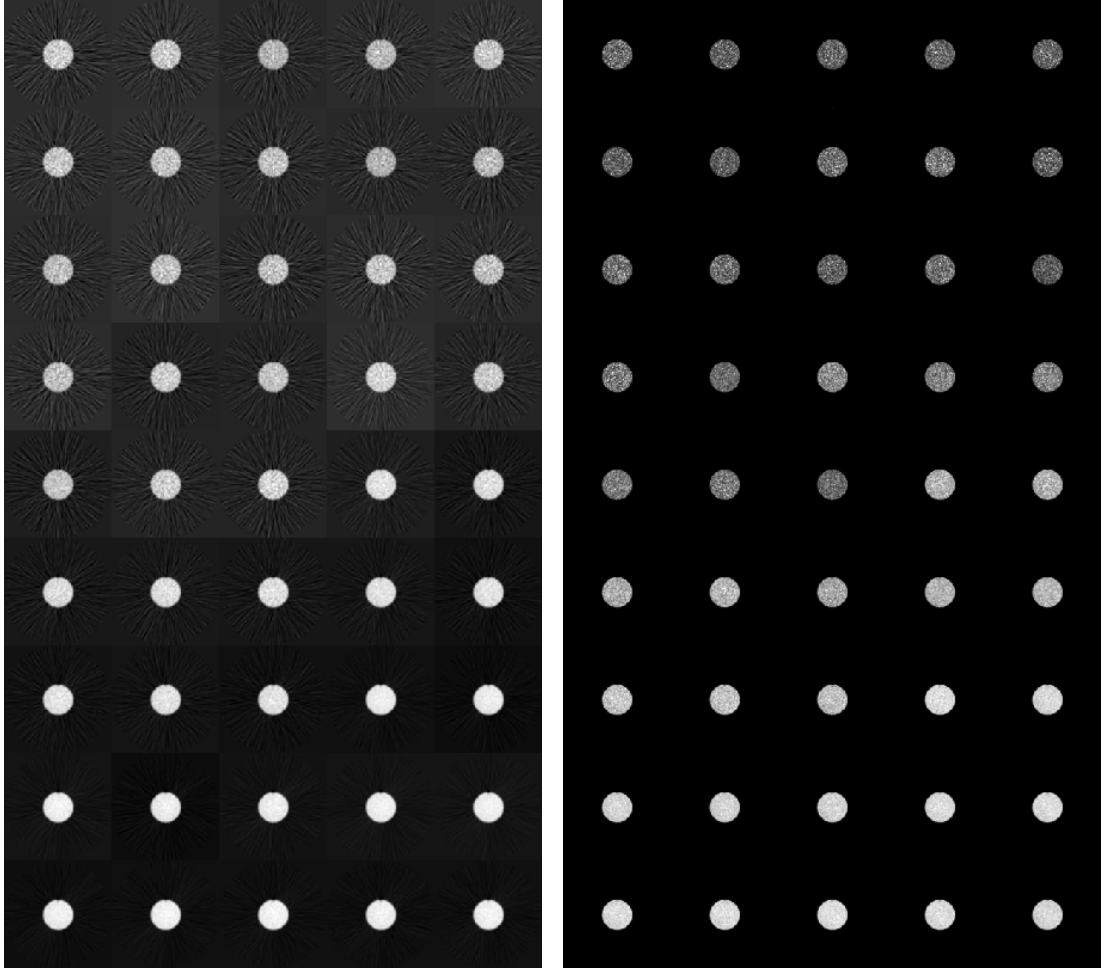
Figure 4.1: A uniform cylindrical phantom in PET/CT scanner.

scanner. Numerical simulations show that when the Gamma assumption is reasonable, gains in efficiency are obtained. The work shows that the adaptation of standard analysis methods to accommodate the Gamma structure is straightforward and beneficial.

This chapter starts with the introduction of Gamma distribution, this is followed by the basic theory and methodology in section 4.2. Studies with physical and simulated data are described in section 4.3. Section 4.4 presents data analysis for FBP and EM reconstructed data. This chapter concludes with discussion.

#### 4.1.1 Gamma Distribution

Gamma distribution was first formally introduced by Karl Pearson in the late 19th century, and was known as the Pearson type III distribution [67] until it was calling after the Gamma Function in the literature and textbooks, *e.g.*, C. E. Weatherburn [119]. This distribution, in statistics, is a family of continuous probability distributions with two positive parameters—a shape parameter  $\nu$  and a scale parameter  $\lambda$ . Sometimes an inverse scale parameter  $1/\lambda$  called rate parameter is used. As shown in Figure 4.3, a few of distributions which  $\nu = \tau$  and  $\lambda = 1/\tau$  are illustrated for different  $\tau$ -values. If a random variable  $X$  is



(a) Slice 23 (all time frames, 1 to 45) reconstructed with FBP.

(b) Slice 23 (all time frames, 1 to 45) reconstructed with OSEM.

Figure 4.2: Reconstructed images from the uniform phantom.

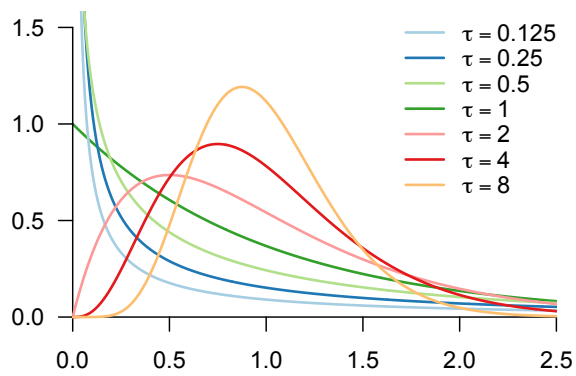


Figure 4.3: Densities of  $\text{Gamma}(\tau, 1/\tau)$  for different  $\tau$ -values.

Gamma-distributed with shape  $v$  and rate  $\lambda$ , it is denoted as

$$X \sim \text{Gamma}(v, \lambda)$$

The corresponding probability density function is given by

$$f(x; v, \lambda) = \frac{1}{\Gamma(v)\lambda^v} x^{v-1} e^{-\frac{x}{\lambda}}$$

where  $\Gamma(\cdot)$  is the Gamma Function,  $x > 0$  and  $v, \lambda > 0$ . The mean of the Gamma distribution is  $v\lambda$  and the variance is  $v\lambda^2$ .

It should be note that the Gamma distributed variables are positive and the results are typically skewed. Therefore, Gamma distribution is commonly used in meteorology (*e.g.*, rainfall [49]) and business (*e.g.*, insurance claims and loan defaults), for which the data are always positive. To the best of our knowledge, it is rarely used in characterising PET reconstructed data so far.

#### 4.1.2 Likelihood Ratio Test

As well known, both the Log-normal and Gamma distributions are efficient for analysing skewed non-negative data sets. Kundu and Manglick [57] provided a procedure to discriminate these two distributions using the ratio of the maximised likelihoods. In this section, we denote a Log-normal parameterisation as  $\log\text{Normal}(\delta, \rho)$  and a Gamma parameterisation as  $\text{Gamma}(v, \lambda)$ , where  $\delta$  and  $\rho$  respectively refer to the mean and standard deviation of the logarithm of the variables, and  $v$  and  $\lambda$  are the shape and scale parameters. The log-likelihood functions can be written as

$$\begin{aligned} L_{\log\text{Normal}}(\delta, \rho) &= \log \left( \prod_{i=1}^N f_{\log\text{Normal}}(x_i; \delta, \rho) \right), \\ L_{\text{Gamma}}(v, \lambda) &= \log \left( \prod_{i=1}^N f_{\text{Gamma}}(x_i; v, \lambda) \right). \end{aligned}$$

Then we define the ratio of the maximised likelihoods as

$$\text{Ratio} = \frac{L_{\text{Gamma}}(\hat{v}, \hat{\lambda})}{L_{\log\text{Normal}}(\hat{\delta}, \hat{\rho})}$$

where  $(\hat{v}, \hat{\lambda})$  and  $(\hat{\delta}, \hat{\rho})$  are the maximum likelihood estimators. Therefore, if  $\text{Ratio} > 1$ , the Gamma model would be preferred, otherwise, the Log-normal model is preferred.



### 4.1.3 Preliminary Analysis with ACRIN Series

Although our work is focus on the phantom data from CUH, a set of 43 PET scanners at different sites collected by the American College of Radiology Imaging Network (ACRIN) [98] are also considered as preliminary analysis. These data are from Quality Assurance (QA) studies for clinical cancer imaging trials followed a brain imaging protocol developed by the ACRIN. The data includes both FBP and iterative EM reconstructed images.

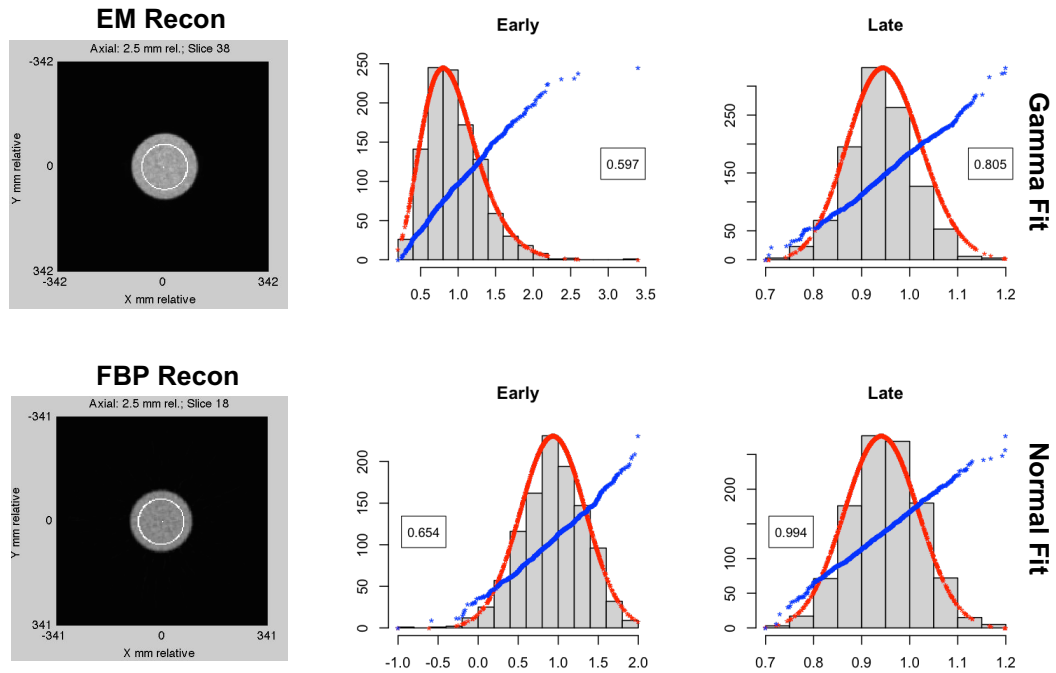


Figure 4.4: Gamma and Normal model fits for ACRIN physical phantom data.

Figure 4.4 shows the transverse images and histograms of two phantom datasets with different reconstruction methods. The histograms are showing the data from early and late time frames of the middle slice with the model fit (red) and Q-Q plots (blue)—Gamma model for EM reconstructed data and Normal model for FBP data. The values on each plots are the Kolmogorov–Smirnov test  $p$ -values. As shown on the plots, the fits are very good and the  $p$ -values suggest that the models are acceptable ( $p > 0.05$ ).

Since the result of the two particular sets shown in Figure 4.4 suggests Gamma model for EM reconstructed data and Normal model for FBP data, more evidence should be accumulated to support this result. Therefore, we applied the Kolmogorov–Smirnov test to all 43 datasets over all time frames and axial slices in order to see the behaviour of  $p$ -values across scanners and reconstruction methods. Figure 4.5 shows the Kolmogorov–Smirnov test  $p$ -values of Gamma model

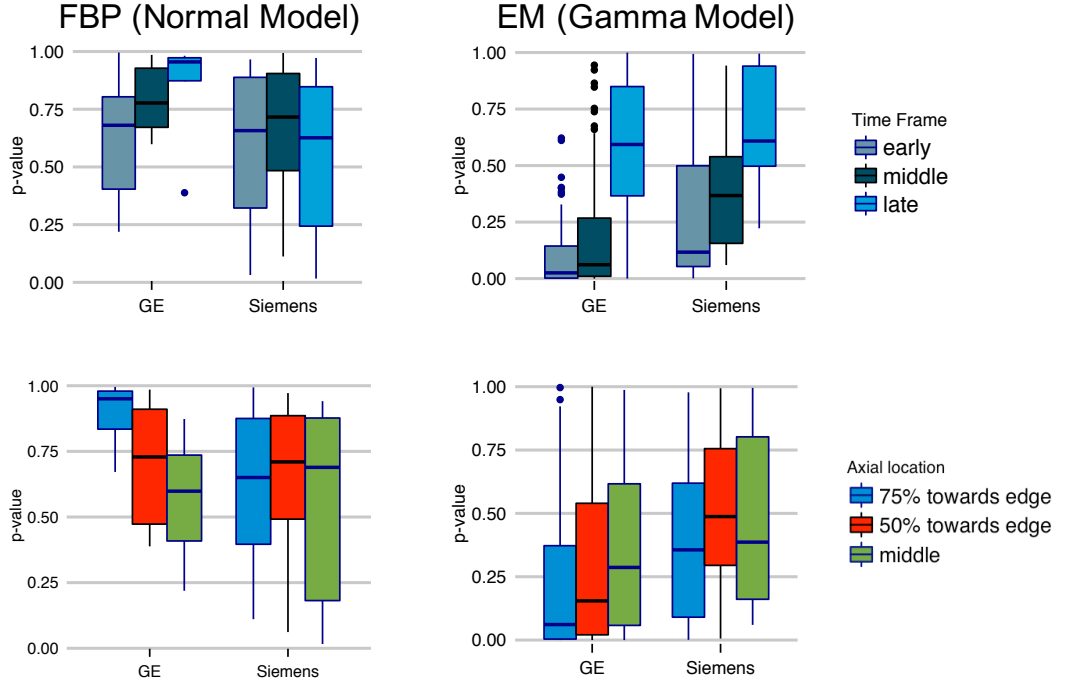


Figure 4.5: Kolmogorov–Smirnov test  $p$ -values of 43 ACRIN sets.

for EM data and Normal model for FBP data. The values are plotted by different time frames and axial locations and classified by manufacturer—GE or Siemens. For FBP data, it seems that Normal model is reasonable since all the  $p$ -values are above 0.05. The  $p$ -values of the data from GE scanners are increasing as time increases but decreasing as axial location moves towards middle whereas Siemens scanners do not show such behaviour. In the case of EM data, Gamma model is appropriate for all Siemens scanners ( $p > 0.05$ ), and also the data in late time frames of GE scanners. Although some of the  $p$ -values of Gamma model are less than 0.05 in early and middle time frames, Gamma model is still acceptable in most cases. This result gives us confidence to study distributional characteristics of EM reconstructed PET data using Gamma distribution.

## 4.2 Methodological Development

While reconstructed PET data are not integer counts they typically inherit the mean-variance property of the Poisson distribution [19, 62, 76, 95]. Positivity constrained EM reconstructions [115] effectively replace negative values with ones that are positive—inducing some skewness. As shown in Figure 4.3 the Gamma distribution, which has the flexibility to describe such data, is plausible in this setting. We use the parameterization  $\text{Gamma}(\tau_{\phi}^{\mu}, \phi)$  to represent reconstructed

PET activity values. This specifies a Gamma distribution with shape parameter  $\tau \frac{\mu}{\phi}$  and scale parameter  $\phi$ , the density function is

$$f(x|\tau, \mu, \phi) = \frac{1}{\Gamma(\tau \frac{\mu}{\phi}) \phi^{\frac{\tau \mu}{\phi}}} x^{\frac{\tau \mu}{\phi}-1} e^{-\frac{x}{\phi}}$$

where  $\Gamma(\cdot)$  is the gamma function. Here  $\tau$  corresponds to the injection dose. The mean and variance of the data will be  $\tau\mu$  and  $\tau\mu\phi$ , respectively. The parameter  $\phi$  represents over-dispersion relative to a Poisson random variable. In practice, such dispersion routinely arises from corrections for detector sensitivity, attenuation and scatter—but other factors such as patient movement may also play a role. Often PET measurements are scaled by the injected dose per weight of the patient for analysis, *e.g.*, converted into standardised uptake value (SUV) units [54]. If the counts are scaled by dose, they will have a  $\text{Gamma}(\tau \frac{\mu}{\phi}, \frac{\phi}{\tau})$  distribution—the mean is  $\mu$  and the variance is  $\mu\phi/\tau$ . Figure 4.3 shows  $\text{Gamma}(\tau\mu, 1/\tau)$  densities for different  $\tau$ -values with  $\mu = 1$ . When  $\tau \leq 1$ , the Gamma distributions have an exponential-like shape. The skewness reduces and the distribution formally converges to a Gaussian as the value of  $\tau$  or  $\frac{\mu\tau}{\phi}$  increases.

We address inference for a certain class of important models involving both temporal and spatial features, when the data have a Gamma structure. Complexity arises because our interest is focused on the mean and variance parameter, thus, unlike the estimation problem of the Gamma distribution in generalised linear models where the dispersion parameter  $\phi$  is a constant and considered as known/unknown nuisance parameter. As  $\mu$  and  $\phi$  are both of inferential interest, the exponential family structure and the familiar IRLS procedures, associated with the Gamma distribution in generalised linear models [65], do not apply.

### 4.2.1 Inference for Multiplicative Models in the Gamma Setting

Consider the situation where we have region of interest (ROI) time-course data. Hence, let  $z_{it}$ , for  $t = 1, 2, \dots, T$  and  $i = 1, 2, \dots, N$  be the set of voxel-level decay-corrected PET tracer activity values (scaled by injected dose) for a ROI with  $N$  voxels measured over  $T$  time-frames. Assuming the region is relatively homogeneous, we might reasonably expect a common temporal characteristic for the data in the ROI, *e.g.*,  $z_{it} \sim \text{Gamma}(\mu_t/\phi_t, \phi_t)$  with  $E(z_{it}) = \mu_t$  and  $\text{Var}(z_{it}) = \phi_t\mu_t$ . Assuming the duration of the  $t$ 'th time-frame of scanning is  $\Delta_t$  and the decay-correction factor for the  $t$ 'th time-frame is  $f_t$ , then  $\phi_t$  would be of

the form  $\phi \frac{f_t}{\Delta_t}$  [47]. In the case that the ROI extended over several slices or there were significant changes in sensitivity due to the attenuation of radiation, the model is readily adapted to take this into account. This leads to consideration of a general structure in which  $z_{ikt} \sim \text{Gamma}(\boldsymbol{\mu}_{kt}/\boldsymbol{\phi}_{kt}, \boldsymbol{\phi}_{kt})$  and

$$\boldsymbol{\mu}_{kt} = \alpha_k \mu_t \quad \text{and} \quad \boldsymbol{\phi}_{kt} = \beta_k \phi_t \quad (4.1)$$

where  $\boldsymbol{\mu}_{kt}$  and  $\boldsymbol{\phi}_{kt}$  decomposed as products of two terms depending on the slice  $k$  and time frame  $t$ , respectively. The relevant data structure is a set of PET measurements of the form  $\{z_{ikt}, i = 1, 2, \dots, N; k = 1, 2, \dots, K, t = 1, 2, \dots, T\}$  corresponding to a collection of  $N$  phantom-voxels each recorded over  $T$  time-frames on each of  $K$  transverse slices in the field of view of the scanner.

All component parameters are non-negative and we impose the additional constraints,  $\sum_t \mu_t = \sum_t \phi_t = 1$ , for identifiability.

While the above formulation connects to the ROI analysis of PET-measured tissue time-course data, it is relevant to analysis of physical phantom measurements used in routine quality assurance of PET scanners. This is discussed more fully below. For analysis purposes, we regard  $z_{ikt}$  for  $i = 1, 2, \dots, N$  as a random sample from a  $\text{Gamma}(\boldsymbol{\mu}_{kt}/\boldsymbol{\phi}_{kt}, \boldsymbol{\phi}_{kt})$  distribution in which the multiplicative constraints of equation (4.1) are in force. Previous reports on constructs of this type for PET data have been presented in [71, 72].

## Estimation

We consider use of a Gamma likelihood for estimation of parameters in the multiplicative model associated with the  $\{z_{ikt}\}$  data above. Assuming  $\{z_{ikt}\}$  are independent—certainly not true in the PET imaging context but still potentially useful as a *quasi-likelihood* device for producing reasonable estimators—the scaled negative log-likelihood function is:

$$l(\boldsymbol{\mu}, \boldsymbol{\phi}) = \sum_{ikt} \left\{ \frac{z_{ikt}}{\boldsymbol{\phi}_{kt}} - \frac{\boldsymbol{\mu}_{kt}}{\boldsymbol{\phi}_{kt}} \log\left(\frac{z_{ikt}}{\boldsymbol{\phi}_{kt}}\right) + \log(z_{ikt}) + \log\left(\Gamma\left(\frac{\boldsymbol{\mu}_{kt}}{\boldsymbol{\phi}_{kt}}\right)\right) \right\} \quad (4.2)$$

where  $\boldsymbol{\mu}_{kt}$  and  $\boldsymbol{\phi}_{kt}$  are specified by equation (4.1). An alternating procedure, updating  $(\alpha_k, \mu_t)$  with  $(\beta_k, \phi_t)$  fixed, followed by updating  $(\beta_k, \phi_t)$  with  $(\alpha_k, \mu_t)$  fixed, is used to minimise (4.2). This might be viewed as a variation of the  $\Pi$  method of Brieman [13]. We elaborate the details of the individual steps involved in the present setting.

**i) Updating  $(\alpha_k, \mu_t)$  with  $(\beta_k, \phi_t)$  fixed:** With  $\boldsymbol{\gamma} = (\gamma_1, \gamma_2, \dots, \gamma_T)$ , for  $\gamma_t = \mu_t/\phi_t$ ;  $\boldsymbol{\theta} = (\theta_1, \theta_2, \dots, \theta_K)$ , for  $\theta_k = \alpha_k/\beta_k$  and  $u_{ikt} = z_{ikt}/\phi_{kt}$ . The problem becomes minimising the following objective with respect to  $(\boldsymbol{\gamma}, \boldsymbol{\theta})$

$$l(\boldsymbol{\gamma}, \boldsymbol{\theta}) = \sum_k \sum_t -\gamma_t \theta_k \log(G_{kt}) + \log(\Gamma(\gamma_t \theta_k)) \quad (4.3)$$

where  $G_{kt} = \{\prod_i u_{ikt}\}^{1/N}$  is the geometric mean of the  $\{u_{ikt}, i = 1, 2, \dots, N\}$  data. Write  $\xi_{kt} = \theta_k \gamma_t$  and suppose  $\xi_{kt}^0 = \theta_k^0 \gamma_t^0 = (\alpha_k^0 \mu_t^0)/(\beta_k^0 \phi_t^0)$  where the super-script “0” indicates the current guess. Second order Taylor series expansion of the log-Gamma function gives

$$\begin{aligned} \log(\Gamma(\xi_{kt})) &\approx \log(\Gamma(\xi_{kt}^0)) + \psi(\xi_{kt}^0)(\xi_{kt} - \xi_{kt}^0) \\ &\quad + \frac{1}{2}\psi_1(\xi_{kt}^0)(\xi_{kt} - \xi_{kt}^0)^2 \end{aligned} \quad (4.4)$$

where  $\psi$  and  $\psi_1$  are the di-gamma and tri-gamma functions [1]. Substitution into (4.3), yields a quadratic approximation to objective function used for updating  $(\boldsymbol{\gamma}, \boldsymbol{\theta})$

$$\begin{aligned} WRSS(\boldsymbol{\gamma}, \boldsymbol{\theta}) &= \sum_k \sum_t w_{kt} (y_{kt} - \xi_{kt})^2 \\ &= \sum_k \sum_t w_{kt} (y_{kt} - \theta_k \gamma_t)^2 \end{aligned}$$

where

$$y_{kt} = \xi_{kt}^0 + \frac{\log(G_{kt}) - \psi(\xi_{kt}^0)}{\psi_1(\xi_{kt}^0)} \quad ; \quad w_{kt} = \psi_1(\xi_{kt}^0)$$

This gives the updating process—given  $\theta_k$ , update  $\gamma_t$  (normalising so that  $\sum_t \phi_t = 1$ ) and given  $\gamma_t$ , update  $\theta_k$

$$\begin{aligned} \hat{\gamma}_t &\leftarrow \frac{\sum_{k=1}^K w_{kt} \theta_k y_{kt}}{\sum_{k=1}^K w_{kt} \theta_k^2}, \quad t = 1, 2, \dots, T; \\ \hat{\theta}_k &\leftarrow \frac{\sum_{t=1}^T w_{kt} \gamma_t y_{kt}}{\sum_{t=1}^T w_{kt} \gamma_t^2}, \quad k = 1, 2, \dots, K. \end{aligned}$$

On convergence set  $\hat{\mu}_t = \hat{\gamma}_t \phi_t^0$  and  $\hat{\alpha}_k = \hat{\theta}_k \beta_k^0$ .

**ii) Updating**  $(\beta_k, \phi_t)$  **with**  $(\alpha_k, \mu_t)$  **fixed:** With  $\mu = \alpha_k \mu_t$ ,  $\zeta = \zeta_t \omega_k$ ,  $\zeta_t = 1/\phi_t$ ,  $\omega_k = 1/\beta_k$ , the objective function (4.2) can be expressed as

$$l(\mu, \zeta) = \sum_{ikt} \{ z_{ikt} \zeta_t \omega_k - \mu_{kt} \zeta_t \omega_k \log(z_{ikt} \zeta_t \omega_k) \\ + \log(z_{ikt}) + \log(\Gamma(\mu_{kt} \zeta_t \omega_k)) \} \quad (4.5)$$

Now hold  $\omega_k$  constant, and minimise (4.5) with respect to  $\zeta_t$ . The relevant first and second derivatives of  $l$  are

$$g(\zeta_t) = \frac{dl}{d\zeta_t} = \sum_{ik} \{ z_{ikt} \omega_k - \mu_{kt} \omega_k \log(z_{ikt} \zeta_t \omega_k) \\ - \mu_{kt} \omega_k + \mu_{kt} \omega_k \psi(\mu_{kt} \zeta_t \omega_k) \} \\ h(\zeta_t) = \frac{d^2 l}{d\zeta_t^2} = N \cdot \sum_k \mu_{kt} \omega_k \{ \mu_{kt} \omega_k \psi_1(\mu_{kt} \zeta_t \omega_k) - 1/\zeta_t \}$$

This gives the Newton updating process:  $\zeta_t^1 = \zeta_t^0 - g(\zeta_t^0)/h(\zeta_t^0)$ . On convergence,  $\hat{\phi}_t = 1/\hat{\zeta}_t$  and scaled so that  $\sum_t \hat{\phi}_t = 1$ .

With  $\zeta_t$  (equivalently  $\phi_t$ ) fixed, the Newton process for updating  $\omega_k$  proceeds as:  $\omega_k^1 = \omega_k^0 - g(\omega_k^0)/h(\omega_k^0)$  where

$$g(\omega_k) = \frac{dl}{d\omega_k} = \sum_{it} \{ z_{ikt} \zeta_t - \mu_{kt} \zeta_t \log(z_{ikt} \zeta_t \omega_k) \\ - \mu_{kt} \zeta_t + \mu_{kt} \zeta_t \psi(\mu_{kt} \zeta_t \omega_k) \} \\ h(\omega_k) = \frac{d^2 l}{d\omega_k^2} = N \cdot \sum_t \mu_{kt} \zeta_t \{ \mu_{kt} \zeta_t \psi_1(\mu_{kt} \zeta_t \omega_k) - 1/\omega_k \}$$

On convergence,  $\hat{\beta}_k = 1/\hat{\omega}_k$ . We update  $\mu_t$ ,  $\alpha_k$  and  $\phi_t$ ,  $\beta_k$  sequentially by iterating the procedures in **i)** and **ii)** above. The iterative process continues until relative errors are lower than the specified tolerance.

$$\varepsilon_\mu = \left\| \frac{\mu_{kt}^n - \mu_{kt}^{n-1}}{\mu_{kt}^n} \right\| < 0.001 ; \quad \varepsilon_\phi = \left\| \frac{\phi_{kt}^n - \phi_{kt}^{n-1}}{\phi_{kt}^n} \right\| < 0.001$$

The process is initialised in a simplified least squares (LS) way, alternating between the following two steps for  $\mu$  and  $\alpha$ —with starting values  $\tilde{\mu}_t = \frac{1}{N \times K} \sum_{i=1}^N \sum_{k=1}^K z_{ikt}$

- $\tilde{\alpha}_k = \frac{\frac{1}{N} \sum_{it} z_{ikt} \tilde{\mu}_t}{\sum_t \tilde{\mu}_t^2}$
- $\tilde{\mu}_t = \frac{\frac{1}{N} \sum_{ik} z_{ikt} \tilde{\alpha}_k}{\sum_k \tilde{\alpha}_k^2}$ , normalising so that  $\sum_t \tilde{\mu}_t = 1$ .

This is followed by setting  $y_{ikt} = (z_{ikt} - \tilde{\alpha}_k \tilde{\mu}_t) / \sqrt{\tilde{\alpha}_k \tilde{\mu}_t}$  and alternating the two steps

- $\tilde{\beta}_k = \frac{\frac{1}{N} \sum_{it} y_{ikt}^2 \tilde{\phi}_t}{\sum_t \tilde{\phi}_t^2}$
- $\tilde{\phi}_t = \frac{\frac{1}{N} \sum_{ik} y_{ikt}^2 \tilde{\beta}_k}{\sum_k \tilde{\beta}_k^2}$ , normalising so that  $\sum_t \tilde{\phi}_t = 1$

for determining  $\phi$  and  $\beta$ . In this setting, IRLS is equivalent to Newton's method and can therefore be expected to benefit from its convergence properties [65]. The process is self-consistent in the sense that if the parameters are set at the true values, any of the individual updating steps is unbiased for the target. We evaluate the efficiency of these simplified estimators in results section.

#### 4.2.2 Probability Transformed Normalised Residuals

Let  $F(\cdot|\mu, \phi)$  be the cumulative distribution for a Gamma random variable  $Z$  with density  $\text{Gamma}(\mu/\phi, \phi)$ . Consider the probability transformation of  $Z$

$$R = \Phi^{-1}(F(Z|\mu, \phi))$$

where  $\Phi^{-1}$  is inverse cumulative distribution function of a standard Gaussian. Theoretically,  $R$  must have a standard normal distribution—Figure 4.6. If the model is correct, the probability-transformed data might be considered as realisations from a Normal distribution.

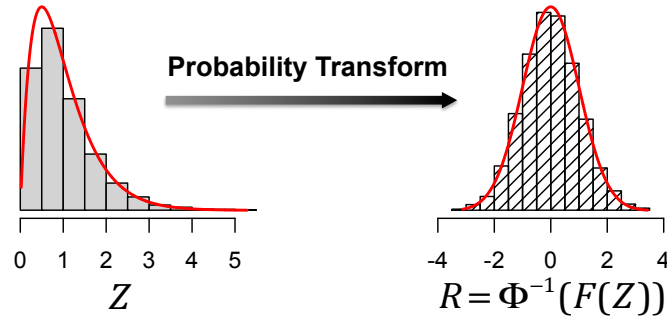


Figure 4.6: Theoretical probability transformation of a Gamma random variable ( $Z$ ) with distribution function  $F$  to a Normal random variable  $R$ .

In the context of the multiplicative model, where  $\mu_{kt}$  and  $\phi_{kt}$  are estimated, we can use this to construct a set of normalised model residuals for the analysis

$$r_{ikt} = \Phi^{-1}(F(z_{ikt}|\hat{\mu}_{kt}, \hat{\phi}_{kt}))$$

for  $i = 1, 2, \dots, N$ ,  $k = 1, 2, \dots, K$  and  $t = 1, 2, \dots, T$ . If the model is appropriate, these residuals should conform to the assumptions of a random sample from a standard normal distribution. There is of course considerable experience with similar residual diagnostics in the context of the linear model—see Weisberg [120] for example. It is worth noting that as  $\hat{\mu}_{kt}/\hat{\phi}_{kt}$  increases,  $z_{ikt}$  becomes Gaussian and the normalised residuals take the familiar form

$$r_{ikt} \approx \frac{z_{ikt} - \hat{\mu}_{kt}}{\sqrt{\hat{\phi}_{kt}\hat{\mu}_{kt}}}.$$

Thus the probability-transformed Gamma model residuals reduce to Pearson residuals as  $\hat{\mu}_{kt}/\hat{\phi}_{kt}$  increases—*c.f.* generalised linear models [65]. It should be appreciated that transformation to the Normal distribution for residual diagnostics is somewhat arbitrary, a referee has suggested transforming to a uniform distribution.

## 4.3 Experimental Methods

### 4.3.1 Physical Phantom Data

A standard part of routine quality assurance for PET scanners involves evaluating accuracy and reliability from imaging of a known source. A range of phantoms and imaging protocols, matched to operational clinical practice, are used for this. We consider the data of this type collected at a PET imaging facility at a local hospital—the Cork University Hospital. The scanner is a GE Discovery STE used clinically for imaging of cancer patients. Routine clinical image reconstruction is performed with 3-D iterative EM reconstruction (IR). Classical linear 3-D Fourier rebinning filtered-backprojection reconstructions (FBP) are also produced. In our study, an uniform cylindrical phantom filled with F-18 radiotracer is placed in the scanner and imaged in accordance with a standard dynamic PET-FDG brain imaging protocol established by the CQIE project of the American College of Radiology Imaging Network (ACRIN) [98]. The brain imaging field of view (FOV) for PET is 700 mm trans-axially and 157 mm axially. The phantom is 215 mm in diameter and placed centrally so that its axis aligns with the long-axis of the scanner. A dynamic sequence of 45 time-frames is acquired for 55 minutes. For each time-frame, the reconstructed image has  $128 \times 128$  pixels in 45 slices, with the pixel size of  $5.47 \times 5.47 \text{ mm}^2$  and slice thickness of 3.27 mm. The dimension of the full 4-D phantom image data set is  $128 \times 128 \times 45 \times 45$ . The ROI



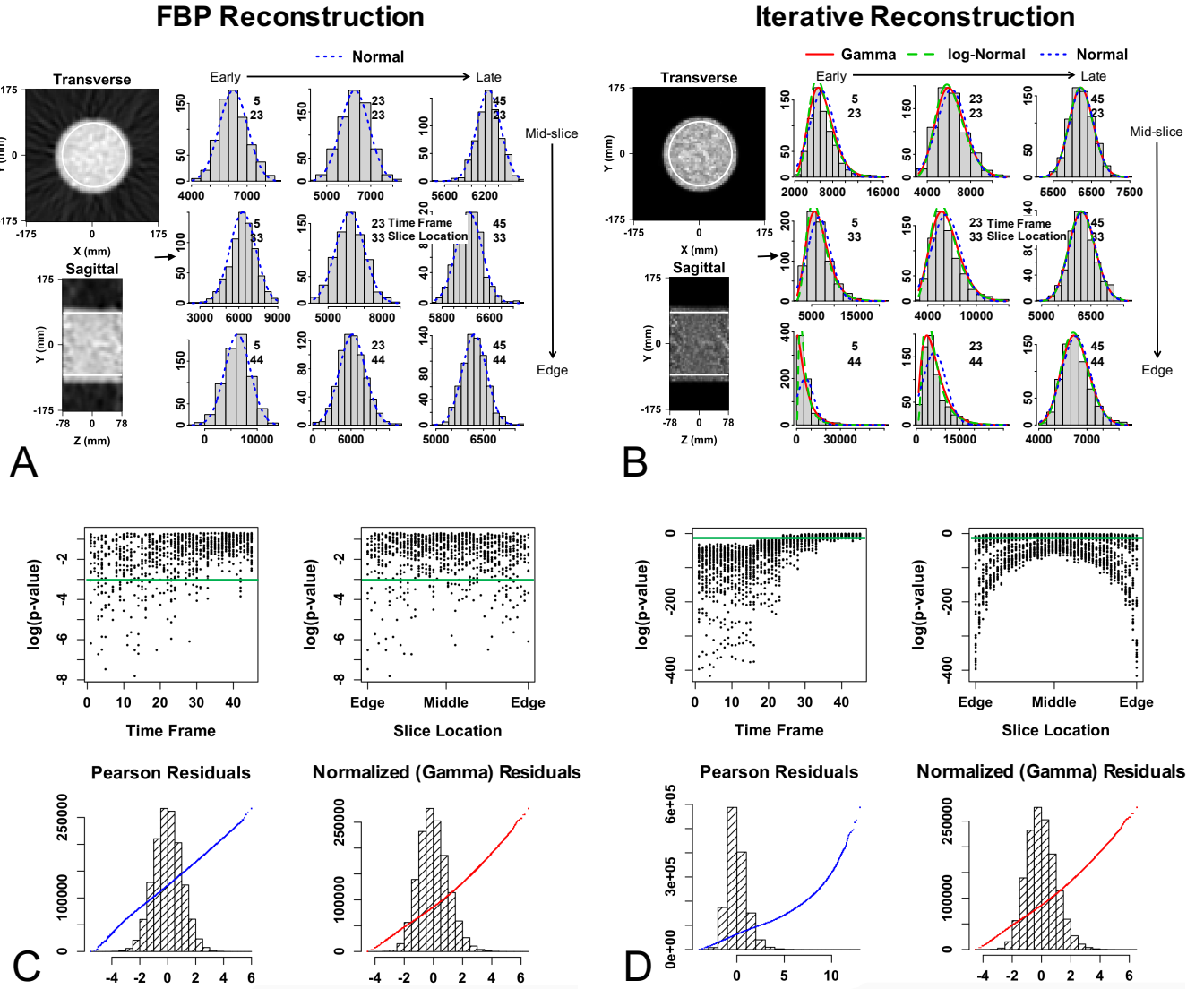


Figure 4.7: 3D dynamic PET study on a cylindrical phantom using FBP (A,C) and EM (IR) (B,D) reconstructed methods. The ROI data within white outline are used in analysis. **Figure A and B:** Left: The cross-section and sagittal image of the phantom data (24th time frame of slice 23). Right: Histograms generated from ROIs on different time frames and slices. The lines on the plots are Gamma (red), Log-normal (green) and Normal (blue) model fits for particular time and slice combinations of ROI data. **Figure C and D:** Top:  $\chi^2$  p-values (log-scale) calculated for each time and slice combinations and plotted by time frame and slice location. The green lines indicate the significant level—0.05. Bottom: Histograms and normal Q-Q plots of Pearson residuals (left blue) and normalised Gamma residuals (right red) for entire phantom data.

data for the interior cross-sectional circular volume of the phantom, acquired for each axial slice,  $k$ , and time-frame,  $t$ , are available for analysis. There are  $N = 680$  voxels in the ROI. The data for the set of all  $K = 45$  slices and  $T = 45$  time-frames structured as  $\{z_{ikt}, i = 1, 2, \dots, N, k = 1, 2, \dots, K, t = 1, 2, \dots, T\}$ . These measurements are decay-corrected and scaled by the known dose per unit volume within the phantom. The perfect scanner would have  $z$ -values close to unity throughout. We use these data to evaluate the plausibility of the Gamma distribution versus the more conventional Gaussian assumption. We go on to use the multiplicative model to analyse the axial and temporal patterns in the bias and variance of measurements. Note that the central placement and small diameter of the phantom, makes radial effects negligible in this setting.

***i) Assessment of the Gamma and Log-normal Distributions:*** The cross-sectional voxel-data for each time-frame and slice are evaluated for conformity to a Gaussian, Gamma and Log-normal law. The Gamma and Log-normal model are estimated using the function `fitdistr` in R [116]. The likelihood ratio statistic comparing twice the negative log-likelihood of the best fitting Gaussian model is compared to twice the negative log-likelihood for the best fitting Gamma model.

$$\begin{aligned} D &= -2 \log \left( \frac{\text{likelihood for Gaussian model}}{\text{likelihood for Gamma model}} \right) \\ &= -2 (\log(\text{likelihood for Gaussian model}) - \log(\text{likelihood for Gamma model})) \end{aligned}$$

From standard parametric likelihood theory, we would expect that if the models were equally valid the deviation  $D$  of the Gamma model log-likelihood from the Gaussian log-likelihood should be on the order of a  $\chi_2^2$  random variable. To formally assess the strength of evidence in favour of the Gamma model, we compute the difference between the Gaussian log-likelihood and the Gamma model log-likelihood and evaluate the probability ( $p$ -value) that a  $\chi_2^2$  random variable could be more than the computed amount. Whether the Gamma fit is significantly better can be suggested by deriving the  $p$ -value of the deviation  $D$ . The null hypothesis of this test should be the two models are equally valid for the data. Note that the analysis of  $p$ -value here is aiming to provide an empirical understanding of the difference between the two models across slices and time frames. It is not the case that taking  $p$ -value as an evidence against the Gaussian model. This calculation is carried out individually for each slice and time-frame combination. A graphical comparison between the Gamma and Gaussian is also carried out.

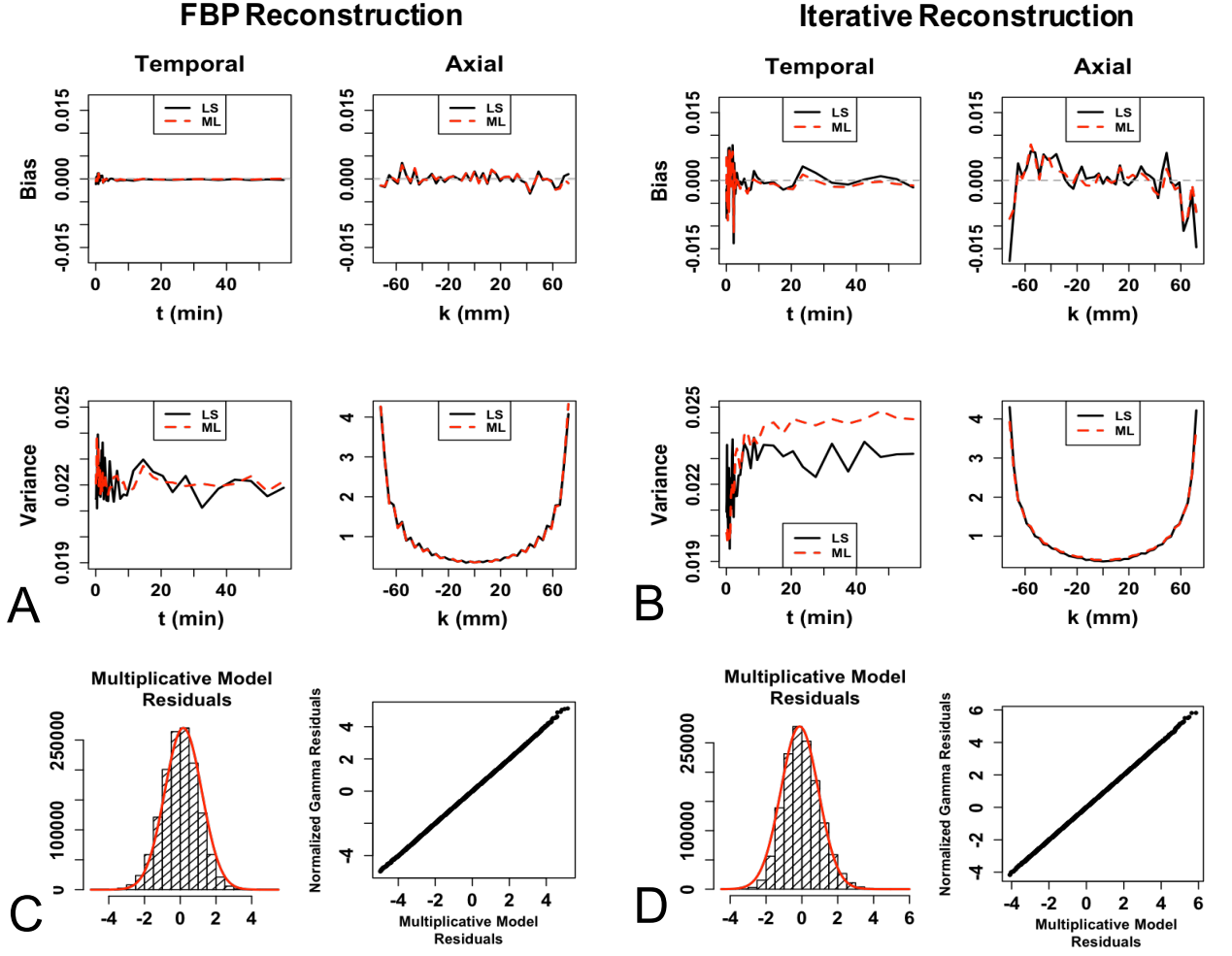


Figure 4.8: Multiplicative model fit on FBP (A,C) and EM (iterative) (B,D) reconstructed PET data. **Figure A and B:** Multiplicative model estimates of bias and variance using Least Square (LS) versus Maximum Likelihood (ML) estimation. **Figure C and D:** show multiplicative model residuals and the Q-Q plot of normalised Gamma residuals with and without the multiplicative constraint.

This is based on the overall structure of probability transformed residuals under Gamma and Gaussian model assumptions for the data. The likelihood ratio of the Gamma and Log-normal fits are also evaluated. These are summarised by the duration of the time-frame.

**ii) Application of the Multiplicative Model:** The model described in section 4.2 is used to evaluate the axial and temporal bias and variance. The Gamma model fit is compared to the fit achieved using the simplified least squares approach—optimal under Gaussian assumptions. In addition, the normalised

residuals are analysed and compared to the corresponding residuals obtained without the multiplicative modelling constraints.

### 4.3.2 Numerical Phantom Study

A numerical phantom study was conducted to explore effects of iteration and count rate on the noise distribution characteristics of EM reconstructed images. The 2-D uniform elliptical disk phantom, shown in Figure 4.9, was used. The simulation model was based on simple analytical projection. One thousand replicates of Poisson simulated projection data were created with counts rates from  $10^4$  to  $10^6$  events. This lead to a collection of 1000 reconstructed images for each count rate. The central pixel value over these sets were evaluated for conformity to Gamma and Log-normal distributions.

### 4.3.3 Numerical Simulation with the Gamma Model

Our study here investigates the performance of the method proposed in section 4.2 for estimation of the accuracy ( $\mu_{kt}$ ) and dispersion ( $\phi_{kt}$ ) characteristics. Data were simulated according to

$$z_{ikt} \sim \text{Gamma}\left(\tau \frac{\mu_{kt}}{\phi_{kt}}, \phi_{kt}/\tau\right)$$

for  $i = 1, \dots, N$ ,  $k = 1, \dots, K$ , and  $t = 1, \dots, T$ , with  $\mu_{kt} = \alpha_k \mu_t$ ,  $\phi_{kt} = \beta_k \phi_t$  and the values of  $\mu_t$ ,  $\alpha_k$ ,  $\phi_t$  and  $\beta_k$ , matched to typical patterns observed in the CUH phantom data. A range of dose levels  $\tau$  and ROI sizes  $N$  are considered. The dose ranges are set to explore values which would be one to two orders of magnitude greater and less than that seen in the CUH sets. The ROI sizes of  $N = 10, 100, 1000$  were considered. Mean square errors (MSE) for the component parameters,  $\mu_t$ ,  $\alpha_k$ ,  $\phi_t$  and  $\beta_k$ , are evaluated as function of dose and ROI size.

## 4.4 Results

We begin by presenting results of the analysis of physical phantom data, this is followed by numerical simulation studies.

### 4.4.1 Physical Phantom Data

***i) Temporal and Spatial Data Distribution:*** Figure 4.7 A and B shows images of slice 23 and time frame 24 located near the centre of the phantom,

which are reconstructed using FBP and IR methods, respectively. Voxel-level data in a cylindrical volume, within white outline, are used in analysis. The ROI histograms with the best fitting Normal model (blue dotted lines), Gamma model (red lines) and Log-normal model (green dashed lines) for the data in different slices and time frames are also exhibited in Figure 4.7 A and B. In the present study, the FBP data show no skewness supporting the Gaussian distribution consistent with previous studies [109]. By contrast, the IR data show skewness particularly in the early time frames (Figure 4.7 B) and towards the axial limits (edge) of the scanner. However, for data in late time frames and towards the middle of the scanner the skewness disappears and there is convergence to the Normal distribution. The red lines in this plot indicate that the IR data can be approximated by the Gamma model, while the blue dashed lines show that the Normal model fails to describe the IR data in early time frames. The Log-normal model appears similar to the Gamma model for most slices. The detailed analysis of discrimination between the Log-normal and Gamma model will be presented in section 4.5. Since the measurable count rate ( $\tau$ ) diminishes with decay (time) and sensitivity (axial extremity), the data shown in Figure 4.7 agree with the structure of  $\text{Gamma}(\tau_{\phi}^{\mu}, \phi/\tau)$  distribution—showing less skewness as  $\tau$  increases (see Figure 4.3).

**ii) Comparison of Gaussian and Gamma model:** The top row of Figure 4.7 C and D, plots  $\chi^2_2$  p-values ( $p_{kt}$ ) by slice location ( $k$ ) and time frame ( $t$ ). This calculation has been described in 4.3.1 i). For FBP data, the majority of p-values are in the range of 0.05 to 1 and there is no obvious temporal or axial pattern. Overall there is no significant difference between the Gaussian model fit and Gamma model fit for FBP data. With the IR data, there is strong evidence against the Gaussian model at early time frames and in extreme axial slices. These areas have less counts and show more skewness. The probability transformations of FBP and IR data are shown on the bottom row of C and D, respectively. The plots on the left showing the histograms and Normal quantile-quantile plots (Q-Q plots) of Pearson residuals  $r_{ikt}^G = (z_{ikt} - \mu_{kt}^*)/\sigma_{kt}^*$ , where  $\mu_{kt}^*$  and  $\sigma_{kt}^*$  are the means and variances of each slice and time-frame combination. On the bottom right of C and D shown the histograms and Normal Q-Q plots of normalised Gamma residuals  $r_{ikt}^{\Gamma} = \Phi^{-1}(F(z_{ikt}|\hat{\mu}_{kt}^*, \hat{\phi}_{kt}^*))$ , where  $\hat{\mu}_{kt}^*$  and  $\hat{\phi}_{kt}^*$  are obtained by fitting Gamma distribution for each slice and time-frame combination using `fitdistr` function in R. Both Pearson and Gamma residuals of FBP data appear Gaussian, suggesting that either model is reasonable. However the Gamma residuals of IR

data are strongly Gaussian in comparison to the Pearson residuals, favouring the Gamma model. To sum up, the Gamma model is superior to the Gaussian for iterative reconstructed PET data, but both models are equivalent for FBP data.

***iii) Evaluation of Temporal and Spatial Scanning Characteristics:***

The maximum likelihood (ML) estimation, described in section 4.2, is used to evaluate the axial and temporal bias and variance. The ML fit is compared to the fit achieved using the least squares (LS) approach. Note LS estimates are used as initial values for the ML computation. The estimated bias and variance using LS and ML method are shown in Figure 4.8 A and B, respectively. For FBP reconstruction, the bias remains stable and stays near zero temporally and axially while the variance shows more fluctuations at the early time. In the case of IR reconstruction, the bias and variance show more fluctuations than in FBP. The variance shows some increase over time. Both FBP and IR data show a strong axial pattern of variance—low variance in the centre of the scanner and high variance towards axial edge. There is no significant difference between LS and ML estimates for FBP data, but the ML estimates for IR data tend to fluctuate less than the LS estimates. Since the true variances are unknown, it is not possible to compare the accuracy of two estimates here, however our simulation study, which is reported in 4.4.3 below, would suggest the ML estimation should be more reliable. C and D show the probability transformation (multiplicative model residuals) and Q-Q plot of normalised Gamma residuals with and without the multiplicative constraint. The linear patterns of Q-Q plots suggest that the distribution of multiplicative model residuals  $r_{ikt}$  (with the constraint) and normalized Gamma residuals  $r_{ikt}^{\Gamma}$  (without the constraint) are similar. To formally assess the performance of these two models, we computed the  $F$  statistic of the residuals.

$$F = \frac{\text{RSS}_1 - \text{RSS}_2}{p_2 - p_1} / \frac{\text{RSS}_2}{n - p_2}$$

where the subscripts 1 and 2 are indexes for the multiplicative model (with the constraint) and the full model (without the constraint) respectively.  $\text{RSS}_i$  is the residual sum of squares of model  $i$ .  $p_i$  is the number of parameters for model  $i$ ,  $p_2 > p_1$ .  $n$  is the number of data points to estimate parameters of both models. The null hypothesis  $H_0$ : the full model does not significantly fit better than the multiplicative model, is accepted since  $F = 1.05$  does not exceed the critical value of 1.52— $F$  distribution with  $(p_2 - p_1, n - p_2)$  degrees of freedom for false-rejection probability of 0.05.

### 4.4.2 Numerical Phantom Simulation

Phantom data results are shown in Figure 4.9. Higher skewness is seen at the lower counts. The red solid lines in Figure 4.9 represent fits of Gamma distributions to the measured data. The fits are very reasonable. The Log-normal shows similar fits to the data (green broken lines). Figure 4.9 demonstrates that the distribution of the measured data becomes closer to the Normal distribution as count rate increases. The result suggests that measured data becomes closer to the Normal distribution as count rate increases, in agreement with analysis of physical phantom data.

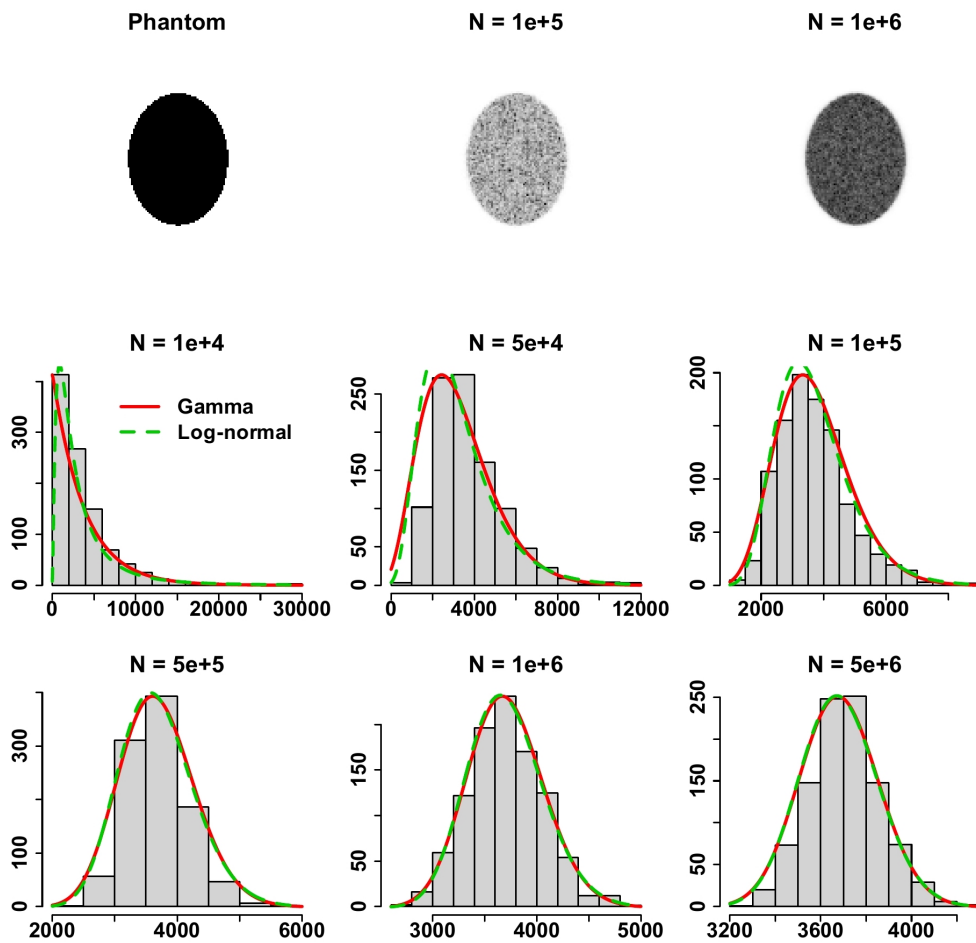


Figure 4.9: Results of numerical phantom simulation study. Top: Phantom image and EM reconstructed images for two count rates ( $N = 10^5$  and  $N = 10^6$ ). Middle and bottom: Histograms of pixel values for different count rates. The Gamma and Log-normal model fits are shown in red and green, respectively.

### 4.4.3 Numerical Simulation with the Gamma Model

The simulated data were generated as described in section 5.2.6. The top row of Figure 4.10 shows the overall histogram of Pearson residuals  $r_{ikt}^G$  for 3 different values of  $\tau$  for a simulated dataset ( $N = 1000$ ). The Pearson residuals become more Gaussian distributed as  $\tau$  increases. This result agrees with the property of Gamma distribution as shown in Figure 4.3. The bottom row shows the Gamma model residuals  $r_{ikt}$  for the same dataset. The Gamma-transformed residuals are strongly Gaussian in comparison to the Pearson residuals.

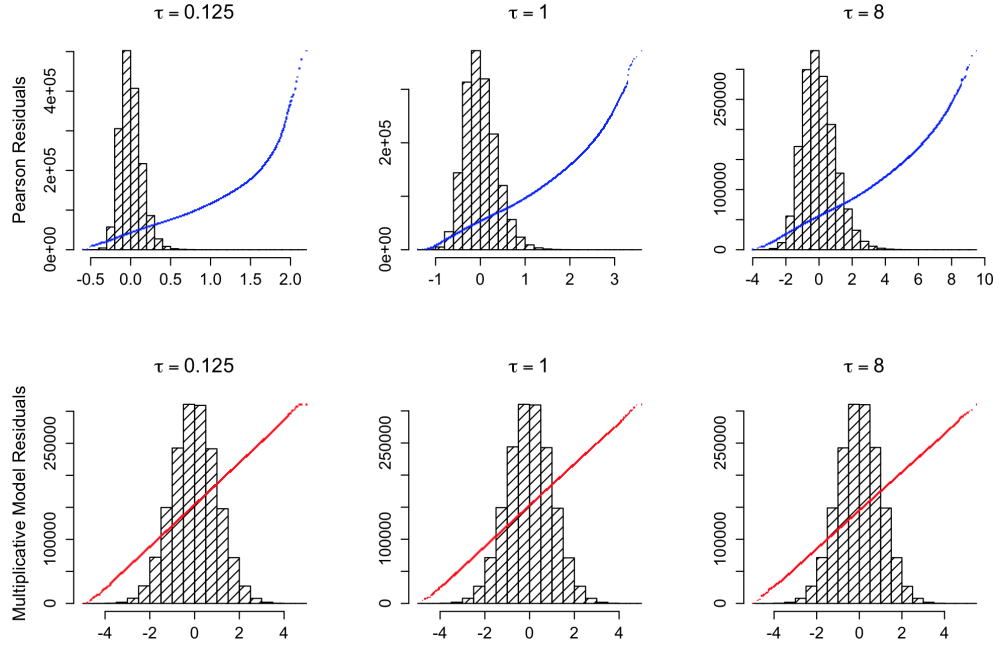


Figure 4.10: Histograms and normal Q-Q plots (dots) of the Pearson (top) and Gamma-transformed residuals (bottom) for different  $\tau$  values.

Considering the data with same dose  $\tau = 1$ , Figure 4.11 compares the initial least squares estimates (blue)— $\tilde{\mu}_t$ ,  $\tilde{\alpha}_k$ ,  $\tilde{\phi}_t$ ,  $\tilde{\beta}_k$  with the multiplicative model/maximum likelihood estimates (red)— $\hat{\mu}_t$ ,  $\hat{\alpha}_k$ ,  $\hat{\phi}_t$ ,  $\hat{\beta}_k$ . The ML estimates follow the true values more closely indicating that the Gamma distribution-based multiplicative model improves the accuracy of estimation.

Figure 4.12 shows the log mean square error (MSE) of the component ML (red) and LS (blue) parameter estimation evaluated as a function of the dose  $\tau$  and ROI size  $N$ . The results indicate that compared to LS, ML estimates have reduced MSEs. The amount of reduction depends on  $\tau$ ,  $N$  and the parameter being estimated. The percentage reductions of MSE for  $\mu_t$  and  $\alpha_k$  are 2% and 78%, respectively, with  $\tau = 1$  and  $N = 1000$ —these values match the physical phantom data. The MSE reduction of  $\phi_t$  and  $\beta_k$  are higher, 96% and 95%. The



compute time for ML is about four times that of the LS estimation method—for a sample size of  $N = 1000$  the total compute time was 111 seconds on a laptop with a 2.9 GHz processor. The results also show that the estimation is consistent as  $\tau$  and  $N$  increase. The empirical rate of convergence of the MSE of the mean value parameters  $\mu_t$  and  $\alpha_k$ , was analysed by linear regression using the model,  $\log(MSE) \sim a_0 + a_1 \log(N) + a_2 \log(\tau)$ . The regression lines are shown on the plot. The estimated regression coefficients  $\hat{a}_0$ ,  $\hat{a}_1$  and  $\hat{a}_2$  of the log MSE of the ML estimation of  $\mu_t$  and  $\alpha_k$  are presented in Table 5.1. The empirical behaviour MSE of ML estimation for  $\phi_t$ ,  $\beta_k$  shows a rate change close to  $\tau = 1$ . After  $\tau = 1$  the MSE shows little improvement with increasing  $\tau$ . In light of this regression separate lines were fitted for  $\tau \leq 1$  and  $\tau \geq 1$ , respectively. The estimated regression coefficients are given in Table 4.2. An asymptotic explanation of the behaviour is offered in the next section.

Table 4.1: Empirical MSE estimation characteristic for  $\mu_t$  and  $\alpha_k$   $\log(MSE) \sim a_0 + a_1 \log(N) + a_2 \log(\tau)$

	$\mu_t$	$\alpha_k$
$\hat{a}_0$	$-4.727 \pm 0.243$	$-5.969 \pm 0.172$
$\hat{a}_1$	$-0.818 \pm 0.049$	$-0.893 \pm 0.035$
$\hat{a}_2$	$-1.311 \pm 0.066$	$-1.135 \pm 0.047$

Table 4.2: Empirical MSE estimation characteristic for  $\phi_t$  and  $\beta_k$   $\log(MSE) \sim a_0 + a_1 \log(N) + a_2 \log(\tau)$

		$\phi_t$	$\beta_k$
$\tau \leq 1$	$\hat{a}_0$	$-3.685 \pm 0.278$	$-3.578 \pm 0.420$
	$\hat{a}_1$	$-0.579 \pm 0.050$	$-0.755 \pm 0.075$
	$\hat{a}_2$	$-1.004 \pm 0.121$	$-0.686 \pm 0.183$
$\tau \geq 1$	$\hat{a}_0$	$-3.359 \pm 0.434$	$-2.449 \pm 0.185$
	$\hat{a}_1$	$-0.625 \pm 0.064$	$-1.013 \pm 0.027$
	$\hat{a}_2$	$-0.127 \pm 0.213$	$-0.067 \pm 0.091$

## 4.5 Discussion

Using Q-Q plots and less formal statistical methods, Teymurazyan et al. [109] showed that the noise in RAMLA-reconstructed PET images was well characterised by the Gamma distribution while FBP reconstructions produced comparable conformity with both Normal and Gamma statistics. This study uses a

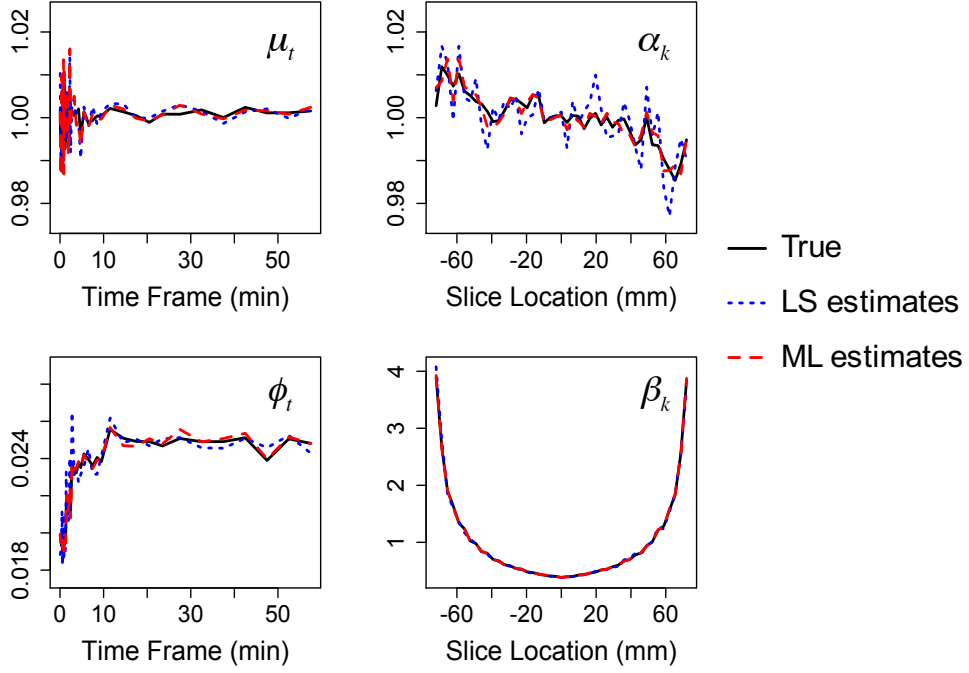


Figure 4.11: Initial (LS) and multiplicative (ML) estimates for  $\mu_t$ ,  $\alpha_k$ ,  $\phi_t$  and  $\beta_k$  when  $\tau = 1$ .

more formal likelihood based approach to investigate evidence in support of the Gamma model in the EM and FBP reconstructed data. The test method is applied to QA data from a phantom study obtained from a PET scanner in routine clinical use. The analysis shows strong evidence in support of the Gamma-model representation of EM reconstructed data. FBP reconstructed data are adequately described by Gaussian distributions. On the basis of these results, we have described an approach for improved statistical analysis of PET data that has been reconstructed using practically used iterative (EM) methods. It involves a novel use of IRLS for implementation of a Gamma-based likelihood. Our experience with various data sets shows that the algorithm is always converged after a modest number of iterations. The approach also involves consideration of probability transformed residuals for diagnostic analysis. The approach is developed in the context of multiplication spatial-temporal models used in QA of PET scanners. The method is applied to estimate the bias and variance in QA data from a phantom study obtained from a PET scanner in routine clinical use.

#### 4.5.1 Theoretical Interpretation of MSE Characteristics

The simulation results presented describe the Gamma-model MSE characteristics for the class of multiplicative spatial-temporal models used in QA evaluation of

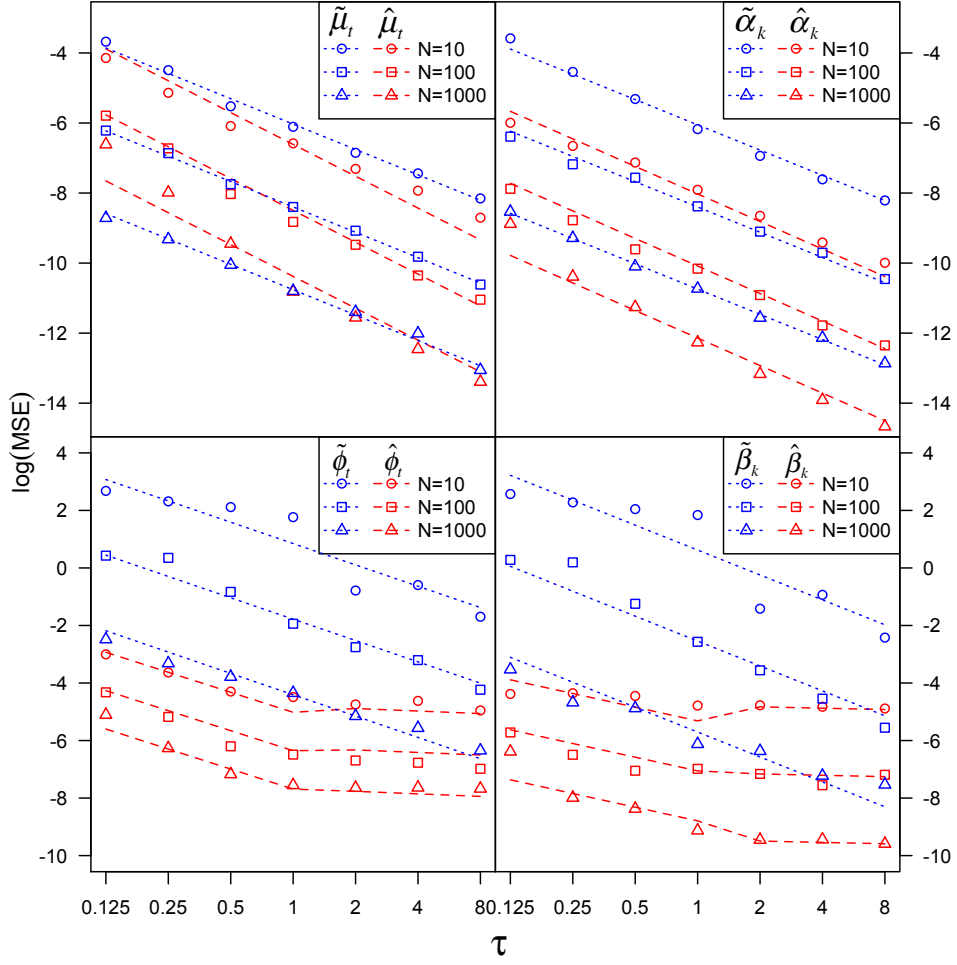


Figure 4.12: The log MSE of the parameter estimation evaluated as function of dose  $\tau$  and ROI size  $N$ . The log MSE for initial (LS) estimates are shown in blue and multiplicative model (ML) estimates are shown in red.

PET scanners. Potential benefits in efficiency are found by use of the Gamma-likelihood approach, when the data are Gamma in nature. A simplified analysis of this setup allows the measured empirical behaviour of the MSE as a function of dose and ROI size to be interpreted theoretically—see Figure 4.12. Consider  $\{z_1, z_2, \dots, z_N\}$  a random sample of size  $N$  from a  $\text{Gamma}(\tau\mu/\phi, \phi/\tau)$  distribution. For  $\tau$  large, the Gamma distribution is well approximated by a Gaussian with mean  $\mu$  and variance  $\mu\phi/\tau$ . In this limit, the maximum likelihood estimator (MLE) for  $\mu$  is the sample mean

$$\hat{\mu} = \frac{1}{N} \sum_{i=1}^N z_i.$$

The expected MSE of this (approximate ML) estimator is

$$E(\text{MSE}(\hat{\mu})) = \frac{\text{Var}(z_i)}{N} = \frac{\mu\phi}{N\tau}$$

Hence  $\log(\text{MSE}) \sim a_0 + a_1 \log(N) + a_2 \log(\tau)$  where  $a_1 = -1$  and  $a_2 = -1$ . This captures the empirical behaviour of the MSE of  $\mu$  and  $\alpha$  as a function of  $\tau$  and  $N$  found in the numerical simulations—see Table 5.1.

The analysis of the error characteristics in  $\phi$  and  $\beta$  in the QA multiplicative model can be examined by consideration of MLE for  $\phi$  in the simplified setup. Here analysis is made easier if we suppose  $\mu$  is known. If  $\mu$  is known, the (MLE) of  $\phi$  is

$$\hat{\phi} = \frac{1}{N} \sum_{i=1}^N \frac{(z_i - \mu)^2}{\mu/\tau}.$$

Using the approximate  $\chi_1^2$  distribution for  $[z_i - \mu]^2/(\mu\phi/\tau)$ —because  $z_i$  is approximately Gaussian—the expected MSE of  $\hat{\phi}$  is

$$E(\text{MSE}(\hat{\phi})) = \frac{\text{Var}([z_i - \mu]^2)}{\tau^2 \mu^2 N} \approx \frac{2\mu^2 \phi^2 / \tau^2}{\mu^2 N / \tau^2} = \frac{2\phi^2}{N}.$$

This analysis predicts that the asymptotic MSE of  $\hat{\phi}$  or  $\hat{\beta}$  will not diminish with increasing  $\tau$ , but it will reduce with increasing ROI size ( $N$ ). So  $\log(\text{MSE}) \sim a_0 + a_1 \log(N) + a_2 \log(\tau)$  where  $a_1 = -1$  and  $a_2 = 0$ . While Figure 4.12 does not agree with this analysis—there is an apparent non-linearity in the dependence of the  $\log(\text{MSE})$  as a function of dose ( $\tau$ ), the characteristic becomes remarkably flat for large dose. Table 4.2 presents estimated coefficients at large doses. These are in good agreement with the theoretical analysis.

### 4.5.2 Discriminating Between the Log-normal and Gamma Distributions

As well known, both the Log-normal and Gamma distributions may be used to describe skewed non-negative data. Kundu and Manglick [57] propose to discriminate between these two distributions using the ratio of the maximised likelihoods. Applying this procedure to our physical phantom data, we used likelihood to fit both the Log-normal and Gamma model to the cross-sectional voxel data for each combination of time frame  $t$  and slice  $k$  and then calculate the ratio of the maximised likelihoods for Gamma and Log-normal models. If the ratio is greater than 1, the Gamma model would be preferred, otherwise, the Log-normal model is preferred. For the non-Gaussian cross-sectional data (*c.f.* 4.4.1) there

are 79.77% of ratio values are greater than one, which means the Gamma model is generally found more appropriate than the Log-normal model in these data. Figure 4.13 (left) shows box-plots of the ratio distribution across the three levels of the time frames. At the early short duration time frames (less than 30 sec-

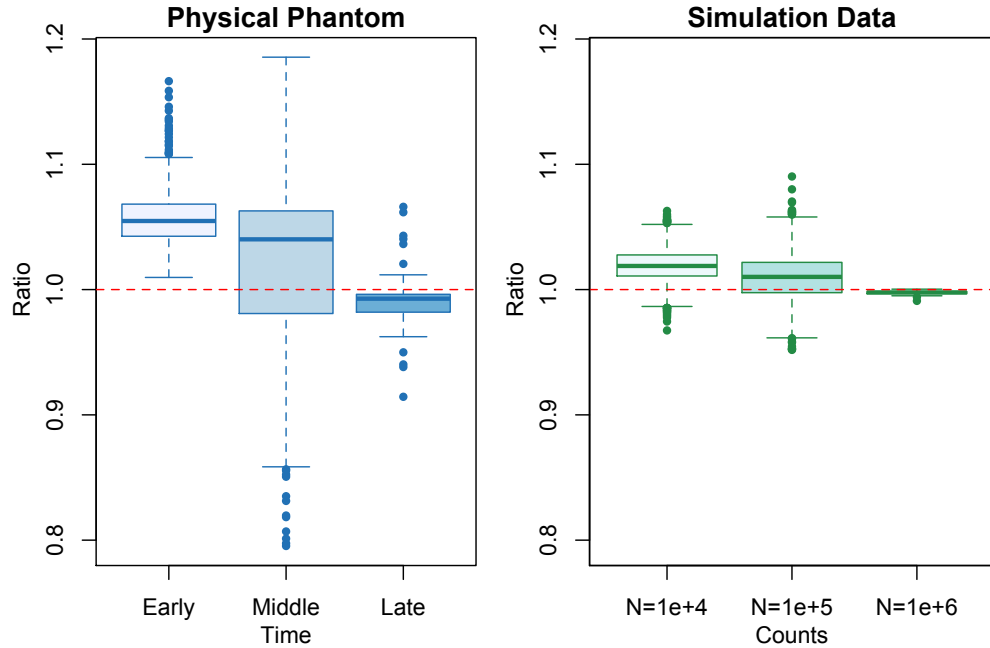


Figure 4.13: The likelihood ratio of Gamma model compare to Log-normal. Choose the Gamma distribution if the value is greater than 1, otherwise the Log-normal distribution is preferred.

onds), all the ratios are greater than 1, showing very strong evidence supporting the Gamma model over the Log-normal model. The evidence gets weaker with longer duration time-frames (between 30 and 1 minute) and diminished at the longest duration late time frames (more than 1 minute duration). In addition, the numerical simulation study, shown in Figure 4.13 (right), agrees with this result that the Gamma model is preferable at lower count. Barrett et al. [7] provided a theoretical argument indicating how the reconstructed data might be approximated by the Log-normal distribution. This was based on the assumption that the noise in the reconstructed images is relatively small—*i.e.* high-count settings. The analysis here indicates that especially in the shorter duration (lower count) time frames (the other end of the spectrum), the Gamma model is more plausible—Figure 4.13.

### 4.5.3 Generalisability to Other PET Scanners

We have evaluated a collection of 34 phantom data sets collected by the ACRIN on PET scanners that use positivity constrained reconstructions. These data sets are reconstructed using different iterative methods, such as RAMLA, OSEM and True-X. Our analysis, which is reported in 4.1.3, finds strong support for the Gamma distribution. In light of this we anticipate that there is potential to use the Gamma model to generally describe the behaviour positively constrained PET scanner data.

### 4.5.4 Implication of Gamma Model for Kinetic Modelling

Let  $z_t, t = 1, 2, \dots, T$  be the PET measured time-course data for an ROI. Often there is interest in evaluating parameters, say  $\theta$ , of a compartmental model based on such data. Suppose the time-course for the model is represented by the function  $c(t|\theta)$  for  $t = 1, \dots, T$ . Note that in this setting  $z_t$  and  $c(t|\theta)$  would usually have units of tracer activity—KBq per ml. The standard approach to estimation entails minimisation of a weighted least squares misfit between the data and the model

$$\text{WRSS}(\theta) = \sum_t w_t [z_t - c(t|\theta)]^2 \quad (4.6)$$

where  $w_t$  is an appropriate weighting function. This is statistically optimal when  $z_t$  is Gaussian with mean  $c(t|\theta)$  and variance proportional to  $w_t^{-1}$ . Often  $w_t$  is just taken to be a combination of frame-duration and decay correction, i.e.  $w_t = \Delta_t/f_t$  [63]. A more sophisticated iteratively re-weighted approach is to let  $w_t = w_t^0 = \Delta_t/(f_t c(t|\theta^0))$  where  $\theta^0$  is a current guess for  $\theta$  [35].

In the Gamma framework the model assumption is

$$z_t \sim \text{Gamma}(c(t|\theta)/(d_t\phi), d_t\phi)$$

where  $d_t^{-1} = \Delta_t/f_t$ . The likelihood based estimation process for multiplicative models is readily adapted to this case. With  $\phi$  fixed, from the expansion in (4.4), if  $\theta^0$  is a current guess for  $\theta$ , the updated value is obtain by minimisation of the weighted least squares function

$$\text{WRSS}(\theta|\theta^0) = \sum_t \tilde{w}_t [\tilde{y}_t - \frac{c(t|\theta)}{\phi d_t}]^2$$

where

$$\tilde{y}_t = \frac{c(t|\theta^0)}{\phi d_t} + \frac{\log(\frac{z_t}{\phi d_t}) - \psi(\frac{c(t|\theta^0)}{\phi d_t})}{\psi_1(\frac{c(t|\theta^0)}{\phi d_t})} ; \quad \tilde{w}_t = \psi_1(\frac{c(t|\theta^0)}{\phi d_t})$$

Thus a standard weighted non-linear least squares procedure can be used to implement the Gamma model analysis of the kinetic parameters. Note, if  $\theta^0$  is close to the true  $\theta$ , second order Taylor series expansion of the logarithm gives

$$\log(\frac{z_t}{\phi d_t}) \approx \log(\frac{c(t|\theta^0)}{\phi d_t}) + \frac{\frac{z_t}{\phi d_t} - \frac{c(t|\theta^0)}{\phi d_t}}{\frac{c(t|\theta^0)}{\phi d_t}} - \frac{(\frac{z_t}{\phi d_t} - \frac{c(t|\theta^0)}{\phi d_t})^2}{2(\frac{c(t|\theta^0)}{\phi d_t})^2}$$

If in addition the true activity  $c(t|\theta)$  is large (increasing dose), we have the following standard approximations for the di- and tri-gamma functions [3, 6].

$$\begin{aligned} \psi(\frac{c(t|\theta^0)}{\phi d_t}) &\approx \log(\frac{c(t|\theta^0)}{\phi d_t}) - \frac{1}{2}(\frac{c(t|\theta^0)}{\phi d_t})^{-1} \\ \psi_1(\frac{c(t|\theta^0)}{\phi d_t}) &\approx (\frac{c(t|\theta^0)}{\phi d_t})^{-1} \end{aligned} \quad (4.7)$$

Thus

$$\tilde{y}_t \approx \frac{z_t}{\phi d_t} - \frac{\epsilon_t}{\frac{c(t|\theta^0)}{\phi d_t}} ; \quad \tilde{w}_t \approx (\frac{c(t|\theta^0)}{\phi d_t})^{-1}$$

where  $\epsilon_t = \frac{(\frac{z_t}{\phi d_t} - \frac{c(t|\theta^0)}{\phi d_t})^2}{2\frac{c(t|\theta^0)}{\phi d_t}} - \frac{1}{2}$ . But, if  $\theta^0$  is the true,  $E(\epsilon_t) = 0$ . Hence the updating of  $\theta$  becomes independent of  $\phi$  and in fact reduces to the familiar iteratively re-weighted approach because our analysis shows

$$\text{WRSS}(\theta|\theta^0) \approx \frac{1}{\phi} \sum_t w_t^0 [z_t - c(t|\theta)]^2$$

where  $w_t^0 = d_t^{-1}/c(t|\theta^0)$ —c.f. (4.6).

A simple estimator of  $\phi$  is

$$\tilde{\phi} = \frac{1}{T} \sum_t \hat{w}_t [z_t - c(t|\hat{\theta})]^2$$

with  $\hat{w}_t = d_t^{-1}/c(t|\hat{\theta})$ . This estimate can be refined by a variation of the likelihood method for estimation of  $\phi$  in the multiplicative model. With  $\zeta = 1/\phi$ , the

iteration is:  $\zeta^1 = \zeta^0 - g(\zeta^0)/h(\zeta^0)$  where

$$\begin{aligned} g(\zeta) &= \sum_t \left\{ \frac{z_t}{d_t} - \frac{c(t|\theta)}{d_t} \log \left( \frac{z_t}{d_t} \zeta \right) \right. \\ &\quad \left. - \frac{c(t|\theta)}{d_t} + \frac{c(t|\theta)}{d_t} \psi \left( \frac{c(t|\theta)}{d_t} \zeta \right) \right\} \\ h(\zeta) &= \sum_t \frac{c(t|\theta)}{d_t} \left\{ \frac{c(t|\theta)}{d_t} \psi_1 \left( \frac{c(t|\theta)}{d_t} \zeta \right) - 1/\zeta \right\} \end{aligned}$$

Set  $\hat{\phi}$  to the converged value of  $\zeta$ . As in the multiplicative model, the estimation process alternates between updating  $\theta$  with  $\phi$  fixed, followed by updating  $\phi$  with  $\theta$  fixed. As an assessment of the standard approach—where  $\theta$  is estimated by iteratively re-weighted least squares, yielding  $\tilde{\theta}$ , and the simple estimator  $\tilde{\phi}$  is used for  $\phi$ —it is reasonable to compare the optimal the Gamma twice-log-likelihood with the twice-log-likelihood achieved using  $(\tilde{\theta}, \tilde{\phi})$ . Based on likelihood ratio theory, the deviations might be a concern if they exceeded the expectations for a  $\chi^2$  random variable with degrees of freedom equal to the dimension of  $(\theta, \phi)$  [87].

## 4.6 Concluding Remarks

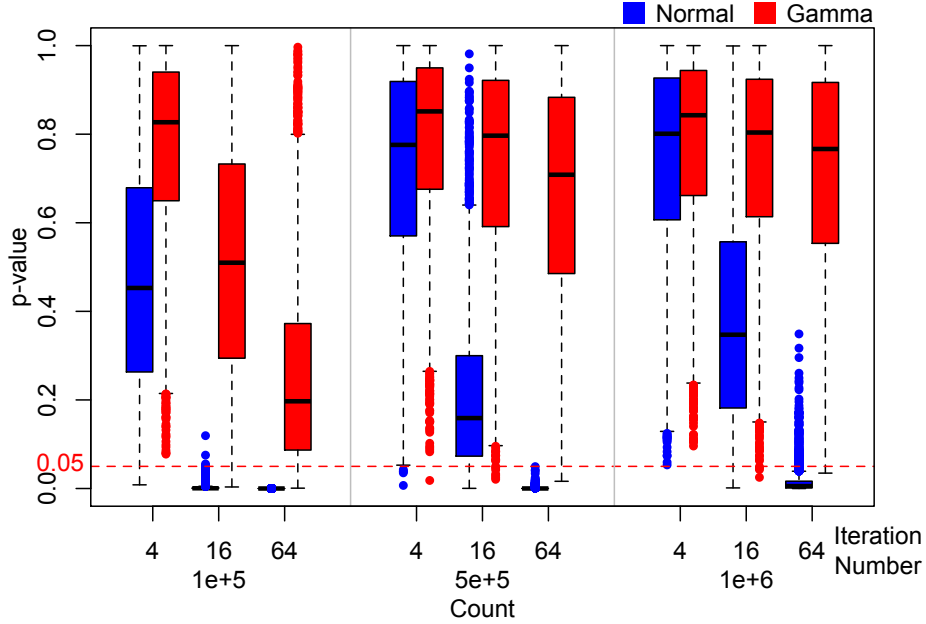


Figure 4.14: The Kolmogorov-Smirnov test p-values of Gamma and Normal model for numerical phantom simulation data with different iteration numbers (4, 16, 64) and counts (1e+5, 5e+5, 1e+6).



Overall the work shows that statistical adaptation to the Gamma-structure of iteratively reconstructed PET data is readily achieved. This has the potential to enhance the statistical efficiency of inferences obtained from such data. As shown in Figure 4.14, in our Numerical Phantom Study simulation setting the Gamma model is superior to Normal model especially at higher iteration numbers and lower counts. The data is more skewed as iteration number increases so that the Gamma model fit is better compared to Normal. The probability transformed Gamma residuals provide a very useful diagnostic in this context. Refinement of these techniques to provide a full treatment of the distribution of PET scanner data in 3-D, including the covariance patterns, is clearly of interest. The model above is a starting point for that development. Investigation of that approach will be reported in the next chapter.

# Chapter 5

## Spatial Auto-correlation and Simulation Analysis

### 5.1 Introduction

In many institutions, positron emission tomography (PET) imaging plays a key role in the routine clinical management of cancer patients, as well as with some important cardiac and neurologic conditions. With the growing reliance on PET imaging information for clinical decision making, there is an ongoing need to have more detailed quantitative understanding of the operational characteristics of reconstructed PET images. This can facilitate consistent clinical decision-making based on the PET at a given institution and may also enable the conduct of multi-institution clinical trials involving PET imaging biomarkers [98]. Going back to the 1980s [51] routine quality assurance (QA) is a well established part of nuclear medicine practice and in particular of PET. The standard approach to QA with PET is to image a known source—physical phantom scans—and use the results to assess bias and sensitivity patterns. Sensitivity plays a key role in understanding local variance characteristics. There is a significant literature on methods for assessment of the statistical variation of PET data. Most of this has focused on approximating standard errors for regional averages of reconstructed data using a combination of analytic and empirical formulae [2, 7, 19, 46, 50, 62, 85, 107, 118]. The potential use of bootstrap methodologies in this context is appealing but for iterative reconstructions the computation requirements of the approach has limited its use in an operational settings, especially for dynamic studies.

At the end of chapter 2, we mentioned some sources of noise correlations in PET image and indicated that the correlation between pixels has an significant effects on the image quality. Therefore, the examination of auto-correlations for

the normalised residuals of PET data is crucial to simulate the performance of PET scanner. In chapter 4, we presented a novel approach to the analysis of bias and sensitivity in a PET scanner based on QA data derived from a uniform source phantom [70]. Results showed that iteratively reconstructed PET image data were well described by Gamma statistics. Within the Gamma framework characterisation of bias and variance can be efficiently carried out in terms of a multiplicative model analysis [70]. As part of our study it was found that, through a standard probability transform which adjusts for bias and variance, raw reconstructed PET image data can be converted into a normalised Gaussian scale.

Building on these works, this chapter presents auto-regressive (AR) type models to represent 3-D spatial correlation structure of the normalised data. The goal of the present work is to extend the previous analysis in order to obtain a practical representation of the full noise characteristics of iteratively reconstructed PET data. We propose spatial autoregressive (SAR) models for representation of the 3-D spatial correlation structure of appropriately normalised data. The SAR approach involves relating the behaviour of each voxel to the behaviour on its neighbours. The first and second order neighbours are considered. Estimation of the SAR model cannot be accomplished by straightforward adaptation of the Yule-Walker process used for estimation of 1-D AR models [11]. Indeed such an approach can sometimes be inconsistent. We adapt a general methodology for SAR model estimation based on likelihood. The implementation makes use of the fast Fourier transform (FFT). The proposed approach leads to a consistent estimation process which provides a simple and practical approach for data analysis. Combining our previous work with this new development leads to a simplified approach to simulating PET images with noise characteristics that are matched to the operational scanner. Thus routine QA data can provide a mechanism for empirically representing the uncertainties in PET scan measurements.

In the following part of this section, we will briefly introduce the auto-correlation function (ACF) and demonstrate the inconsistency of least squares estimation for spatial auto-regressive model 5.1.2. In section 5.2, the basic theory and methodology are developed. Studies with physical and simulated data are described in section 5.3. Section 5.4 presents the results for both EM reconstructed data and simulated data.

### 5.1.1 Auto-correlation Function

In time series, auto-correlation is a measure of dependence between a series and a lagged copy of itself as a function of time lag. The auto-correlation [11] function (ACF) can be used to detect non-randomness in data and identify the processing model if the data is correlated. From the image analysis point of view, ACF is often used to evaluate the similarity between pixel values or, more specifically, between the pixel and nearby points.

Consider a set of 3-D PET image data  $z_{ijk}$  at a fixed time point. The relevant data structure is of the form  $\{z_{ijk}, i = 1, 2, \dots, I; j = 1, 2, \dots, J; k = 1, 2, \dots, K\}$  corresponding to a collection of  $I \times J$  phantom-voxels each recorded over  $K$  transverse slices. According to the analysis in the previous chapter, the data should follow the structure in which  $z_{ijk} \sim \text{Gamma}(\mu_k/\phi_k, \phi_k)$ , the mean is  $\mu_k$  and the variance is  $\mu_k\phi_k$ . Thus, the 1-D auto-correlation calculations on both transaxial and axial directions are as follows

$$\begin{aligned}\rho_i(l) &= \frac{1}{(I-l)JK\mu_k\phi_k} \sum_{\substack{i=1,\dots,I-l \\ j=1,\dots,J \\ k=1,\dots,K}} (z_{ijk} - \mu_k)(z_{i+l,j,k} - \mu_k) \\ \rho_j(m) &= \frac{1}{I(J-m)K\mu_k\phi_k} \sum_{\substack{i=1,\dots,I \\ j=1,\dots,J-m \\ k=1,\dots,K}} (z_{ijk} - \mu_k)(z_{i,j+m,k} - \mu_k) \\ \rho_k(n) &= \frac{1}{IJ(K-n)\mu_k\phi_k} \sum_{\substack{i=1,\dots,I \\ j=1,\dots,J \\ k=1,\dots,K-n}} (z_{ijk} - \mu_k)(z_{i,j,k+n} - \mu_{k+n})\end{aligned}$$

where  $l$  and  $m$  are the lags in transverse domain ( $x$ - and  $y$ -direction),  $n$  is the lag on axial direction (distance between slices),  $\mu_k$  and  $\phi_k$  are the estimated parameters of the Gamma model. The result of estimated 1-D and 3-D autocorrelation as a function of transaxial and axial distance is shown on Figure 5.1. The auto-correlation patterns in both transaxial and axial directions are significant. There is little difference of auto-correlation between  $x$ - and  $y$ -direction within one plane.

In following sections, 3-D auto-correlation is used to investigate how surrounding pixels affect the central pixel in both transaxial and axial directions. We consider an efficient computation follows the Wiener-Khinchin theorem [11, 104] which allows us to compute the spatial autocorrelation with two Fast Fourier

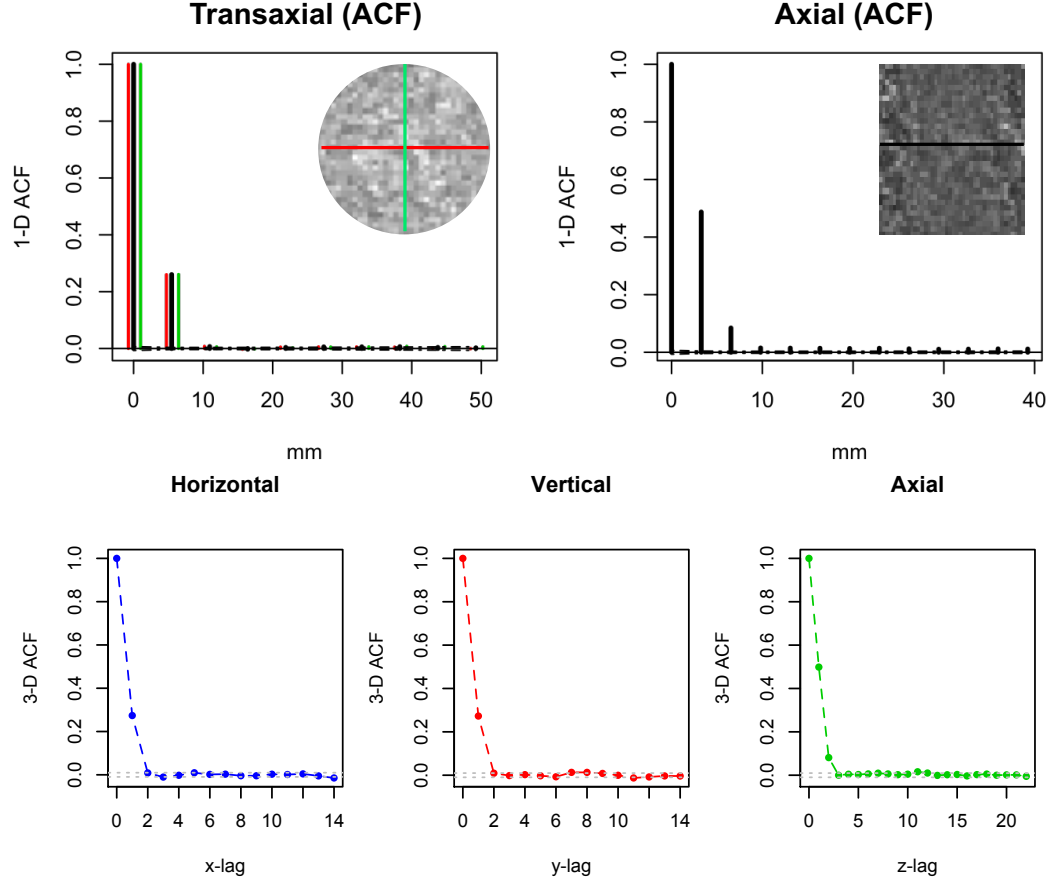


Figure 5.1: Top: Estimated transverse and axial auto-correlation functions (1-D ACF) for iterative reconstructed phantom data. The red and green lines in the transverse plot represent auto-correlation in row and column directions, respectively. Bottom: 3-D ACF for the same phantom. 1-D profiles through the centre of the phantom, showing from left to right, horizontal, vertical, and axial profile.

transforms (FFT)

$$\begin{aligned} S_{ijk} &= |\text{FFT}(u_{ijk})|^2 \\ R(l, m, n) &= \text{IFFT}(S_{ijk}) \end{aligned} \quad (5.1)$$

where IFFT denotes the inverse Fast Fourier transform,  $S_{ijk}$  is the power spectrum of  $u_{ijk}$ ,  $R(l, m, n)$  is the autocorrelation function  $\{l = 1, 2, \dots, L \ni I; m = 1, 2, \dots, M \ni J; n = 1, 2, \dots, N \ni K; \}$ .

### 5.1.2 Inconsistency of Least Squares Estimation for Spatial Autoregressive Model

In signal processing, the autoregressive (AR) model is often used to represent the random process that each variable is correlated with its own previous values. For example, the AR(2) model is defined as

$$X_t = \phi_1 X_{t-1} + \phi_2 X_{t-2} + \epsilon_t, \quad \epsilon_t \sim N(0, \sigma^2).$$

However, 3-D PET image data often shows spatial autocorrelations—as shown in Figure 5.1—which means that each voxel is correlated with its surrounding values and the conventional AR model is not applicable. Therefore, spatial autoregressive model (SAR) is more reasonable to describe the spatial autocorrelation pattern and to generate uncorrelated residuals. A simple 1-D SAR model and the parameter estimation of this model will be introduced shortly. Furthermore, the elaborate 3-D spatial autoregressive model for the physical PET phantom data will be discussed in section 5.2.

Consider a simple 1-D SAR model in time

$$y_t = \theta_1(y_{t-1} + y_{t+1}) + \theta_2(y_{t-2} + y_{t+2}) + \epsilon_t \quad (5.2)$$

for  $t = 0, \pm 1, \pm 2, \dots, T$  and  $\epsilon_t \stackrel{iid}{\sim} N(0, \sigma^2)$  white noise. Rewrite equation (5.2) as  $-\theta_2 y_{t-2} - \theta_1 y_{t-1} + y_t - \theta_1 y_{t+1} - \theta_2 y_{t+2} = \epsilon_t$  and let  $\Theta = (-\theta_2, -\theta_1, 1, -\theta_1, -\theta_2)$ , then the model could be rewritten as  $(\Theta * Y)_t = \epsilon_t$ . The data simulation procedure is as follows:

1. Generate an *iid* sequence  $\{\epsilon_t\}$ .
2. Generate  $\{Y_t\}$  by the inverse Fourier Transform (FT) of:  $\text{FT}(\{\epsilon_t\})/\text{FT}(\Theta)$ .

The simulated time series based on the above 1-D SAR model with  $\theta_1 = 0.3$ ,  $\theta_2 = 0.02$  is showed in the top row of Figure 5.2.

**Ordinary Least Squares (OLS) Estimation:** While the method of least squares is a standard (and asymptotically optimal) approach for estimation of familiar AR model coefficients [11, 15], it runs into problems for more general autoregressions. This was highlighted by Whittle [121]. To illustrate this consider the SAR model equation (5.2), then the least squares estimates of  $\theta = (\theta_1, \theta_2)$  minimise

$$RSS(\theta|y(t), t \in \mathcal{N}/\mathcal{N}_0) = \sum_{t \in \mathcal{N}_0} [\mathcal{P}_\theta y(t)]^2$$

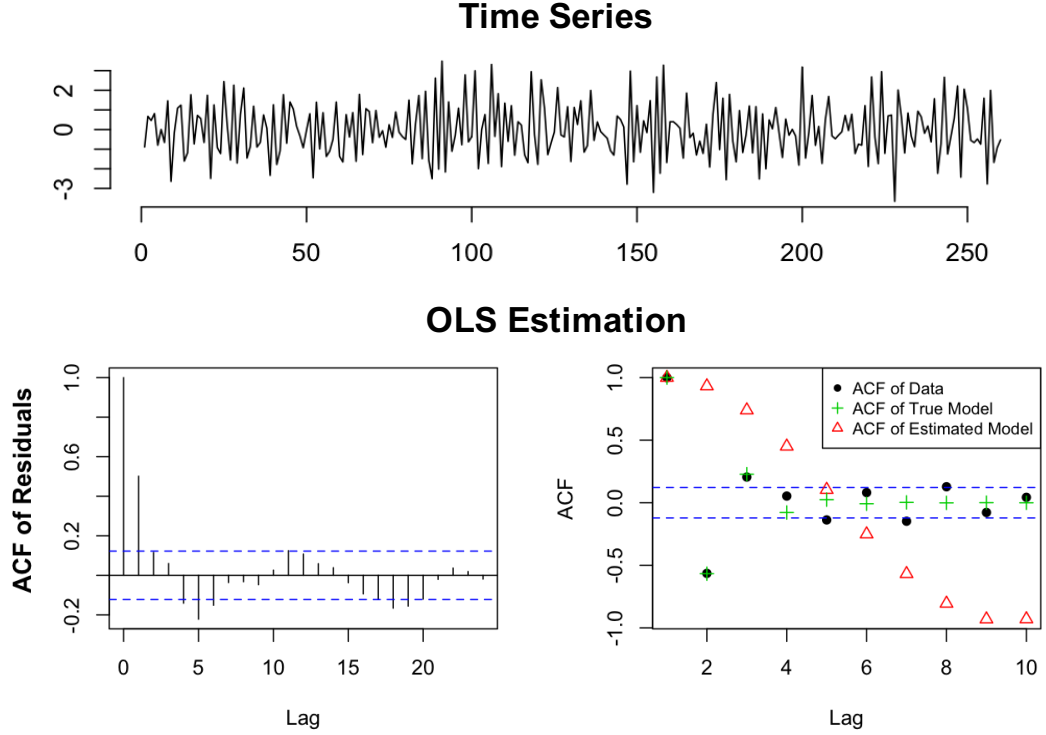


Figure 5.2: Top: Time series generated from the 1-D spatial AR(2) model. Bottom: Least squares auto-regression estimation results.

where  $\mathcal{P}_\theta = I - \theta_1(B + B^{-1}) - \theta_2(B^2 + B^{-2})$  with  $B$  is the backshift  $B^k y_t = y_{t-k}$  and  $\mathcal{N}_0 = \{0, \pm 1, \pm 2, \dots, T\}$  is the set of data indices and  $\mathcal{N}/\mathcal{N}_0 = \{-T-2, -T-1, T+1, T+2\}$  are the indices of unobserved  $y$ -values which are needed in order to reconstruct the innovations  $\epsilon(t)$  at the sampled points. For large  $T$ , the impact of unobserved data is negligible. Least squares coefficients satisfy the normal equations. In the present situation for large  $T$  these coefficients,  $\tilde{\theta}$ , are identified by

$$\begin{bmatrix} 1 + \rho_2 & \rho_1 + \rho_3 \\ \rho_1 + \rho_3 & 1 + \rho_4 \end{bmatrix} \begin{bmatrix} \tilde{\theta}_1 \\ \tilde{\theta}_2 \end{bmatrix} = \begin{bmatrix} \rho_1 \\ \rho_2 \end{bmatrix} \quad (5.3)$$

where  $\rho_l$  is the auto-correlation at lag  $l$  for  $l = 1, 2, 3, 4$ . It is not hard to find a situation where the estimates are inconsistent. For example, if  $\theta = (0.30, 0.02)$  then  $\tilde{\theta} = (-0.54, -0.15)$ . In light of this, least-squares auto-regression may not be relied on for estimation of SAR models parameters.

## 5.2 Methodological Development

The data structure arising from a physical phantom study is a set of reconstructed PET measurements  $\{z(n) = z(n_1, n_2, n_3), n = (n_1, n_2, n_3) \in \mathcal{N}_0\}$  corresponding

to a collection of  $N$  voxels consisting of  $I_1 \times I_2$  phantom-voxels recorded on each of  $I_3$  transverse slices in the field of view of the scanner. These data correspond to a particular acquisition time-frame during which the phantom is measured in the scanner field of view. In a dynamic PET study there will be multiple time-frames, but, as data from distinct time-frames can be considered to arise as a processed version of a thinned 4-D Poisson process, these can be considered as independent of each other. Our focus is on PET data that has been iteratively reconstructed using some variation on the EM algorithm [115].

### 5.2.1 Spatial Autoregressive Model

In previous work, we demonstrated that iteratively reconstructed PET data could be represented using the Gamma distribution [70]. So

$$z(n) = z(n_1, n_2, n_3) \sim \Gamma(\tau\mu(n)/\phi(n), \phi(n)/\tau)$$

where  $(n_1, n_2)$  are transverse plane co-ordinates and  $n_3$  indexes the slice.  $\mu(n)$  is the activity of the target source activity per unit mass (scaled by dose),  $\phi(n)$  models scanner and object-specific factors (most notably attenuation) that contribute to extra-Poisson variation,  $\tau$  is proportional to the injected dose per unit mass of the object. The Gamma model allows us normalise PET data to a Gaussian scale via the probability transform [70]:

$$u(n) = \Phi^{-1}(F(z(n)|\tau, \hat{\mu}(n), \hat{\phi}(n))) \quad (5.4)$$

where  $F(\cdot | \tau, \hat{\mu}(n), \hat{\phi}(n))$  is the Gamma distribution function with mean  $\hat{\mu}(n)$  and variance  $\hat{\mu}(n)\hat{\phi}(n)/\tau$ . Both  $\hat{\mu}(n)$  and  $\hat{\phi}(n)$  can be estimated from phantom data measurements [70].  $\Phi$  is the standard normal distribution function.

Here we propose to analyse the 3-D covariance of the normalised data using spatial autoregressive (SAR) models. A SAR model specifies a linear relation between a collection of appropriately defined neighbours

$$u(n) = \sum_k \theta_k u(n - k) + \epsilon(n) \quad (5.5)$$

where  $u(n) = u(n_1, n_2, n_3)$  and the summation is made over a set of negative and positive indices,  $k = (k_1, k_2, k_3)$ , such that voxels  $(n - k)$  belong to an appropriate neighbourhood of the voxel  $n$ —this will be detailed below.  $\epsilon(n)$  is a Gaussian white noise process with variance  $\sigma^2$ . By introducing a linear difference operator



$\mathcal{P}_\theta = \sum_k \theta_k B^k$  the model can be expressed as

$$\mathcal{P}_\theta u(n) = \epsilon(n) \quad (5.6)$$

where  $u(n)$  and  $\epsilon(n)$  represent the data and the innovation white noise process evaluated at the  $n$ 'th voxel and  $B^k u(n) = u(n - k) = u(n_1 - k_1, n_2 - k_2, n_3 - k_3)$ . In practice only a small number of  $\theta_k$  coefficients are non-zero. A first order model will only involve terms where all components of  $k$  are zero, except one being 1 in absolute value; an  $s$ 'th order model only has non-zero terms for  $k = (k_1, k_2, k_3)$ 's in which  $|k_1| + |k_2| + |k_3| \leq s$ . Models of order 2 seem adequate for us. SAR models are generalizations of simple auto-regressive (AR) models used in classical time series analysis [11, 15]. See Yao and Brockwell [126] for discussion of spatial generalizations of classical ARMA time series models. SARs have been proposed for analysis of spatial processes [36, 69, 94, 121], but to our knowledge, they have not been applied to nuclear medicine imaging data. The SAR models used in spatial statistics are sometimes specified so that the  $\theta$ -coefficients are known up to some scale factor determined from available data [34]. In our case we are interested in SAR models in which the full set of non-zero  $\theta$ -coefficients must be estimated from the available data.

### 5.2.2 Estimation of SAR Model Coefficients Using Likelihood-based Approach

Likelihood-based approaches to the estimation of SAR and ARMA models are well established and have the familiar behavior of regular maximum likelihood procedures [39, 69, 126]. In the case of an SAR it is well known, see *e.g.* Mohalp [69], that the appropriate (conditional) likelihood-based objective function can be expressed as

$$\begin{aligned} \ell(\theta|u(n), n \in \mathcal{N}/\mathcal{N}_0) &= \sum_{n \in \mathcal{N}_0} \frac{[\mathcal{P}_\theta u(n)]^2}{\sigma^2} + N \log(\sigma^2) \\ &+ \frac{N}{(2\pi)^3} \int_{[-\pi, \pi]^3} \log(\mathcal{P}_\theta(\lambda)^{-2}) d\lambda \end{aligned} \quad (5.7)$$

where  $N$  is the number of voxels in  $\mathcal{N}_0$ ,  $\lambda = (\lambda_1, \lambda_2, \lambda_3)$  and  $\frac{\sigma^2}{(2\pi)^3} |\mathcal{P}_\theta(\lambda)|^{-2}$  is the 3-d spectral density of the SAR process.  $\mathcal{P}_\theta(\lambda) = \sum_k \theta_k e^{i\lambda \cdot k}$ , with  $\lambda \cdot k = \lambda_1 k_1 + \lambda_2 k_2 + \lambda_3 k_3$ , is the 3-D discrete Fourier transform of the SAR coefficients. Differentiating equation (5.7) with respect to  $\theta$  and setting the derivative to zero

we obtain a pseudo-linear (score) equation for the unknown components of  $\theta$

$$\frac{1}{N} \sum_{n \in \mathcal{N}_0} [\mathcal{P}_\theta u(n)] u(n-l) = \int f_\theta(\lambda) |\mathcal{P}_\theta(\lambda)| e^{-i\lambda \cdot l} d\lambda \quad (5.8)$$

where  $l = (l_1, l_2, l_3) \in \mathcal{L}_\mathcal{P}$  indexes the relevant components of non-zero  $\theta$ 's. Under the assumption of symmetric SAR model,  $\mathcal{P}_\theta(\lambda)$  is positive, we have  $|\mathcal{P}_\theta(\lambda)| = \mathcal{P}_\theta(\lambda)$ . Then we have

$$\begin{aligned} \frac{1}{N} \sum_{n \in \mathcal{N}_0} [\mathcal{P}_\theta u(n)] u(n-l) &= \int f_\theta(\lambda) \mathcal{P}_\theta(\lambda) e^{-i\lambda \cdot l} d\lambda \\ \frac{1}{N} \sum_{n \in \mathcal{N}_0} [\sum_{l'} \theta_{l'} u(n-l')] u(n-l) &= \int f_\theta(\lambda) \sum_{l'} \theta_{l'} e^{-i\lambda \cdot (l'-l)} d\lambda \end{aligned}$$

Using Parseval's relation, the above equation can be expressed as a requirement that the maximum likelihood estimators ensure that select sample auto-covariances, at lags corresponding to the non-zero  $\theta$ , match the model-predicted covariances

$$\sum_{l' \in \mathcal{L}_\mathcal{P}} \hat{c}_N(l'-l) \hat{\theta}_{l'} = \sum_{l' \in \mathcal{L}_\mathcal{P}} c(l'-l|\theta) \hat{\theta}_{l'} \quad (5.9)$$

for  $l \in \mathcal{L}_\mathcal{P}$ . Here  $\hat{c}_N(l-l') = \frac{1}{N} \sum_{n \in \mathcal{N}_0} u(n-l) u(n-l')$  is a sample estimate of the auto-covariance and the inverse Fourier transform of the spectral density  $f_\theta(\lambda)$  gives the 3-D model auto-covariance,  $c(l-l'|\theta) = \int e^{-i\lambda \cdot (l-l')} f_\theta(\lambda) d\lambda$ . So that the problem is becoming to find the solution of equation (5.10)—score equation

$$\left( \sum_{l' \in \mathcal{L}_\mathcal{P}} \left( \hat{c}_N(l'-l) - c(l'-l|\theta) \right) \right) \theta_{l'} = 0 ; \quad \text{for } l \in \mathcal{L}_\mathcal{P} \quad (5.10)$$

by minimising the following objective function

$$\sum_{l \in \mathcal{L}_\mathcal{P}} \left[ \sum_{l' \in \mathcal{L}_\mathcal{P}} \left( \hat{c}_N(l'-l) - c(l'-l|\theta) \right) \theta_{l'} \right]^2$$

According to the Cauchy-Schwarz inequality [102], the above function is smaller than the following

$$K \sum_{l \in \mathcal{L}_\mathcal{P}} \sum_{l' \in \mathcal{L}_\mathcal{P}} \left( \hat{c}_N(l'-l) - c(l'-l|\theta) \right)^2 \theta_{l'}^2$$

Under the general assumption of  $|\theta_l| \leq 1$ , we can then further diminish the function as

$$K \sum_{l \in \mathcal{L}_\mathcal{P}} \sum_{l' \in \mathcal{L}_\mathcal{P}} \left( \hat{c}_N(l'-l) - c(l'-l|\theta) \right)^2$$

By setting  $w_m$  as the number of  $l' - l$  where  $m \in l' - l$ , the above function can be diminished by considering the sum of squared difference between the sample auto-covariances and the model-predicted covariances with weights  $w_m$  and respect to  $m \in l' - l$ .

$$K \sum_{m \in l' - l} w_m \left( \hat{c}_N(m) - c(m|\theta) \right)^2$$

Then a nonlinear least squares (NLS) approach is straightforward for estimating the parameter  $\theta$ .

### 5.2.3 Computational Considerations

The hyper-rectangular volume of the normalised data— $u(n)$  can be processed using the 3-D FFT to obtain the periodogram,  $f_N(\lambda)$ . The inverse FFT of the periodogram provides a set of sample auto-covariances  $c_N(l - l')$ . For a specified  $\theta$  we sample  $\frac{1}{(2\pi)^3} |\mathcal{P}_\theta(\lambda)|^{-2}$  at the same discrete Fourier frequencies as the periodogram and apply the inverse FFT, followed by normalisation to ensure  $c(0|\theta) = c_N(0)$ , this provides the model auto-covariances,  $c(l - l'|\theta)$ . These are used to evaluate (7). Note the auto-correlations of the data and the model are obtained as

$$\rho_N(k) = c_N(k)/c_N(0) \quad \text{and} \quad \rho(k|\theta) = c(k|\theta)/c(0|\theta).$$

### 5.2.4 Validation of the Likelihood-based Estimation Using 1-D Simulation

To validate our likelihood-based approach to the estimation of SAR model, we consider a 1-D simulation study which is comparable to the study in section 5.1.2. The simulation model is (5.2) with parameters  $\theta_1 = 0.4$  and  $\theta_2 = 0.05$  and then apply our estimation procedure described in 5.2.2 to estimate the parameters. As shown in Figure 5.3, the estimates are  $\hat{\theta}_1 = 0.398 \pm 0.01$  and  $\hat{\theta}_2 = 0.049 \pm 0.01$  and both of the objective function and the score equation are converged. Also, the ACF of estimated model is consistent with the true model. This result indicates that the estimated model by likelihood-based approach is able to cover the true ACF pattern and the consistency is guaranteed. In following sections, an elaborate simulation procedure in 3-D domain is developed for iterative reconstructed PET data.

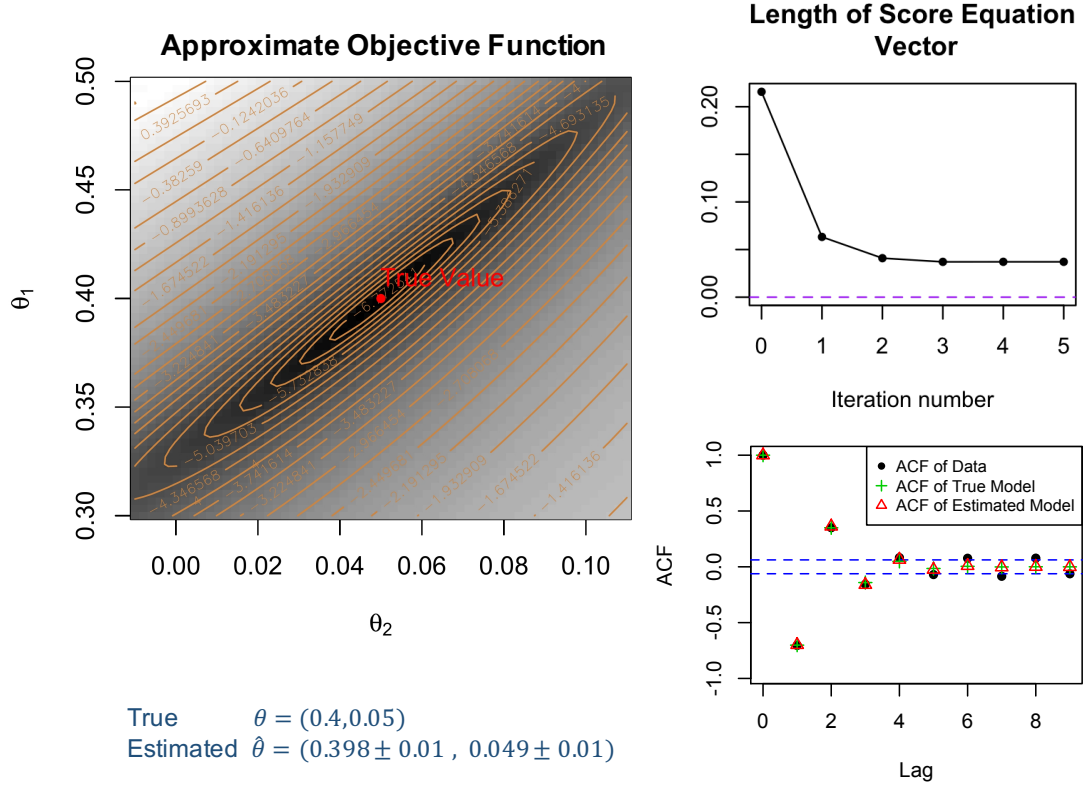


Figure 5.3: Results of likelihood-based estimation of 1-D simulation data.

### 5.2.5 Neighbourhood Structure

Model (5.5) is based on specification of the neighbourhood structure of each voxel. Image data has a regular structure and there are several intuitive strategies for defining the neighbourhood structure of a voxel [23]. We define the  $s$ 'th order neighbourhood of  $(i, j, k)$  as

$$N_s = \{(i', j', k'); 0 < |i - i'| + |j - j'| + |k - k'| \leq s\};$$

for  $s = 1, 2, \dots$

The first ( $s = 1$ ) and second ( $s = 2$ ) neighbourhood structures are sketched in Fig. 5.4. The first order neighbourhood is also known as the 3-D Rook neighbourhood [127].

### 5.2.6 Simulation of PET Data

The Cramer representation theorem, see *e.g.* Mohalp [69], provides a mechanism to simulate normalised PET data and by inverting the Gamma model probability transform in equation (1), these data can be converted into simulated PET image

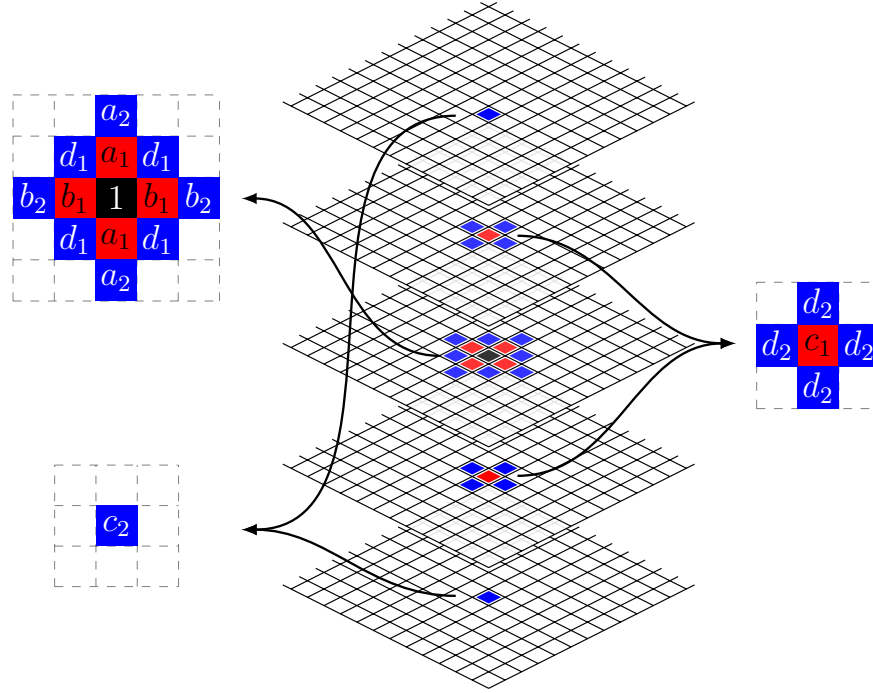


Figure 5.4: Diagram of first (red) and second (blue) order neighbours for a selected voxel (black) with a set of coefficients for each neighbour.

values for  $z(n)$ . The process is as follows: First generate  $\epsilon(n)$  as an *iid*  $N(0, \sigma^2)$  process; transform  $\epsilon(n)$  using the FFT and scale by the  $\mathcal{P}_\theta(\lambda)$ . Next apply the inverse Fourier transform (FFT) to generate the normalised data  $u(n)$ . These steps are summarised by the formula.

$$u(n) = \mathcal{F}^{-1}\left[\frac{\mathcal{F}[\epsilon](\lambda)}{\mathcal{P}_\theta(\lambda)}\right][n]$$

where  $\mathcal{F}$  represents the FFT. Finally simulated PET values are obtained as

$$z(n) = F^{-1}\left(\Phi(u(n))|\tau, \mu(n), \phi(n)\right)$$

The analysis method and simulation step is summarised graphically in Fig. 5.5.

## 5.3 Experimental Methods

### 5.3.1 Normalised Physical Phantom Data Analysis

Quality assurance refers to a procedure to ensure that delivered products match to the requirements. In particular, monitoring the performance of installed scanner

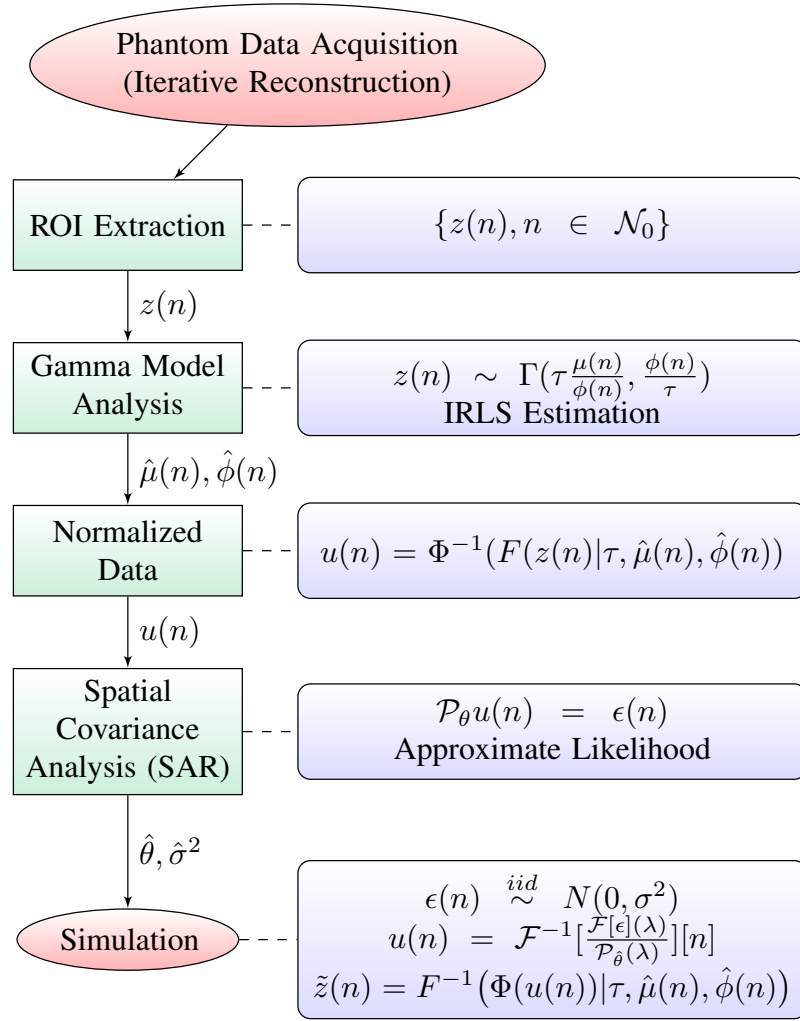


Figure 5.5: Graphical representation of the PET analysis and simulation process

can be implemented by a range of routine phantom tests matched to operational clinical practice. We consider the data of this type collected at a PET imaging facility at a local hospital—the Cork University Hospital (CUH). The scanner is a GE Discovery VCT PET/CT and used clinically for imaging of cancer patients. In our study, the scanning procedure was in line with a standard dynamic PET-FDG brain imaging protocol developed by the American College of Radiology Imaging Network (ACRIN) [98]. The cylindrical phantom is 189 mm in length and 195 mm in diameter, filled with a mixed solution of F-18 radiotracer and water and placed centrally in the field of view (FOV). Routine clinical image reconstruction is performed with 3-D iterative EM reconstruction (3D-IR). A dynamic sequence of 45 time-frames is acquired for 55 minutes. For each time-frame, the reconstructed image has  $128 \times 128$  pixels in 47 slices, with pixel size of  $5.46875 \times 5.46875 \text{ mm}^2$  and slice thickness of 3.27 mm. Region of interest (ROI)

data for the interior cross-sectional circular volume of the phantom, acquired for each axial slice (except two extreme slices),  $k$ , and for each time-frame,  $t$ , are available for analysis. The data for the set of all  $K$  slices and  $T$  time-frames structured as  $\{z_{ikt}, i = 1, 2, \dots, N, k = 1, 2, \dots, K, t = 1, 2, \dots, T\}$ . The analysis here focuses on data from a single time-frame—the  $t = 24$  frame.

In previous study [70], these measurements have been normalised based on the multiplicative Gamma model and the normalised data can be well described by the Gaussian distribution (*c.f.* Fig. 5.6). Based on the analysis of 3-D auto-correlation of the phantom data (Figure 5.7), there is little rotational variation in row and column directions within each slice. Hence we consider all voxels within the ROI where both 1- and 2-order neighbours are available. Reasonably assuming that the data on each direction (row, column and axial) are symmetric, we denote the regression coefficients as shown in Figure 5.4. We apply the methodology developed in the previous section to fit to SAR models to the normalised data. The order of neighbourhood,  $s$ , is selected based on the significance of regression coefficients and diagnostic analysis of residuals—primarily the residual auto-correlation characteristic [11].

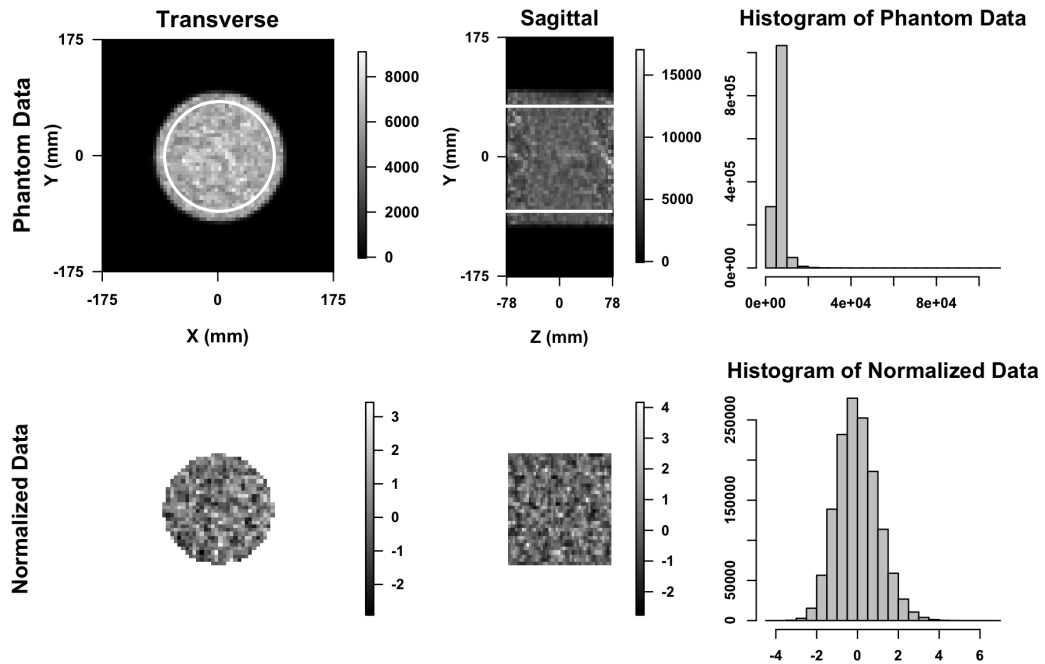


Figure 5.6: Top: The transverse and sagittal image of 3-D dynamic PET study on a cylindrical phantom using iterative (3D-IR) reconstructed methods (24th time frame of slice 23). The ROI data within white outline are used in analysis. On the right is the histogram of the data generated from ROIs. Bottom: Images and histogram of the probability transformed/normalised data generated by the previous study.

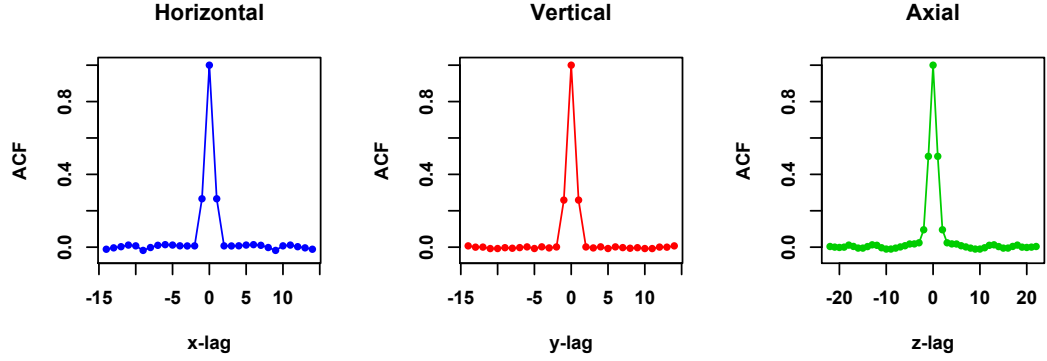


Figure 5.7: 3-D ACF of the ROI data shown in the top of Fig. 5.6

### 5.3.2 SAR Model Simulation

To illustrate the performance of the proposed method in estimating SAR model coefficients, we simulate 3-D data according to the following model

$$u(n) = \sum_k \theta_k u(n - k) + \epsilon(n),$$

for  $n \in \mathcal{N}_0$  and  $\theta_k$  matched to typical values estimated from the CUH phantom. Mean square errors (MSE) for the  $\theta$  parameter estimation, defined as  $\frac{1}{N_\theta} \sum_k (\theta_k - \hat{\theta}_k)^2$  where  $N_\theta$  is the number of the  $\theta$  parameters, are evaluated as function of ROI size for the noise level matched to the one in the CUH Phantom data.

### 5.3.3 Numerical Phantom Simulation

The 2-D VSK phantom [115] and the same size uniform elliptical phantom, shown in Fig. 5.11 and 5.12, were used. A sinogram source  $g$  was evaluated using a simple analytic Radon projection. The both sinograms generated from the VSK and uniform phantom were attenuated using the same attenuation matrix that assumed uniform density in the phantom region. Poisson data in the sinogram domain were simulated in R using the function `rpois`. Reconstructions with count rates of  $10^5$  and  $10^6$  were considered. Data were reconstructed using the Expectation-Maximization (EM) algorithm. The EM algorithm, initialised with the true uniform image, is stopped after iterated 16 times. No post-reconstruction smoothing was performed. For each count rate, 1000 replicates were evaluated. The distribution of data over replicates were used to estimate Gamma model parameters and probability transform normalisation [70]. Methods developed in Section 5.2 were then used to analyse the 2-D autocorrelation of the normalised



VSK and uniform phantom data respectively.

## 5.4 Results

We begin by presenting results of the analysis of physical phantom data, this is followed by numerical simulation studies including SAR model simulation and VSK phantom simulation.

### 5.4.1 Physical Phantom Data

Figure 5.8 shows uniform cylindrical phantom data OSEM reconstructed at a PET imaging facility at a local hospital before (the top) and after (the bottom) normalising based on the Gamma distribution [70]. Histogram at the bottom right indicates that the normalised data can be modelled using the Gaussian distribution. We fit a SAR model with the second order neighbourhood to the normalised data. The 3-D ACF of the fitted model is plotted as three 1-D profiles in Figure 5.8, in comparison with 3-D ACF of the normalised data. Also shown in Figure 5.8 is the 3-D ACF of SAR model residuals. The 3-D ACF of the normalised data is well described by the model. The model residuals show no significant autocorrelation present in transaxial directions, but some significant autocorrelation present in axial direction. However, the amplitude of autocorrelation is greatly reduced (in comparison to the normalised data). This may indicate that there is non-stationary axial autocorrelation present in the data not accounted for by the 3D SAR model. The estimated model coefficients are presented in Table 5.1.

Table 5.1: Non-linear Regression Coefficients

$\hat{a}_1$	$0.151 \pm 0.005^*$	$\hat{a}_2$	$-0.015 \pm 0.002^*$
$\hat{b}_1$	$0.149 \pm 0.005^*$	$\hat{b}_2$	$-0.014 \pm 0.002^*$
$\hat{c}_1$	$0.275 \pm 0.006^*$	$\hat{c}_2$	$-0.040 \pm 0.003^*$
$\hat{d}_1$	$-0.018 \pm 0.003^*$	$\hat{d}_2$	$-0.037 \pm 0.003^*$

\* denotes significant.

### 5.4.2 SAR Model Simulation

Using the  $\theta$  parameters estimated from and the same data size as the CUH ROI data for one time frame ( $N_0 = 30 \times 30 \times 45$ ), Fig. 5.9 shows that the ACF structure in the CUH ROI data can be well captured and simulated by the simulation model. The R-squared values of the estimated ACFs based on the CUH ROI data and

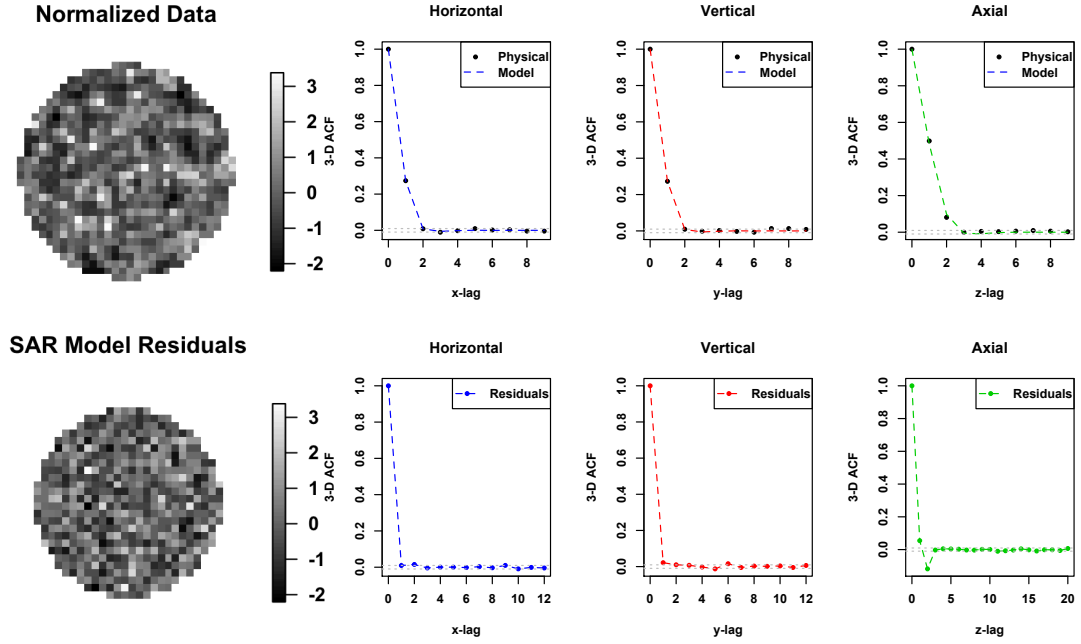


Figure 5.8: Top: Comparison between the ACF of reconstructed PET phantom data and the modelled ACF. Bottom: 3-D ACF patterns of SAR model residuals.

simulated data are 99.86%, 99.51% and 99.56% in the horizontal, vertical and axial direction, respectively. At lag 1 the relative differences between these ACFs are 2.38%, 7.41% and 4.33%, respectively.

To demonstrate estimation accuracy of the proposed method, data with varying size were generated. The considered data sizes are created by scaling each dimension of the CUH ROI using the same scale factor  $\tau$ , that is  $\tau N_0$  for  $\tau = 0.5, 1, 2, 4, \dots, 64$ . Then the proposed method was applied to the simulated data. This process is repeated 20 times for each data size. Fig. 5.10 shows the log mean square error (MSE) of the  $\theta$  estimation, defined as  $\frac{\sum_k (\theta_k - \hat{\theta}_k)^2}{\text{number of } \theta'_s}$ , as function of the log sample size  $\tau N_0$ . This figure seems to indicate that log MSE decreases linearly in the log sample size, especially after ignoring the first box. The slope-coefficient is estimated as  $(-1.04 \pm 0.06)$ , consistent with asymptotic theory.

### 5.4.3 Numerical Phantom Simulation

The top left of Fig. 5.11 and 5.12 shows the image of the VSK and uniform phantom used in the simulation study, respective. The top right shows the EM reconstruction of the VSK and uniform phantom after 16 iterations. The 2-D ACF of the normalised VSK and uniform phantom reconstruction as well as the 2-D ACF of the fitted SAR model residuals are also shown in Fig. 5.11 and

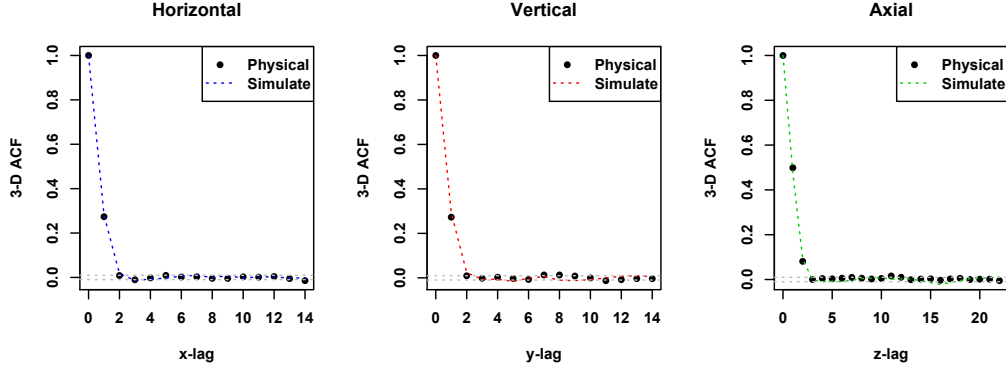


Figure 5.9: Comparison of the 3-D ACF between the physical phantom data and the model simulated data on each direction.

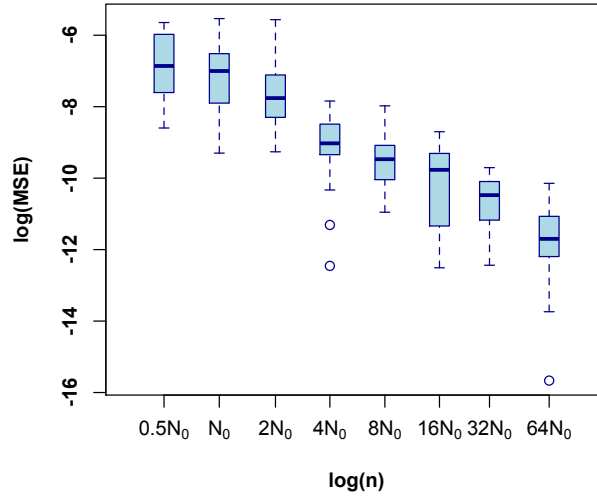


Figure 5.10: Log mean squared errors (MSE) of the estimated parameters based on simulation study with different sample sizes (20 repetitions for each size).  $N_0$  corresponds to the size of the phantom ROI in the CUH data.

5.12. The very similar 2-D autocorrelation patterns of the normalised VSK and uniform phantom reconstruction can be seen in the middle row of 5.11 and 5.12, and the both patterns can be captured by the SAR model (the bottom row of 5.11 and 5.12). To make more reliable comparison between uniform and non-uniform sources, 1000 replicates were generated. Fig. 5.13 shows the images of average  $\mu(n)$  and  $\phi(n)$  for uniform (top row) and VSK phantom (bottom row) based on 1000 replicates. Fig. 5.14 shows the estimated SAR model parameters of the normalised VSK and uniform phantom reconstruction based on 1000 replicates. It is apparent that the estimated parameters are very similar between VSK and uniform phantom reconstructions.

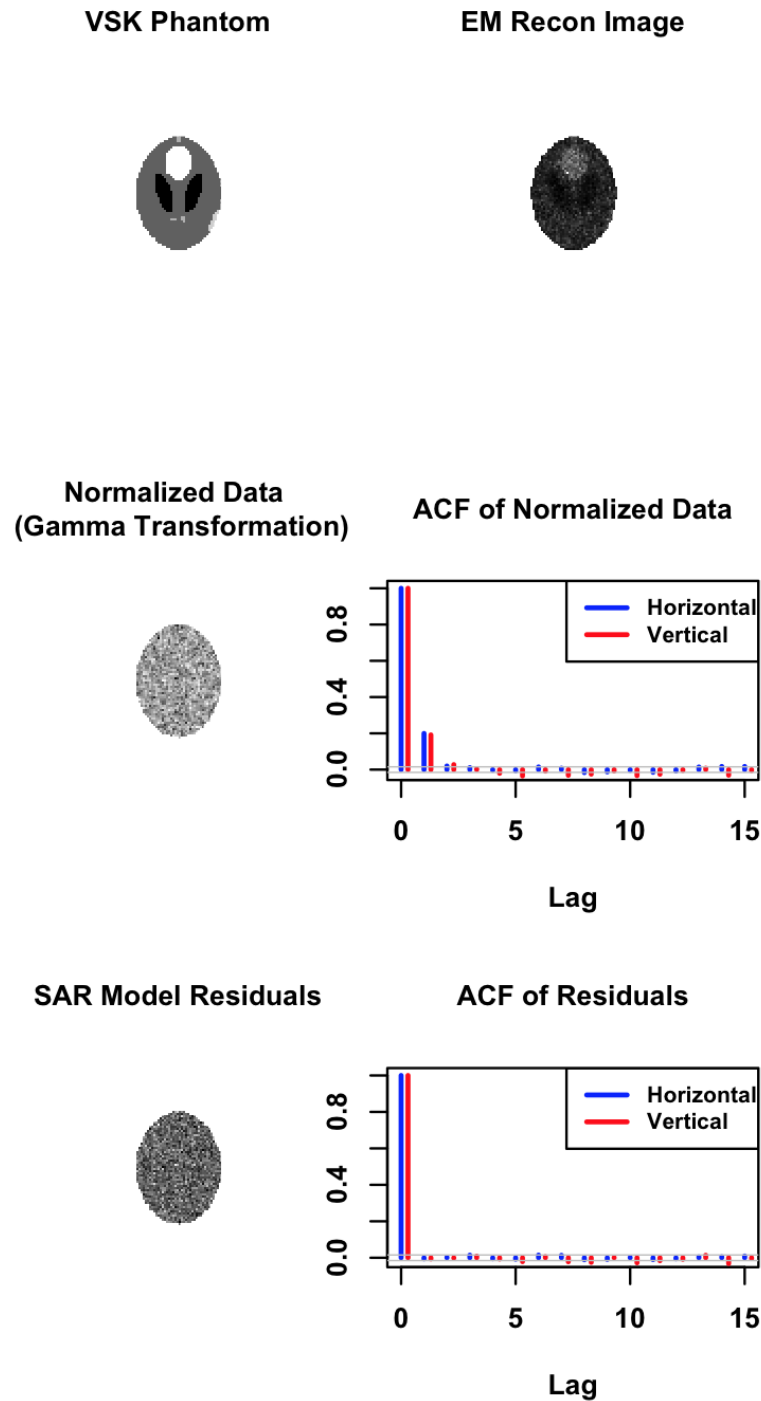


Figure 5.11: Images of the VSK phantom and EM reconstructed VSK phantom (top row). Image and one dimensional profiles of 2-D ACF of the normalised EM reconstructed VSK phantom (middle row). Image and one dimensional profiles of 2-D ACF of the fitted SAR model residuals (bottom row). The 2-D ACF were assessed for each replicate. Shown is the averaged ACF over 20 replicates.

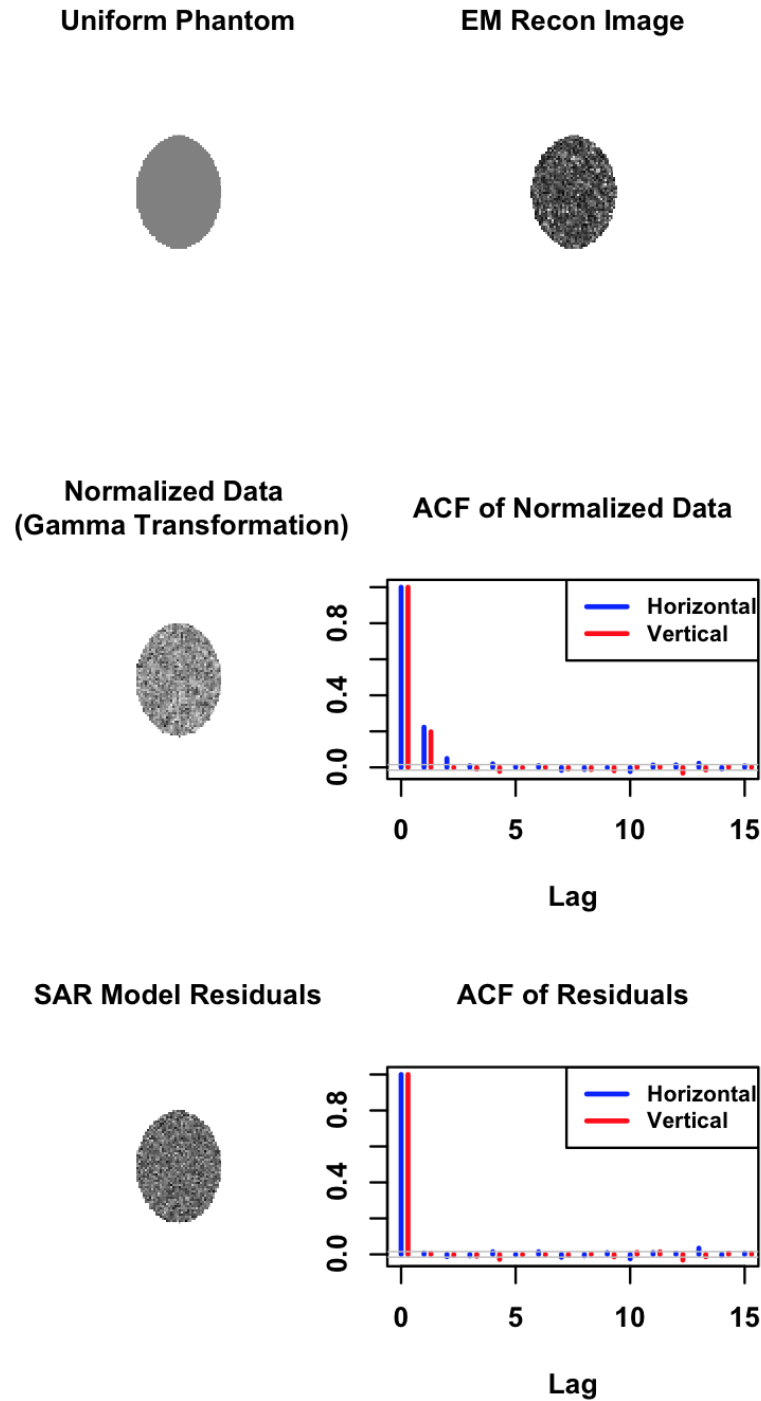


Figure 5.12: Images of the uniform phantom and EM reconstructed uniform phantom (top row). Image and one dimensional profiles of 2-D ACF of the normalised reconstructed uniform phantom (middle row). Image and one dimensional profiles of the fitted SAR model residuals. The 2-D ACF were assessed for each replicate. Shown is the averaged ACF over 20 replicates.

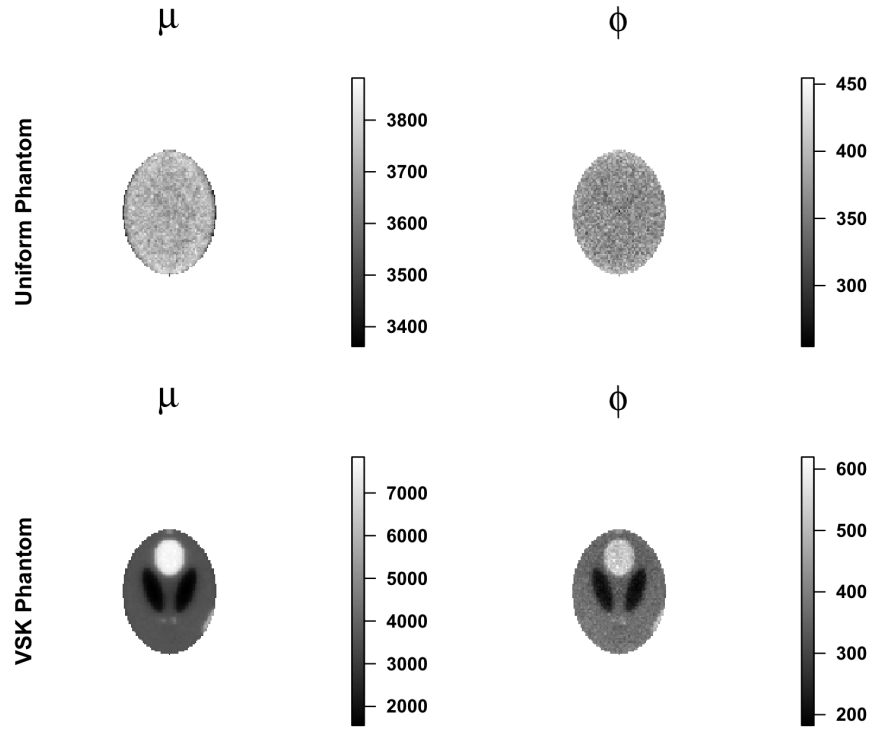


Figure 5.13: Images of average  $\mu(n)$  and  $\phi(n)$  based on 1,000 simulation studies involving the VSK and uniform phantom.

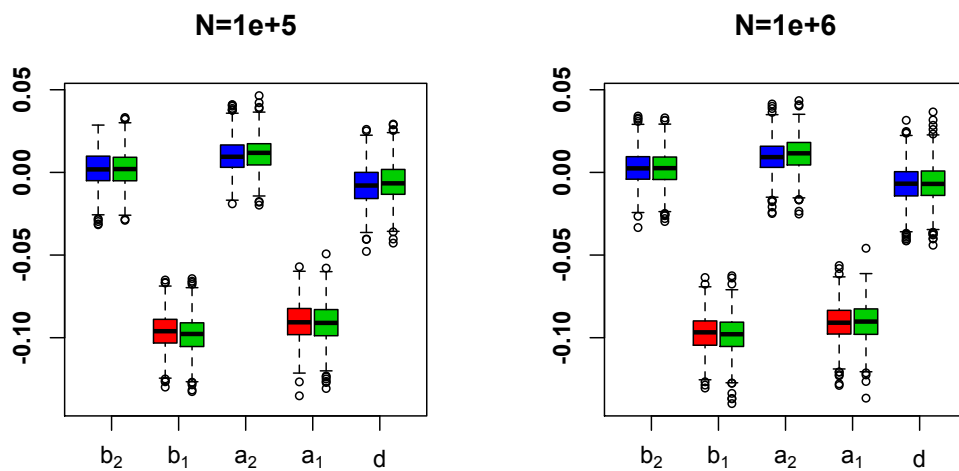


Figure 5.14: Estimated the SAR model parameters of the normalised EM reconstructed VSK phantom (blue and red) and uniform phantom (green) based on 1,000 simulation studies involving different count levels.

#### 5.4.4 Impact of Spatial Covariance

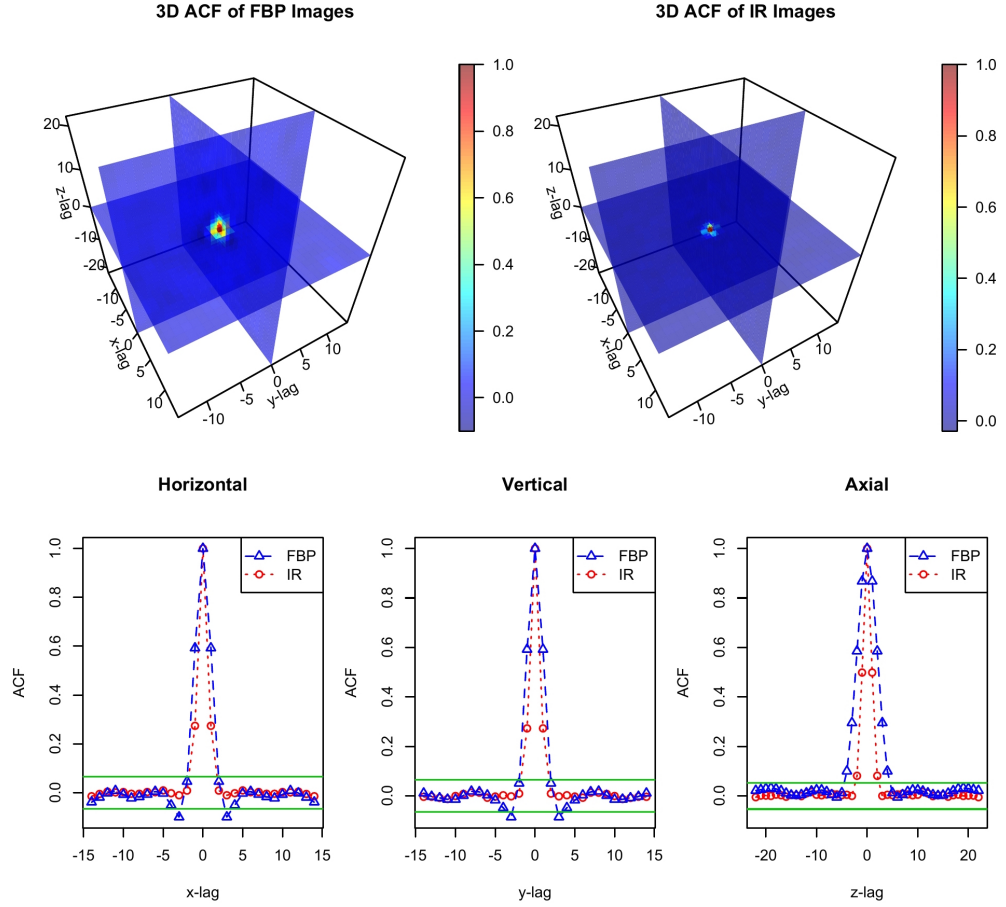


Figure 5.15: Top: 3-D ACF of FBP and IR physical phantom. Bottom: One dimensional profiles of 3-D ACF of FBP and IR reconstruction physical phantom images through the centre of the phantom, showing from left to right, horizontal, vertical and axial profile.

In this section, we will discuss the impact of spatial covariance by some simulation studies. In practice the covariance characteristics of reconstructed PET images is clearly important. The MSE behaviour of the Gamma-based estimation technique relative to LS could well be impacted by covariance in the ROI data. To investigate this, we adapted our simulation study to take account of the type of covariance seen in the physical phantom data. The auto-covariance used was matched to our physical phantom data by considering a hyper-rectangular volume placed inside the physical phantom (4.3.1) and extracting the normalised Gamma-transformed residuals  $\{r_{ijk}, i = 1, 2, \dots, I; j = 1, 2, \dots, J; k = 1, 2, \dots, K\}$ .

Following the Wiener-Khinchine theorem [11], the 3-D autocorrelation function (ACF) was estimated as the inverse FFT of the 3-D power spectrum of hyper-rectangular volume data. Very similar 3-D autocorrelation patterns are

observed across time frames (not shown). This is expected since time-frames are independent and the resolution filter bandwidth is not varied with frame duration. We averaged the ACF's across time-frames to produce a final 3-D ACF function. One dimensional ACF profiles through the centre of the hyper-rectangular volume are shown in Figure 5.15. Horizontal profiles (left) look almost same as the vertical ones (middle), indicating isotropic correlation behaviour within each slice for both FBP and EM images. There is stronger correlation in the FBP images compared to the EM images. This is no doubt due to the different mechanisms affecting the smoothness of the two data sets—the correlation is affected by the filter cut-off frequency for the FBP images [122] and, in addition, by the iteration number for the EM images [124].

We note that the simulation method in 5.2.6 generates correlated data. To investigate the effects of correlation on estimation accuracy of  $\mu_{kt}$  and  $\phi_{kt}$ , we use the simulation method in 5.2.6 to simulate the PET images with 3-D auto-correlation matched to the one observed in the EM data for each time frame and slice.

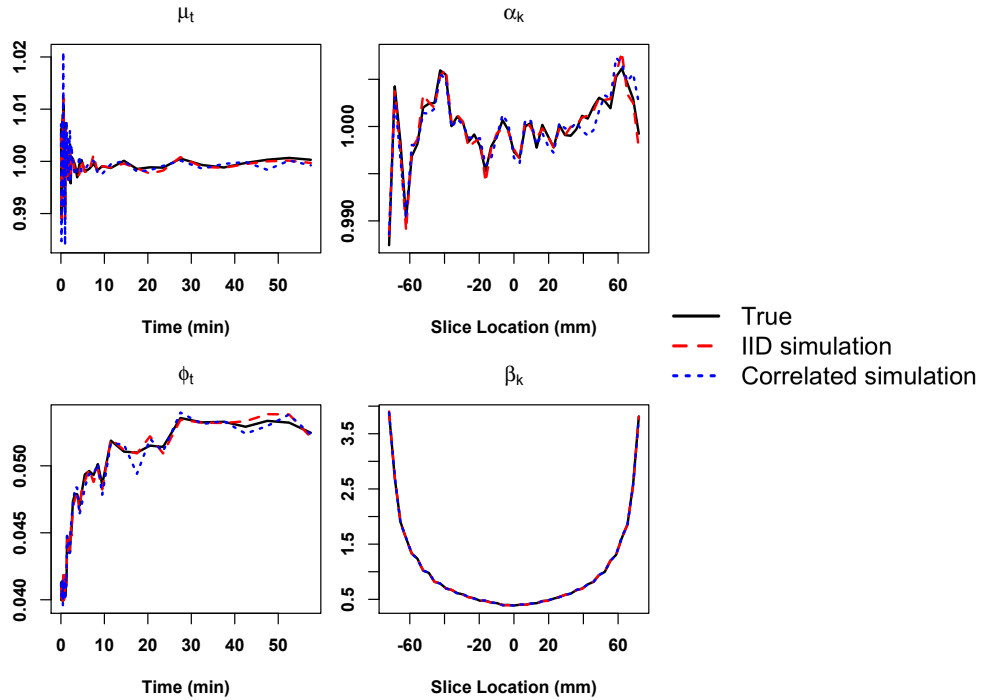


Figure 5.16: Parameter estimation for *i.i.d.* simulation versus correlated simulation.

Figure 5.16 shows comparison of  $\mu_t$ ,  $\alpha_k$ ,  $\phi_t$  and  $\beta_k$  estimation based on simulated data with (blue) and without (red) 3-D autocorrelation structure. Although less accurate, estimates based on the auto-correlated data follow the true values



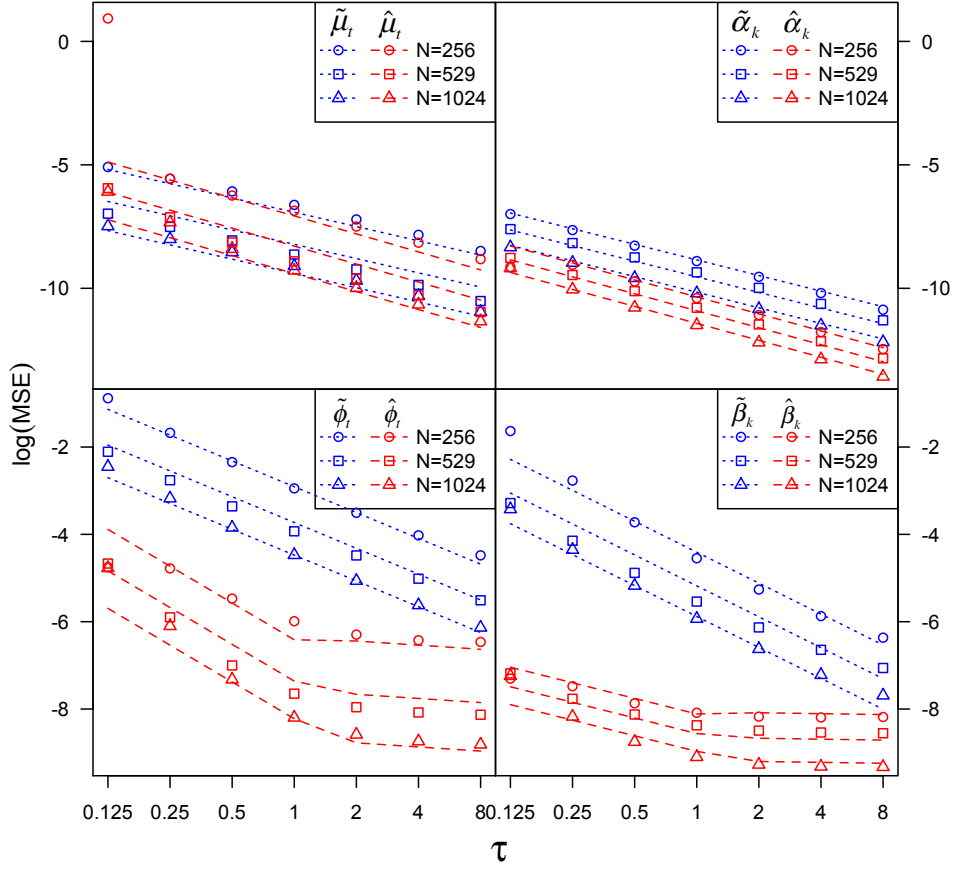


Figure 5.17: The log MSE of the parameter estimation for auto-correlated data evaluated as a function of dose  $\tau$  and ROI size  $N$ . The log MSE for initial (LS) estimates are shown in blue and multiplicative model (ML) estimates are shown in red.

well. The log MSE of the two estimations evaluated as a function of dose  $\tau$  and ROI size  $N$  are presented in Fig. 5.17.  $N = I \times J$ . The regression model of MSE is  $\log(MSE) \sim a_0 + a_1 \log(N) + a_2 \log(\tau)$ —same as Figure 4.12. Figure 5.17 shows that the MSE of auto-correlated data behaves similar to the non-correlated data (compare to Figure 4.12). The MSE is consistent as  $\tau$  increases as well as  $N$  increases. The ML algorithm significantly reduces the MSE compare to LS. The ML algorithm is under the assumption of *i.i.d.* data, it is not optimal for correlated data, however, the ML estimation is still acceptable and the MSE behaviour follows the theoretical interpretation discussed in section 4.5.1.

Compared to Figure 4.12, the auto-correlated data increases MSE of the dispersion parameter estimates  $\hat{\phi}_t$  and  $\hat{\beta}_k$  slightly, by 40% and 5%, respective. However, the MSE of the mean parameter estimates  $\hat{\mu}_t$  and  $\hat{\alpha}_k$  are greatly increased, by 547% and 137%. Also shown that the auto-correlated data have much larger effects on the estimation of time components,  $\mu_t$  and  $\phi_t$ , than on the estimation

of slice components,  $\alpha_k$  and  $\beta_k$ . A possible reason for this is that the estimation of time components is affected by 3-D correlation, while the estimation of slice components is affected by 2-D correlation.

## 5.5 Concluding Remarks

This chapter provides a very practical way to quickly generate uncertainties for quantified PET measurements. Building on the work, presented in chapter 4, on analysis of the distributional characteristics of iteratively reconstructed PET data, we construct an auto-regression model for analysis of the 3-D spatial auto-covariance structure of iteratively reconstructed data, after normalisation. Appropriate likelihood-based statistical techniques for estimation of the auto-regression model coefficients are described. The fitted model leads to a simple process for approximate simulation of scanner performance—one that is readily implemented in an R script. Thus the analysis provides a practical mechanism for evaluating the operational error characteristics of iteratively reconstructed PET images. Simulation studies are used for validation. The approach is illustrated on QA data from an operational clinical scanner. Overall the method is found to be practical and effective.

# Chapter 6

## Discussion, Conclusions and Future Work

### 6.1 Discussion

The work in this thesis is based on the quality assurance data of clinical 3-D PET scanners, or more specific, the reconstructed PET images of uniform cylindrical phantom. The research of this kind of data has been reported on both statistical and engineering literatures over the past few decades. Many different points of view have been taken. Our work provides a sophisticated method for characterisation and simulation of PET data, which has potential to lead to improved clinical decision making. A multiplicative Gamma model and a 3-D spatial auto-regressive model are discussed with a rich detailed description. Once the model has been determined, the simulation of the properties of PET scanner is straightforward. All the analysis in this thesis can be implemented in R, and so it is very practical for routinely assessing the noise characteristics of PET measurements.

Quantitative interpretation of PET scans by region of interest (ROI) evaluation of simple averages or perhaps even more elaborate calculations based on detailed modelling of a dynamic time-activity-curve, can benefit from a better understanding of the stochastic structure of the input data. While simulation based propagation of detector domain noise to the ROI measurements is the most satisfactory theoretical approach to evaluate the noise properties in PET image, there are many situations where the analyst does not have access to the raw detector domain data. As noted by Carson et al. [19], in a practical setting the analysis of ROI value is often carried out long after the raw projection data have already been archived and cannot easily be obtained for calculation. Thus, it is desirable

to develop a variance estimation method that does not require retrieval of raw projection data. In 1993, Carson et al. [19] developed an approximation formula for the variance of ROI values without accessing the raw projection data, therefore, the formula could be routinely used in clinical practice. A refinement of this technique has been proposed by Maitra and O’Sullivan [62] in 1998 which describes that the reconstruction kernel can be approximated by a weighted sums of Gaussian density functions. Although the above approximation based estimators of bias and variance are convenient for calculation, these estimators are based on a series of assumptions which may not be realistic for some PET data analyses. Thus, it is still worthwhile to generate the model based parameter estimation approach which allows a very trivial process to be used for simulation of the scanner. In addition, most of the analysis of statistical variation in PET data [2, 19, 46, 50, 62, 107] has necessarily concentrated on classical filtered-backprojection (FBP) reconstruction. In recent time, however, the iteratively expectation-maximisation (EM) reconstructions are the most popular method in clinical imaging. Such reconstruction impose positivity constraints that lead to noise characteristics in the reconstructed image, which can be very different from the ones in the FBP reconstructed images. Therefore, previous methods seem to be antiquated and outdated.

Our preliminary analysis, presented in 4.1.3, shows that the iteratively reconstructed PET data are non-Gaussian—typically right-skewed, while the FBP data can be well characterised by Gaussian distribution. This has largely encouraged the author to build an efficient Gamma model for PET data. Motivated by a recently acquired physical phantom study of a PET/CT scanner, we propose, in Chapter 4, a Gamma parameterisation of the reconstructed data. An iterative approach of using iteratively re-weighted least squares (IRLS) techniques and Newton’s method has been adapted to estimate parameters. The accuracy and consistency of the model are verified by numerical simulation study.

Similar work has been reported by Teymurazyan et al. [109] in 2013. Using simple exploratory methods such as Q-Q plots, their work suggests Gamma distribution in representing the EM-reconstructed PET data while both Gamma and Normal statistics are equally valid for FBP reconstructions. Nevertheless, we use more formal and sophisticated methods to investigate the applicability of Gamma distribution in representing EM reconstructed data, using data sets collected over 43 PET scanners in the US (ACRIN) and a local hospital (CUH). The methods involve likelihood ratio test and use probability transformed residuals for model diagnostic. We also consider implications of the Gamma model

for ROI analysis, which involves using Gamma-based likelihood to estimate the bias and variance in the PET data. To the best of our knowledge, experimental evaluations describing the Gamma characteristics of noise in EM-reconstructed PET images have yet to appear in the literature.

The noise properties of the EM algorithm using Log-normal distribution were also studied in the literature, *e.g.*, Barrett et al. [7]. Based on some theoretical analyses of EM algorithm, the Log-normal distribution was obtained for the intensity level of each pixel. Their method was based on the assumption that the noise in the reconstruction is relatively small, *i.e.*, the number of counts is large and/or the iteration number is small. To demonstrate the superiority of the Gamma model over the Log-normal, we simply compared the likelihood ratio of these two distributions. Our result, shown in Figure 4.13, finds that especially in the early time frames (lower count), the Gamma model is more plausible. Similar to Figure 4.14, Figure 6.1 compares Gamma and Log-normal model for the simulated data with different iteration numbers and counts. The left group indicates that when the number of counts is low ( $1e+5$ ) and iteration number is large (64), that is noise level relatively high, Log-normal model is not appropriate.

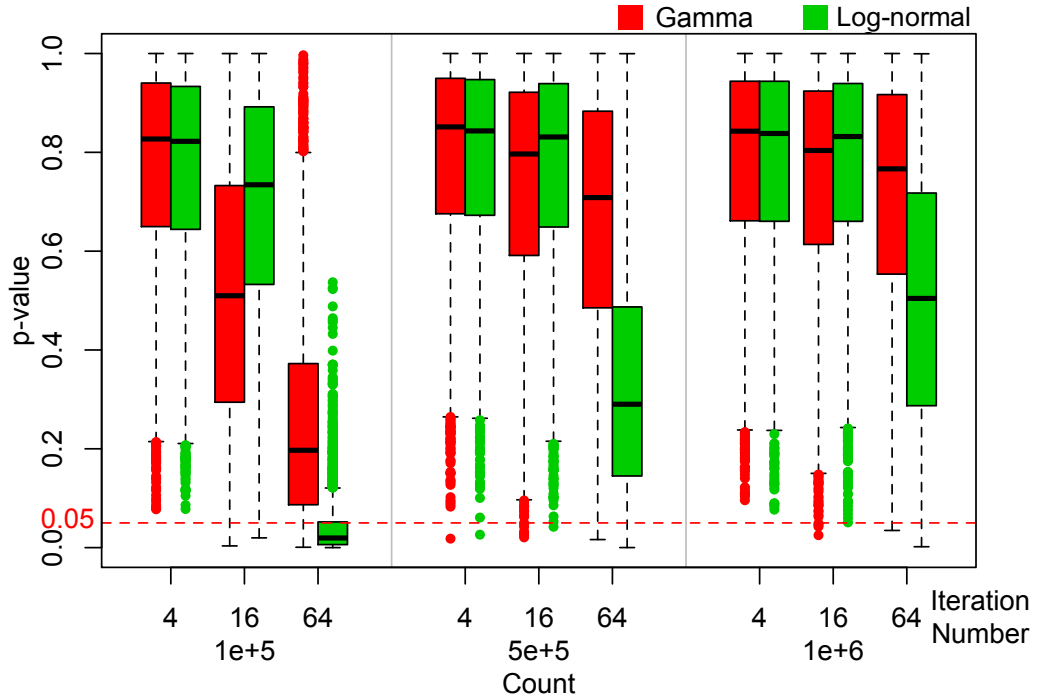


Figure 6.1: The Kolmogorov-Smirnov test  $p$ -values of Gamma and Log-normal model for numerical phantom simulation data with different iteration numbers (4, 16, 64) and counts ( $1e+5$ ,  $5e+5$ ,  $1e+6$ ).

Compared to the variance, the noise correlation of PET image data is much

less investigated in literature and normally considered in 1-D and 2-D mode [5, 18, 81, 89, 88, 89]. In Chapter 5, we have described a practical approach to using physical phantom data to obtain a statistical understanding of the imaging characteristics of an operational scanner that uses iterative reconstruction. The approach is based on a 3-D model taking account of the Gamma-characteristic of positivity constrained iterative reconstruction, and a novel application of spatial auto-regressive (SAR) modelling to describe covariance patterns. The SAR analysis uses a variation on the Whittle [121] approach for implementation of conditional likelihood estimation in general SAR models. Numerical studies demonstrates the reliability of the SAR estimation procedure. These results are fully in line with asymptotic theory, see *e.g.* [69].

Our techniques which are implemented in R, are applied to data from a PET scanner in operational clinical use. Second-order SAR models are found to adequately represent auto-correlation of the normalised phantom data. This extends the analysis reported in [70]. A numerical phantom study using both uniform and non-uniform (VSK) source distributions, indicates that after normalisation via an appropriate Gamma model probability transform [70], the 2-D autocorrelation pattern of iteratively reconstructed data does not appear to depend on whether the source is uniform or non-uniform. This merits more detailed investigation. A systematic study of the factors that influence the nature of local Gamma-model parameters associated with non-uniform sources would also be evaluable next step. This could lead to a practical and efficient approach to obtaining uncertainties for regional summaries of PET scanning information in clinical settings and would be particularly valuable in situations where the bootstrap [50] might not be routinely feasible.

Our simplified approach to representing the statistical characteristics of an operational 3-D scanner, though obviously much less sophisticated than a proper physical representation, may have some on-going value, particularly as the ability to fully represent all of the details of the operational scanner is challenging. The parsimony offered by the approach described here, should be of practical value.

***Implication for patient data:*** In recent years, PET imaging has become the most important diagnostic tool for the detection, localisation, characterisation, and staging of cancer. However, the generally low signal to noise ratio (SNR) and the relatively low spatial resolution of PET limit the detection sensitivity and quantification accuracy [114]. After all the investigations of phantom and simulation studies, the ultimate purpose of our research is to improve the

clinical diagnostic. Based on our practical and effective modelling of the noise structure in PET phantom images, the Gamma distribution could be included in modelling the noise characteristics in patient images. For instance, the lesion detection and characterisation can be badly affected by the spatial characteristics and low-contrast data [105]. Our method could be adapted to estimate the spatial characteristics (mean, variance and correlation structure) of the lesions and to compare the corresponding characteristics with normal anatomical structures.

## 6.2 Conclusions

Overall, this thesis demonstrates the investigations of noise characteristics in reconstructed PET images. A novel approach of model fitting and diagnostics incorporating the Gamma distribution has been developed for analysis of iterative reconstructed data and demonstrated to be a promising step towards an enhanced statistical efficiency of inferences obtained from such data. The exhibited Gamma-structure of iteratively reconstructed PET data indicates that noise reduction algorithms specifically designed for Poisson or Gaussian noise are not appropriate. We explore, for the first time in literature, the adaptability of spatial auto-regressive model for PET imaging data. Spatial auto-regressive modelling in combination with the Gamma distribution based modelling provides a very useful and practical mechanism for quality assessment of operational clinical scanners.

## 6.3 Future Work

In this thesis, several new approaches for estimating statistical characteristics in PET data were proposed and implemented. The models mentioned above are starting points for future work. Further investigations and developments to refine these techniques to provide a quantification of noise characteristics in a non-PET imaging modality data such as MRI and low-dose CT data, are clearly of interest.

### 6.3.1 Generalisation to other medical imaging modalities

Nowadays, low-dose CT scan screening are widely used for early detection of cancers including lung cancer, one of low-dose CT data analysis challenges is high noise. Since the reconstruction methods used in CT imaging are similar to PET, it is reasonable to explore the statistical characteristics in low-dose CT

data using techniques developed in this thesis. Although reconstruction methods used in MRI imaging are quite different, it is still interesting to adapt empirical noise modelling approaches developed in this thesis to MRI data.

### 6.3.2 Generalisation to non-uniform PET images

All the physical phantom data analysed in this thesis are from uniform cylindrical phantom scans. While we have done some simulation studies of VSK phantom in Chapter 5, it is important to test and evaluate the obtained results on non-uniform physical phantom data, *i.e.*, NEMA phantoms [96]. This information is important for the further analysis of patient data.

### 6.3.3 Using SAR model to analysis the auto-correlation structure in FBP reconstructed PET data

We have demonstrated, in Chapter 5, that the SAR model is useful in representing auto-correlation structure of IR data. While it may also be efficient for FBP reconstructed data. As shown in Figure 6.2, the auto-correlation structure in FBP data is quite different from IR data (compare to Figure 5.1). Both transaxial and axial auto-correlation functions have longer tails, so that the SAR model should be modified in order to fit the data.

### 6.3.4 Explore the robustness of the methods

Although our multiplicative model is based on the Gamma assumption, it is not specialised for Gamma distributed data. Another future interest would be to justify methods with good performance when there are small departures from Gamma distribution. Here we simply present a Gaussian simulation study to show the robustness of the methods in one sense. Based on the simulation procedure in section 5.2.6, we replace the Gamma model by Gaussian with parameters mean  $\mu$  and variance  $\mu\phi/\tau$ . An appropriate value is added to each point to avoid infinite values in the computation with gamma function (always positive values). Then the simulated data should be able to fit our Gamma model. The parameter estimation result is shown in Figure 6.3 with the true value in black and the estimates in red. The mean squared errors for each estimate are indicated on the plots. This result is indicating that our Gamma model is applicable for Gaussian distribution.

In addition, we have presented some analysis based on FBP data—widely



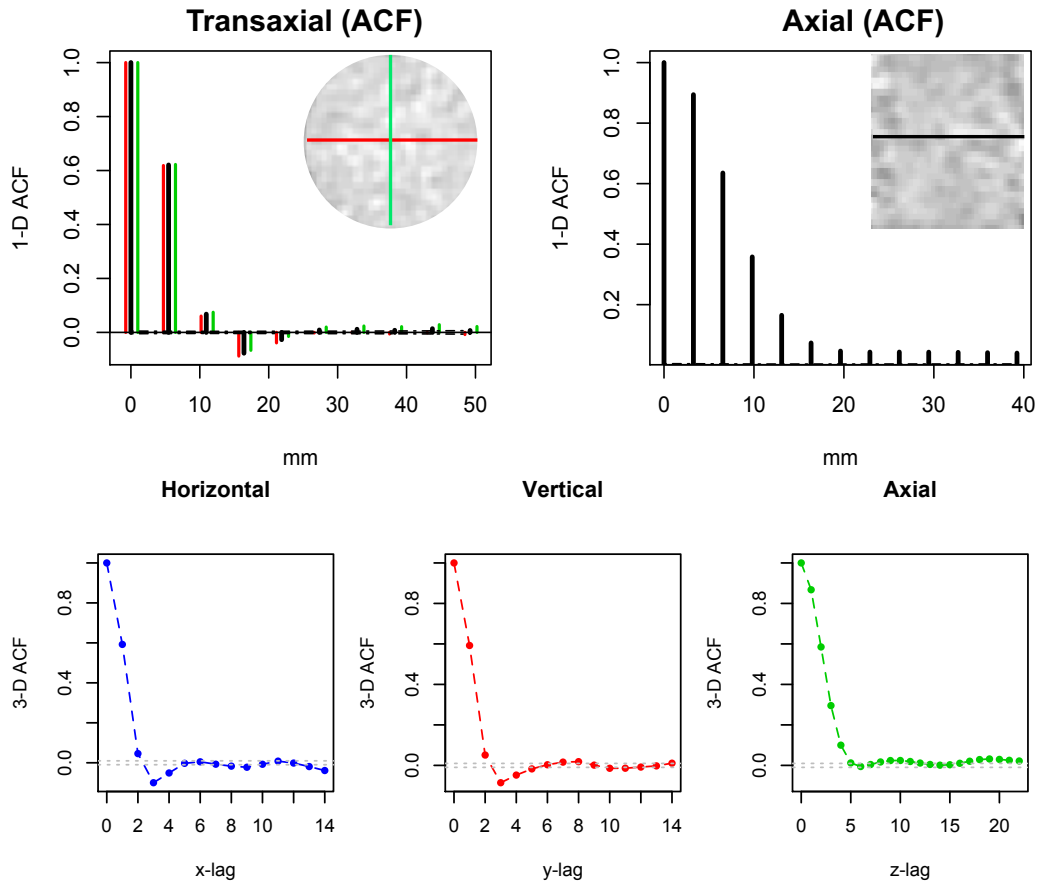


Figure 6.2: Top: Estimated transverse and axial autocorrelation functions (1-D ACF) for FBP reconstructed phantom data. The red and green lines in the transverse plot represent auto-correlation in row and column directions, respectively. Bottom: 3-D ACF for the same phantom. 1-D profiles through the centre of the phantom, showing from left to right, horizontal, vertical, and axial profile.

considered as Gaussian, in chapter 4 shown in Figure 4.7 and 4.8. In this case, our Gamma model performs as well as the LS estimation and produces normal residuals. These results show some robustness of the proposed multiplicative model against deviation from the assumed Gamma distribution. Further study along this direction can be considered as future work.

### 6.3.5 Explore alternative parametrizations

Chapter 4 provides a novel and efficient approach for estimating the axial and temporal bias and variance of PET data. The estimated bias and variance show some smoothness characteristics (Figure 4.8 A & B). Incorporating smooth functions into multiplicative model of PET data could reduce the number of parameters and provide better understanding of the noise characteristics of PET images across spatial locations and time frames. As a future work, we could consider

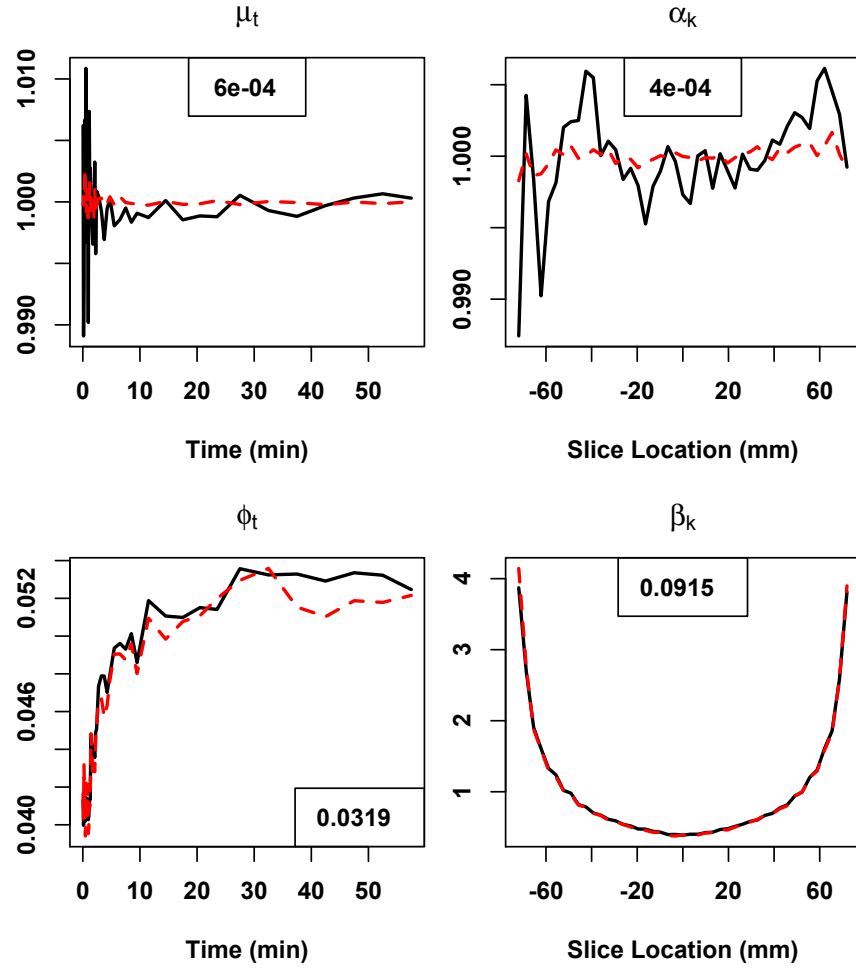


Figure 6.3: Gamma model estimation result for Gaussian simulated data with corresponding mean squared error for each estimate.

incorporating a quadratic function or general b-spline function into the model, and then examine the efficiency and robustness of the estimation result.

# Appendix A

## List of Publications and Presentations by the Author

### A.1 Conference Proceedings related to Chapter 3

T. Mou, J. Huang, B. Elston, P. Kinahan, M. Muzi, A. Opanowski, Y. Zhang and F. O’Sullivan, “Examination of Spatial Covariance Characteristics in a Collection of 3-D PET scanners used in Clinical Imaging Trials,” *IEEE NSS & MIC Record 2014*.

T. Mou, J. Huang, Y. Zhang, P. Kinahan and F. O’Sullivan, “An improved statistical approach to the estimation of spatial bias and variability in reconstructed PET Data,” *IEEE NSS & MIC Record 2015*.

### A.2 Publications related to Chapter 4

T. Mou, J. Huang and F. O’Sullivan, “The Gamma Characteristic of Reconstructed PET Images: Implications for ROI Analysis,” *IEEE Transactions on Medical Imaging*, vol. 37, no. 5, pp. 1092–1102, May 2018. URL: <https://ieeexplore.ieee.org/document/8119532/>

### A.3 Publications related to Chapter 5

T. Mou, J. Huang and F. O’Sullivan, “Empirical Representation of the Scanning Characteristics of an Operational PET/CT: Making use of Quality Assurance Data,” *IEEE Transactions on Medical Imaging*, under review.

## A.4 Other Publications

N. M. Hughes, T. Mou, K. N. O'Regan, P. Murphy, J. N. O'Sullivan, E. Wolsztynski, J. Huang, M. Kennedy, J. F. Eary, and F. O'Sullivan, "Prognostic value of tumor heterogeneity evaluated by FDG-PET/CT imaging in lung cancer patients," *Journal of Clinical Oncology*, 34:15\_suppl, 11564–11564, 2016.

N. M. Hughes, T. Mou, K. N. O'Regan, P. Murphy, J. N. O'Sullivan, E. Wolsztynski, J. Huang, M. Kennedy, J. F. Eary, and F. O'Sullivan, "Tumour heterogeneity measurement using [ $^{18}\text{F}$ ] FDG PET/CT shows prognostic value in patients with non-small cell lung cancer," *European Journal of Nuclear Medicine and Molecular Imaging*, under review.

E. Wolsztynski, J. O'Sullivan, N. M. Hughes, T. Mou, P. Murphy, F. O'Sullivan, and K. O'Regan, "Combining structural and textural assessments of volumetric FDG-PET uptake in NSCLC" *Transactions on Radiation and Plasma Medical Sciences*, under review.

F. Fan, T. Mou, B. Nurhadia and Y. H. Roos, "Water sorption-induced crystallization, structural relaxations and strength analysis of relaxation times in amorphous lactose/whey protein systems," *Journal of Food Engineering*, vol. 196, pp. 150–158, March 2017.

## A.5 Conference Presentations

1. T. Mou, J. Huang, B. Elston, P. Kinahan, M. Muzi, A. Opanowski, Y. Zhang and F. O'Sullivan, "Examination of Spatial Covariance Characteristics in a Collection of 3-D PET scanners used in Clinical Imaging Trials," *IEEE NSS & MIC Record 2014*, M10-22, Seattle, WA USA, Nov. 8–15, 2014. [Poster presentation]
2. T. Mou, J. Huang, Y. Zhang, B. Elston, P. Kinahan, M. Muzi, A. Opanowski and F. O'Sullivan, "Statistical Analysis of a Collection of 3-D PET scanners used in Clinical Imaging Trials," *35<sup>th</sup> Conference on Applied Statistics in Ireland (CASI)*, Cork, Ireland, 11–13 May, 2015. [Poster presentation]
3. T. Mou, J. Huang, Y. Zhang, P. Kinahan and F. O'Sullivan, "An improved statistical approach to the estimation of spatial bias and variability in re-

- constructed PET Data,” *IEEE NSS & MIC Record 2015*, San Diego, CA 92108, USA, Oct. 31–Nov. 7, 2015. [Poster presentation]
4. T. Mou, J. Huang and F. O’Sullivan, “The role of the Gamma Distribution in representing Positron Emission Tomography measurements,” *Royal Statistical Society International Conference (RSS)*, Manchester, UK, 5–8 Sept. 2016. [Poster presentation]
  5. T. Mou, J. Huang and F. O’Sullivan, “An Examination of the Role of the Gamma Model in Approximating of the Distribution of Reconstructed PET Data,” *International Chinese Statistical Association (ICSA) International Conference*, Shanghai, China, 19–22 Dec. 2016. [Oral presentation]
  6. T. Mou, J. Huang and F. O’Sullivan, “Empirical representation of the performance of an operational PET scanner,” *37<sup>th</sup> Conference on Applied Statistics in Ireland (CASI)*, Mullingar, Co. Westmeath, Ireland, 15–17 May, 2017. [Oral presentation]
  7. T. Mou, J. Huang, E. Wolsztynski and F. O’Sullivan, “Implications for Gamma characteristic of reconstructed PET data,” *Joint Statistical Meetings (JSM)*, Baltimore, Maryland, USA, Jul. 29–Aug. 3, 2017. [Poster presentation]
  8. T. Mou, J. Huang, Z. Xiu and F. O’Sullivan, “Fitting Spatial Auto-Regression Models to 3-D PET Imaging Data,” *Royal Statistical Society Annual Conference (RSS)*, Glasgow, UK, 4–7 Sept. 2017. [Oral presentation]
  9. J. Huang, T. Mou and F. O’Sullivan, “Application of Gamma Statistics in the Analysis of Kinetic Models for Dynamic PET Time Course Data,” *Society of Nuclear Medicine and Molecular Imaging (SNMMI) Annual Meeting*, San Diego, CA USA, June 11–15, 2016. [Oral presentation]
  10. N. M. Hughes, P. Murphy, T. Mou, E. Wolsztynski, J. Huang, F. O’Sullivan and K.N. O’Regan, “Tumour heterogeneity measurement using [<sup>18</sup>F] FDG PET/CT in patients with lung cancer,” *European Congress of Radiology Conference (ECR)*, Vienna, Austria, March 2–6, 2016. [Oral presentation]
  11. N. M. Hughes, T. Mou, K. N. O’Regan, P. Murphy, J. O’Sullivan, E. Wolsztynski, J. Huang, M. Kennedy, J. F. Eary, F. O’Sullivan, “Prognostic value of tumor heterogeneity evaluated by FDG-PET/CT imaging in lung cancer

patients,” *American Society of Clinical Oncology (ASCO) Annual Meeting*,  
Chicago, IL USA, June 2–6, 2016. [Poster presentation]

# Appendix B

## R code

```
#####  
#-----Read in DICOM Data-----#  
#####  
library(oro.dicom)  
  
# Set up directory  
dname='/Users/tian/Desktop/CUH_Phantom_070317/DICOM_PET_WB_3D'  
setwd(dname)  
  
# Read in DICOM data; nz - slice; nt - time frame  
n=128;N=n*n;nz=47;nt=45  
img=NULL  
slp=NULL  
int=NULL  
rsimg=NULL  
header=NULL  
ld=dir()  
for(i in 1:length(dir())){  
x=readDICOMFile(ld[i])  
img=c(t(x[[2]]))  
# slope and intercept, check row/column number  
slp1 = as.numeric(x[[1]][259,6])  
int1 = as.numeric(x[[1]][258,6])  
cimg=c(img)*slp1+int1  
slp=c(slp,slp1)  
int=c(int,int1)
```

## B. R CODE

```

rsimg=cbind(rsimg,cimg)
}

sIR=array(c(rsimg),dim=c(n,n,nz,nt))
save(sIR,file='sIR.RData')

sFBP=array(c(rsimg),dim=c(n,n,nz,nt))
save(sFBP,file='sFBP.RData')

#####
#-----Extract ROI Data-----#
#####
load(file='sIR.RData') # load(file='sFBP.RData')
s=sIR
x1pix=5.46875; x2pix=x1pix ; x3pix=3.27 # pixel size
z=x3pix*( (1:nz)-(nz+1)/2 )
x1 = x1pix*( (1:n)-(n+1)/2 ) ; x2=x1
dur = c(rep(5,16),rep(10,7),rep(30,5),rep(60,5),rep(180,5),
rep(300,7))
te=cumsum(dur)
ts=te-dur
tme=(ts+te)/120
lam=log(2.)/109.77
# proportional to inverse variance
wme=(dur/60) * exp(0-lam*tme) ; wme=wme/max(wme)
xm = matrix(rep(x1,n),ncol=n) ; ym=t(xm)
x = array(rep(c(rep(c(xm),nz)),nt),c(n,n,nz,nt))
y = array(rep(c(rep(c(ym),nz)),nt),c(n,n,nz,nt))
tm=NULL ; for(i in 1:nt) { tm = c(tm,rep(tme[i],n*n*nz)) }
wm=NULL ; for(i in 1:nt) { wm = c(wm,rep(wme[i],n*n*nz)) }
zm=NULL ; for(i in 1:nz) { zm = c(zm,rep(z[i],n*n)) }
zm=rep(zm,nt)

zv = array(zm,c(n,n,nz,nt))
tv = array(tm,c(n,n,nz,nt)) ; wv = array(wm,c(n,n,nz,nt))
rv = sqrt(x*x+y*y); xv=x ; yv=y
rm(xm);rm(ym);rm(tm);rm(x);rm(y);rm(wm)

```



## B. R CODE

```
# Plot transverse and sagittal view
sIR=s
par(mfrow=c(2,2),cex=0.7,mai=c(0.6,0.1,0.3,0),oma=c(0,0,0,0),
    font=2,font.axis=2,font.lab=2,cex.lab=1.5,cex.axis=1.4)
gs=grey((0:128)/128)
image(sIR[, , 23, 24], col=gs, axe=F, xlab="X (mm)", ylab="", asp=1)
mtext("Transverse", side=3, line=-2, cex=1.5, col="white")
axis(1, at=c(0, 0.5, 1), labels=c(-350, 0, 350))
axis(2, at=c(0, 0.5, 1), pos=0, labels=c(-350, 0, 350))
title(ylab="Y (mm)", line=-3)
title(ylab="2017", line=-1.5, cex.lab=2)
image(t(sIR[65, , , 24]), col=gs, axe=F, xlab="Z (mm)", ylab="",
      asp=700/220)
mtext("Sagittal", side=2, line=-6, cex=1.5)
axis(1, at=c(0, 0.5, 1), labels=c(-78, 0, 78))
axis(2, at=c(0, 0.5, 1), pos=0, labels=c(-350, 0, 350))
title(ylab="Y (mm)", line=-8)

# Define a mask with radius = 80mm
par(mfrow=c(2,2))
mrv=rv[, , 1, 1]
m=c(mrv)
mm=rep(0, N)
for(i in 1:N){
  if(m[i]<=80){mm[i]=1}
  if(m[i]>80){mm[i]=0}
}
m=matrix(mm, ncol=n, nrow=n)
image(m)
mask=array(rep(c(m), nt), c(n, n, nt))
mask[, , 1]=0; mask[, , nt]=0
# Check the region of mask
test=sIR[, , 23, 23]
test[m==1]=0
image(test)
save(mask, file='mask(r<=80mm).RData')
```

## B. R CODE

```
# Extract the ROI data
load(file="mask(r<=80mm).RData")
nv=n*n*nz*nt

# Phantom Data and Axial Indicator
s=sIR
axial=mask*0 ; axp=NULL
for(z in 1:nz) { axial[, , z]=z+mask[, , z]*0 }
axp = c(axial)[c(mask)>0]
sp=NULL
for(t in 1:nt) { sp=cbind(sp,c(s[, , t])[c(mask)>0] ) }
tp=NULL
for(t in 1:nt) { tp=cbind(tp,c(tv[, , t])[c(mask)>0] ) }
wp=NULL
for(t in 1:nt) { wp=cbind(wp,c(wv[, , t])[c(mask)>0] ) }
zp=NULL
for(t in 1:nt) { zp=cbind(zp,c(zv[, , t])[c(mask)>0] ) }
rp=NULL
for(t in 1:nt) { rp=cbind(rp,c(rv[, , t])[c(mask)>0] ) }
xp=NULL
for(t in 1:nt) { xp=cbind(xp,c(xv[, , t])[c(mask)>0] ) }
yp=NULL
for(t in 1:nt) { yp=cbind(yp,c(yv[, , t])[c(mask)>0] ) }

rm(s) ; rm(tv) ; rm(zv) ; rm(wv) ; rm(rv)

sp=c(sp);tp=c(tp);zp=c(zp);rp=xlpix*round(c(rp)/xlpix)

save(sp,file='sp.RData')
save(tp,file='tp.RData')
save(xp,file='xp.RData')
save(yp,file='yp.RData')
save(zp,file='zp.RData')
save(rp,file='rp.RData')
```

## B. R CODE

```
#####  
#-----Chapter 3 Spatial Statistical Characteristics-----#  
#####  
#Source subfunctions first - file name: "CQIE-subfun.R"##  
library(MASS) ; library(ic.infer)  
  
# Multiplicative Bias Adjustment FUNCTION  
  
biass <- function(tp,zp,rp,sp,pp,it,iz,ir) {  
  
  sp0 = sp/(mean(sp)) ; mu0=mean(sp)  
  
  # Temporal  
  wt=as.vector(tapply((tp*0+1),tp,sum))  
  yt=tapply(sp0,tp,mean) ; xt=sort(unique(tp))  
  out=smooth.spline(xt,yt,w=wt,df=pp*length(yt))  
  tt=predict(out)$x ; mut=predict(out)$y  
  sp1 = sp0/(approx(tt,mut,xout=tp,rule=2)$y)  
  
  # Axial  
  wt=as.vector(tapply((zp*0+1),zp,sum))  
  yz=tapply(sp1,zp,mean) ; xz=sort(unique(zp))  
  out=smooth.spline(xz,yz,w=wt,df=pp*length(yz))  
  zz=predict(out)$x ; muz=predict(out)$y  
  sp2 = sp1/(approx(zz,muz,xout=zp,rule=2)$y)  
  
  # Radial  
  wt=as.vector(tapply((rp*0+1),rp,sum))  
  yr=tapply(sp2,rp,mean) ; xr=sort(unique(rp))  
  out=smooth.spline(xr,yr,w=wt,df=pp*length(yr))  
  rr=predict(out)$x ; mur=predict(out)$y  
  sp3 = sp2/(approx(rr,mur,xout=rp,rule=2)$y)  
  
  #par(mfrow=c(2,2))  
  plot(xt,yt,pch=16,main="Temporal",xlab="t (min)",  
        ylab=" ",ylim=range(yt,yz,yr))  
  lines(tt,mur,col=4) ; abline(h=1,col=2,lwd=2)
```

## B. R CODE

```

plot(xz,yz,pch=16,main="Axial",xlab="z (mm)",ylab=" ",
      ylim=range(yt,yz,yr))
lines(zz,muz,col=4); abline(h=1,col=2,lwd=2)
plot(xr,yr,pch=16,main="Radial",xlab="r (mm)",ylab=" ",
      ylim=range(yt,yz,yr))
lines(rr,mur,col=4); abline(h=1,col=2,lwd=2)

cf=mu0+sp*0
if(it==1){ cf = cf*(approx(tt,mut,xout=tp,rule=2)$y) }
if(iz==1){ cf = cf*(approx(zz,muz,xout=zp,rule=2)$y) }
if(ir==1){ cf = cf*(approx(rr,mur,xout=rp,rule=2)$y) }
e <- new.env()
e$cf = cf
e$mu = mu0
e$mut = cbind(tt,mut)
e$muz = cbind(zz,muz)
e$mur = cbind(rr,mur)

e

}

# Scale Adjustment for SD
# (ep has mean 1 ; bias adjusted sp data)

sds <- function(tp,zp,rp,ep,pp,it,iz,ir) {

ep0= ep*ep

sd0=sqrt(mean(ep0));ep0=ep0/mean(ep0)

# Temporal
wt=as.vector(tapply((tp*0+1),tp,sum))
yt=tapply(ep0,tp,mean) ; xt=sort(unique(tp))
out=smooth.spline(xt,yt,w=wt,df=pp*length(yt))
tt=predict(out)$x ; mut=predict(out)$y
ep1 = ep0/(approx(tt,mut,xout=tp,rule=2)$y)

```

## B. R CODE

```
# Axial
wt=as.vector(tapply((zp*0+1),zp,sum))
yz=tapply(ep1,zp,mean) ; xz=sort(unique(zp))
out=smooth.spline(xz,yz,w=wt,df=pp*length(yz))
zz=predict(out)$x ; muz=predict(out)$y
ep2 = ep1/(approx(zz,muz,xout=zp,rule=2)$y)

# Radial
wt=as.vector(tapply((rp*0+1),rp,sum))
yr=tapply(ep2,rp,mean) ; xr=sort(unique(rp))
out=smooth.spline(xr,yr,w=wt,df=pp*length(yr))
rr=predict(out)$x ; mur=predict(out)$y
ep3 = ep2/(approx(rr,mur,xout=rp,rule=2)$y)

yt=sqrt(yt) ; yz=sqrt(yz) ; yr=sqrt(yr)
mut=sqrt(mut) ; muz=sqrt(muz) ; mur=sqrt(mur)

plot(xt,yt,pch=16,main="Temporal",xlab="t (min)",
      ylab=" ",ylim=range(yt,yz,yr))
lines(tt,mut,col=4); abline(h=1,col=2,lwd=2)
plot(xz,yz,pch=16,main="Axial",xlab="z (mm)",ylab=" ",
      ylim=range(yt,yz,yr))
lines(zz,muz,col=4); abline(h=1,col=2,lwd=2)
plot(xr,yr,pch=16,main="Radial",xlab="r (mm)",ylab=" ",
      ylim=range(yt,yz,yr))
lines(rr,mur,col=4); abline(h=1,col=2,lwd=2)

cf=sd0+ep*0
if(it==1) { cf = cf*(approx(tt,mut,xout=tp,rule=2)$y) }
if(iz==1) { cf = cf*(approx(zz,muz,xout=zp,rule=2)$y) }
if(ir==1) { cf = cf*(approx(rr,mur,xout=rp,rule=2)$y) }
e <- new.env()
e$cf = cf
e$sd = sd0
e$sdt = cbind(tt,mut)
e$sdz = cbind(zz,muz)
```

## B. R CODE

```
e$sdr = cbind(rr,mur)

e

}

#
# Produce a lagged-version of the data indexed by
# [x,y,z,t] using one of the co-ordinates x,y,z
# (indicated by cflag) . The lag is given by l

# x,y,z,t are integers

dlag <- function(x,y,z,t,data,l,cflag) {

x=as.integer(x) ; y=as.integer(y)
z=as.integer(z) ; t=as.integer(t)
# cflag=1 ; l=1 ; a=38
it=as.integer(unique(sort(t)))
iz=as.integer(unique(sort(z)))
iy=as.integer(unique(sort(y)))
ix=as.integer(unique(sort(x)))

n=length(data) ; ind=c(1:n);data1=rep(NA,n)

# Organize Calculation by time

for( a in it ) {
indt=ind[a==t]
if(cflag==1) { # x-lag
zt=z[indt]
for(k in iz) { indtz=indt[zt==k] ; ytz=y[indtz]
iy=unique(ytz)
for(j in iy) {
inds= indtz[(j==ytz)] ; xs=x[inds]
mxxs=max(xs) ; mnxs=min(xs)
```

## B. R CODE

```

indss=inds[ ((xs+1)<=mxxs)&((xs+1)>=mnxs)]
ns=length(indss)
if(ns>0) { xss=x[indss]
for(i in 1:ns){indil=indss[((xss[i]+1)==xs)]
  if(length(indil)>0){data1[inds[i]]=
    data[indil]}
}}
  } # j
} # k
} # cflag =1
if(cflag==2) { # y-lag
zt=z[indt]
for(k in iz) { indtz=indt[zt==k] ; xtz=x[indtz]
  ix=unique(xtz)
for(j in ix) {
inds= indtz[(j==xtz)] ; ys=y[inds]
mxys=max(ys) ; mnys=min(ys)
indss=inds[ ((ys+1)<=mxys)&((ys+1)>=mnys)]
ns=length(indss)
if(ns>0) { yss=y[indss]
for(i in 1:ns){indil=inds[((yss[i]+1)==ys)]
  if(length(indil)>0){data1[inds[i]]=
    data[indil]}
}}
  } # j
} # k
} # cflag =2
if(cflag==3) { # z-lag
yt=y[indt]
for(k in iy) { indty=indt[yt==k] ; xtz=x[indty]
  ix=unique(xtz)
for(j in ix) {
if(length(indty[(j==xtz)])>0){
inds= indty[(j==xtz)] ; zs=z[inds]
mxzs=max(zs) ; mnzs=min(zs)
indss=inds[ ((zs+1)<=mxzs)&((zs+1)>=mnzs)]
ns=length(indss)

```

## B. R CODE

```

if(ns>0) { zss=z[indss]
for(i in 1:ns){indil=inds[((zss[i]+1)==zs)]
if(length(indil)>0){datal[inds[i]]=
                        data[indil] }
}}
}

} # j
} # k
} # cflag =3
} # t index
datal
}

#
# Produce a spatial auto-covariance at lag (l,k)
# in one of coordinates x,y and z

acflk <- function(x,y,z,t,data,l,ixy,k) {
# ixy=1 ; l=1 ; k=18
cflag=ixy #lag in x-y domain
datan=dlag(x,y,z,t,data, l,cflag)
cflag=3 #add lag in z domain
datan = dlag(x,y,z,t,datan,k,cflag)

u=data*datan ; v=u[is.na(u)==F];cv=NA;se=NA;ne=0
if(length(v)>0) { cv=mean(v) ; ne=length(v)
                  se = sqrt(var(v)/(ne+.1)) }
e= c(l,k,cv,2*se,round(ne))
e
}

#####END SUBFUNCTIONS#####

# Estimate temporal (t), axial (k) and radial (r) bias
# and standard deviations (SD)
par(mfrow=c(2,3))
pp=.7 ; it=1;iz=1;ir=1; ssp = sp ;cfmu=sp*0+1
for(k in 1:2) { e=biass(tp,zp,rp,ssp,pp,it,iz,ir)

```



## B. R CODE

```

        ssp=ssp/e$cf ; cfm=cfmu*e$cf
if(k==1) { mut=e$mut[,1]*0+1 ; muz=e$muz[,1]*0+1
        mur=e$mur[,1]*0+1 }
if(it>0) {mut=mut*e$mut[,2] }
if(iz>0) {muz=muz*e$muz[,2] }
if(ir>0) {mur=mur*e$mur[,2] }
    }
mut=cbind(e$mut[,1],mut);muz=cbind(e$muz[,1],muz)
mur=cbind(e$mur[,1],mur)

pp=.7 ; it=1;iz=1;ir=1; ep = (sp/cfm-1); cfsd=sp*0+1
for(k in 1:6) { e=sds(tp,zp,rp,ep,pp,it,iz,ir)
        ep=ep/e$cf ; cfsd=cfsd*e$cf
if(k==1) { sdt=e$sdt[,1]*0+1 ; sdz=e$sdz[,1]*0+1
        sdr=e$sdr[,1]*0+1 }
if(it>0) {sdt=sdt*e$sdt[,2] }
if(iz>0) {sdz=sdz*e$sdz[,2] }
if(ir>0) {sdr=sdr*e$sdr[,2] }
    }
sdt=cbind(e$sdt[,1],sdt);sdz=cbind(e$sdz[,1],sdz)
sdr=cbind(e$sdr[,1],sdr)

zp= (zp/x3pix-min(zp)/x3pix )+1
xp= (xp/x1pix-min(xp)/x1pix )+1
yp= (yp/x1pix-min(yp)/x1pix )+1
t=tp*0 ;nd=length(tme)
for(i in 1:nd) { t[tp==tme[i]]=i } ; tp=t

x=as.integer(xp) ; y=as.integer(yp)
z=as.integer(zp) ; t=as.integer(tp)

# Spatial Covariance Patterns

acfsx=NULL ; nz=12 ; nx=9
for(k in 0:nz) {
for(l in 0:nx) {
ixy=1

```

## B. R CODE

```
acfsx=rbind(acfsx,acflk(x,y,z,t,data,l,ixy,k))
}}

acfsy=NULL; nz=12 ; nx=9
for(k in 0:nz) {
  for(l in 0:nx) {
    ixy=2
    acfsy=rbind(acfsy,acflk(x,y,z,t,data,l,ixy,k))
  }
}

mx=matrix(acfsx[,3],ncol=(nz+1))
my=matrix(acfsy[,3],ncol=(nz+1))
xse=matrix(acfsx[,4],ncol=(nz+1))
yse=matrix(acfsy[,4],ncol=(nz+1))
mxa = mx[,1] %o% mx[1,]

# Figure 3.5 top
plot((0:nx)*xlpix,(mx[,1]+my[,1])/2,type="h",lwd=3,
      col=1,xlab="mm",main="Transaxial (ACF) ",ylab=
      "1-D ACF",xlim=range(-1,(xlpix*nx+1)))
points(((0:nx)*xlpix)-.75,(mx[,1]),type="h",lwd=2,col=2)
points(((0:nx)*xlpix)+1,(my[,1]),type="h",lwd=2,col=3)
abline(h=0)
matlines((0:nx)*xlpix,cbind(-2*xse[,1],2*xse[,1]),
          lty=c(4),col=1)

plot((0:nz)*x3pix,mx[1,],type="h",lwd=3,col=1,xlab="mm",
      main="Axial (ACF)",ylab="1-D ACF")
matlines((0:nz)*x3pix,cbind(-2*xse[1,],2*xse[1,]),
          lty=c(4),col=1)
abline(h=0)

# Figure 3.4
par(mfcol=c(3,2),pty="m")
boxplot(sp~round(tp,1),pch=".",ylab="Temporal",main=
        "Raw",xlab="t (min)")
boxplot(sp~round(zp),pch=".",ylab="Axial",xlab=
```

## B. R CODE

```

      "z (mm) ")
boxplot(sp~round(rp),pch=".",ylab="Radial")
ep=(sp/cfmu-1)/cfds
boxplot(ep~round(tp,1),pch=".",xlab="t (min)",main=
      "Standardized")
boxplot(ep~round(zp),pch=".",xlab="z (min)")
boxplot(ep~round(rp),pch=".")

# Figure 3.5 bottom
par(mfrow=c(2,1),pty="m")
phi=1 ; epp=(sp^phi-cfmu^phi)/(cfds/cfmu^phi)
hist(epp,main="Normalized Values")
par(new=T);qqnorm(epp,axes=F,pch=".",xlab=" ",
      ylab="",main=" ",col=4)

phi=.333 ; epp=(sp^phi-cfmu^phi)/(cfds/cfmu^phi)
hist(epp,main="Skew Adjusted Values")
par(new=T);qqnorm(epp,axes=F,pch=".",xlab=" ",
      ylab="",main=" ",col=4)

#####
#-----Chapter 4 Multilicative Gamma Model-----#
#####

####Source subfunctions first - file name: "subfuns.R"####

ls.est <- function(zij,I,J){ # LS estimation
mul=as.vector(tapply(zij,J,mean))
mul=mul/mean(mul)
Mi=NULL;Mj=NULL;error=NULL
for(m in 1:20){
Mul=approx(sort(unique(J)),mul,xout=J,rule=2)$y
mu2=as.vector(tapply(Mul*zij,I,sum))/as.vector(
      tapply(Mul^2,I,sum))
Mu2=approx(sort(unique(I)),mu2,xout=I,rule=2)$y
mul=as.vector(tapply(Mu2*zij,J,sum))/as.vector(
      tapply(Mu2^2,J,sum))

```

## B. R CODE

```

mul=mul/mean(mul)
Mi <- cbind(Mi,mul)
Mj <- cbind(Mj,mu2)
if(m > 1){
  emi <- sum(((Mi[,m]-Mi[,m-1])/Mi[,m])^2)
  emj <- sum(((Mj[,m]-Mj[,m-1])/Mj[,m])^2)
  error <- cbind(error,c(emi,emj))
  if(all(c(error[,m-1])<0.001)){break}}
}
muj=approx(sort(unique(J)),mul,xout=J,rule=2)$y
mui=approx(sort(unique(I)),mu2,xout=I,rule=2)$y
mu0=mui*muj

yikt=((zij-mu0)^2)/mu0

ph1=as.vector(tapply(yikt,J,mean))
ph1=ph1/mean(ph1)
Pi=NULL;Pj=NULL;error=NULL
for(m in 1:20){
  Ph1=approx(sort(unique(J)),ph1,xout=J,rule=2)$y
  ph2=as.vector(tapply(Ph1*yikt,I,sum))/as.vector(
    tapply((Ph1^2),I,sum))
  Ph2=approx(sort(unique(I)),ph2,xout=I,rule=2)$y
  ph1=as.vector(tapply(Ph2*yikt,J,sum))/as.vector(
    tapply((Ph2^2),J,sum))
  ph1=ph1/mean(ph1)
  Pi <- cbind(Pi,ph1)
  Pj <- cbind(Pj,ph2)
  if(m > 1){
    epi <- sum(((Pi[,m]-Pi[,m-1])/Pi[,m])^2)
    epj <- sum(((Pj[,m]-Pj[,m-1])/Pj[,m])^2)
    error <- cbind(error,c(epi,epj))
    if(all(c(error[,m-1])<0.001)){break}}
  }
  phj=approx(sort(unique(J)),ph1,xout=J,rule=2)$y
  phi=approx(sort(unique(I)),ph2,xout=I,rule=2)$y
  phij=phi*phj

```

## B. R CODE

```
e <- new.env()
e$mui = mui
e$mu_j = mu_j
e$phi = phi
e$ph_j = ph_j
e
}

simple <- function(zij,I,J){ # Simple mean and variance
mul=as.vector(tapply(zij,J,mean))
mu2=as.vector(tapply(zij,I,mean))
muz=mul/mean(mul);mur=mu2
mu_j=approx(sort(unique(J)),muz,xout=J,rule=2)$y
mui=approx(sort(unique(I)),mur,xout=I,rule=2)$y
mu0=mui*mu_j

yij=(zij-mu0)^2/mu0

var1=as.vector(tapply(yij,J,mean))
var2=as.vector(tapply(yij,I,mean))
bmu=mean(mu2);bvar=mean(var2)
# adjust the initial mu[j] and phi[j] to have mean 1
varz=var1/mean(var1)
varr=var2

ph_j=approx(sort(unique(J)),varz,xout=J,rule=2)$y;
phi=approx(sort(unique(I)),varr,xout=I,rule=2)$y
phi_j=phi*ph_j

e <- new.env()
e$mui = mui
e$mu_j = mu_j
e$phi = phi
e$ph_j = ph_j
e
}
```

## B. R CODE

```
# ML estimation
est <- function(mui,muj,phi,phj,zij,I,J,lambda,tol){
mu0=mui*muj;phi j=phi*phj
L=NULL;Mi=NULL;Mj=NULL;Pi=NULL;Pj=NULL;error=NULL;Tao=NULL
for(i in 1:50){
gai=mui/phi;thj=muj/phj

# Estimate mui j
e=e_fun(zij,mu0,gai,phi j,J)
thj.hat=e$est

thj=approx(sort(unique(J)),thj.hat,xout=J,rule=2)$y
muj=(thj*phj)/mean(thj*phj) # adjust mu[j] to have mean 1
if(min(muj)<0){muj.hat=-1;mui.hat="negative";break}
mu0=mui*muj

e=e_fun(zij,mu0,thj,phi j,I)
gai.hat=e$est

gai=approx(sort(unique(I)),gai.hat,xout=I,rule=2)$y
mui=gai*phi
if(min(mui)<0){mui.hat=-1;break}
mu0=mui*muj

# Estimate phi j
mui j=mu0
lambda=rev(sort(lambda))
kk=length(lambda)
sigij=1/phi j;sigi=1/phi;sigj=1/phj

for(m in 1:kk){
lam1 = lambda[m]
dl=zij*sigj-mui j*sigj*log(zij*sigij)-mui j*sigj+mui j*sigj*
  digamma(mui j*sigij)
dl2=(mui j^2)*(sigj^2)*trigamma(mui j*sigij)-mui j*sigj/sigi
hat=as.vector(tapply(dl,I,sum))/as.vector(tapply(dl2,I,sum))
```

## B. R CODE

```

hat2=as.vector(tapply(sigi,I,unique))-lam1*hat
if(min(hat2)>0) {break}
}
sigi.hat=hat2
sigi=approx(sort(unique(I)),sigi.hat,xout=I,rule=2)$y

sigij=sigi*sigj

for(m in 1:kk){
lam2 = lambda[m]
dl=zij*sigi-muij*sigi*log(zij*sigij)-muij*sigi+muij*sigi*
  digamma(muij*sigij)
dl2=(muij^2)*(sigi^2)*trigamma(muij*sigij)-muij*sigi/sigj
hat=as.vector(tapply(dl,J,sum))/as.vector(tapply(dl2,J,sum))
hat2=as.vector(tapply(sigj,J,unique))-lam2*hat
if(min(hat2)>0) {break}
}
sigj.hat=hat2
# adjust phi[j] to have mean 1
pj=(1/sigj.hat)/mean(1/sigj.hat)
sigj.hat=1/pj
sigj=approx(sort(unique(J)),sigj.hat,xout=J,rule=2)$y

sigij=sigi*sigj
phi=1/sigij;phi=1/sigi; phj=1/sigj

mui.hat=as.vector(tapply(mui,I,unique));bmu=mean(mui.hat)
mui.hat=mui.hat/bmu
muj.hat=as.vector(tapply(muj,J,unique))
phi.hat=1/sigi.hat;bphi=mean(phi.hat);phi.hat=phi.hat/bphi
phj.hat=1/sigj.hat
Mi <- cbind(Mi,mui.hat)
Mj <- cbind(Mj,muj.hat)
Pi <- cbind(Pi,phi.hat)
Pj <- cbind(Pj,phj.hat)
if(i > 1){
emi <- sum(((Mi[,i]-Mi[,i-1])/Mi[,i])^2)

```

## B. R CODE

```

emj <- sum(((Mj[,i]-Mj[,i-1])/Mj[,i])^2)
epi <- sum(((Pi[,i]-Pi[,i-1])/Pi[,i])^2)
epj <- sum(((Pj[,i]-Pj[,i-1])/Pj[,i])^2)
error <- cbind(error,c(emi,emj,epi,epj))
if(all(c(error[,i-1])<tol)){break} # tolerance error
}}

e <- new.env()
e$mui = mui.hat
e$mu_j = mu_j.hat
e$phi = phi.hat
e$ph_j = ph_j.hat
e$error = error
e$bmu = bmu
e$bphi = bphi

e
}

e_fun<-function(zij,mu0,hat,phij,location){
xi0 = mu0/phij
wij = trigamma(xi0)
uij=zij/phij
yij = xi0 + (log(uij)-digamma(xi0))/(trigamma(xi0))
wrss = sum(wij*(yij-xi0)^2)

est = as.vector(tapply(wij*yij*hat,location,sum))/
      as.vector(tapply(wij*(hat^2),location,sum))

e <- new.env()
e$wrss = wrss
e$est = est
e
}

#####END SUBFUNCTIONS#####

load("sp.RData")

```



## B. R CODE

```
load("tp.RData")
load("zp.RData")
load("xp.RData")
load("yp.RData")
source("subfun.R")

# FBP
sp=sp+abs(min(sp))+(1e-15)

# IR
sp=sp/mean(sp)
dur = c(rep(5,16),rep(10,7),rep(30,5),rep(60,5),
        rep(180,5),rep(300,7))
te=cumsum(dur)
ts=te-dur
tme=(ts+te)/120
lam=log(2)/109.77
wme=(dur/60) * exp(0-lam*tme)
wme=wme/max(wme)

zz=sort(unique(zp))

#
# Estimation
#
flag=1
zij=sp
lambda=c(1:10)/10;tol=0.001

# Generate I,J
I=tp;J=zp

# Least square estimation
init1=ls.est(zij,I,J)
mui=init1$mui;muj=init1$muj;phi=init1$phi;phj=init1$phj

mul=as.vector(tapply(mui,I,unique));mul=mul/mean(mul)
```

## B. R CODE

```
mu2=as.vector(tapply(mu_j,J,unique))
ph1=as.vector(tapply(phi,I,unique));ph1=ph1/mean(ph1)
ph2=as.vector(tapply(ph_j,J,unique))

if(flag==1){ # Initial value - LS estimates
  mui=init1$mui;mu_j=init1$mu_j
  phi=init1$phi;ph_j=init1$ph_j
}
if(flag==2){ # Initial Value by Simple mean and var
  init2=simple(zij,I,J)
  mui=init2$mui;mu_j=init2$mu_j
  phi=init2$phi;ph_j=init2$ph_j
}

# ML estimation
e=est(mui,mu_j,phi,ph_j,zij,I,J,lambda,tol)

mui.hat=e$mui
mu_j.hat=e$mu_j
phi.hat=e$phi
ph_j.hat=e$ph_j
error=e$error
bmu=e$bmu
bphi=e$bphi

# Figure 4.8 - Gamma model fit
par(mfcol=c(2,3),cex=0.7,mai=c(0.7,0.7,0.6,0),
    oma=c(0,0,0,0.7),font=2,font.axis=2,font.lab=2)
plot(tme,mu1-1,type="l",main="Temporal",lwd=2,xlab=
     "t (min)",ylab="Bias",ylim=c(-0.017,0.017),cex.lab=
     1.6,cex.main=1.8,cex.axis=1.4)
abline(h=0,lty=2,col="grey")
lines(tme,mui.hat-1,lty=2,col=2,lwd=2)
legend("top",legend=c("LS","ML"),lty=c(1,2),col=c(1,2),
      lwd=2)

plot(tme,ph1*wme/sum(ph1*wme),ylim=c(0.016,0.029),type="l",
```

## B. R CODE

```

        lwd=2,xlab="t (min)",ylab="Variance",cex.lab=1.6,
        cex.axis=1.4)
lines(tme,(phi.hat*wme/sum(phi.hat*wme)),lty=2,col=2,lwd=2)
legend("bottom",legend=c("LS","ML"),lty=c(1,2),col=c(1,2),
      lwd=2)

plot(zz,mu2-1,type="l",main="Axial",lwd=2,xlab="k (mm)",
      ylab="",ylim=c(-0.032,0.017),cex.lab=1.6,cex.main=1.8,
      cex.axis=1.4)
abline(h=0,lty=2,col='grey')
lines(zz,muj.hat-1,lty=2,col=2,lwd=2)
legend("bottom",legend=c("LS","ML"),lty=c(1,2),col=c(1,2),
      lwd=2)

plot(zz,ph2,type="l",lwd=2,xlab="k (mm)",ylab="",cex.lab=1.6,
      cex.axis=1.4)
lines(zz,phj.hat,lty=2,col=2,lwd=2)
legend("top",legend=c("LS","ML"),lty=c(1,2),col=c(1,2),lwd=2)

# Normalized model residuals
library(MASS)
muij<-approx(sort(unique(I)),mui.hat,xout=I,rule=2)$y *
      approx(sort(unique(J)),muj.hat,xout=J,rule=2)$y*bmu
phij<-approx(sort(unique(I)),phi.hat,xout=I,rule=2)$y *
      approx(sort(unique(J)),phj.hat,xout=J,rule=2)$y*bphi

cdf=pgamma(zij,shape=muij/phij,scale=phij)
res <- qnorm(cdf)

hist(res,main="Multiplicative Model\nResiduals",cex.main=
      1.4,xlab="",ylab="",density=15,cex.lab=1,cex.axis=1.4,
      adj=0.5)
par(new=T)
x<-seq(from=range(res)[1],to=range(res)[2],length.out=1000)
plot(x,dnorm(x,mean=0,sd=1),xlab="",ylab="",axes=F,main="",
      type="l",col=2,lwd=2)

```

## B. R CODE

```
qqplot(res.g, res, pch=20, cex=0.8, main="", xlab="Multiplicative
      Model\nResiduals", ylab="Normalized Gamma Residuals",
      cex.lab=1.1, cex.axis=1.4, adj=0.5)

# FBP
res2 <- res[res>=-5] ; res.g<-res.g[res.g>=-5]
hist(res2, main="Multiplicative Model \n Residuals",
      cex.main=1.4, xlab="", ylab="", density=15, cex.lab=1,
      cex.axis=1.4, adj=0.5)
par(new=T)
x<-seq(from=range(res2)[1], to=range(res2)[2], length.out=
      1000)
plot(x, dnorm(x, mean=0, sd=1), xlab="", ylab="", axes=F, main=
      "", type="l", col=2, lwd=2)

#qqplot(res.g, res2, pch=20, cex=0.8, main="", xlab=
#      "Multiplicative Model\nResiduals", ylab="Normalized
#      Gamma Residuals", cex.lab=1.1, cex.axis=1.4, adj=0.5)

x1pix=5.46875; x2pix=x1pix ; x3pix=3.27
zp= (zp/x3pix-min(zp)/x3pix )+1
xp= (xp/x1pix-min(xp)/x1pix )+1
yp= (yp/x1pix-min(yp)/x1pix )+1
t=tp*0 ; nd=length(tme)
for(i in 1:nd) { t[tp==tme[i]]=i } ; tp=t

x=as.integer(xp) ; y=as.integer(yp)
z=as.integer(zp) ; t=as.integer(tp)

# Save residuals and corresponding index as data frame
dataIR<-data.frame(x=c(x), y=c(y), z=c(z), res, t=c(t))
save(dataIR, file="dataIR.Rdata")

#dataFBP<-data.frame(x=c(x), y=c(y), z=c(z), res.n, t=c(t))
#save(dataFBP, file="dataFBP.Rdata")
```

## B. R CODE

```
#####  
#-----Chapter 5 SAR Model-----#  
#####  
  
##Source subfunctions first - file name: "ACFfuns3D.txt"##  
SARsim3D=function(Amod, N, Nz)  
{  
  Aarray=array(0,dim = c(N,N,Nz))  
  Aarray[1:5,1:5,1:5]=Amod  
  omegalmat=matrix(rep(c(0:(N-1)),times=N),ncol=N)  
  omega2mat=t(omegalmat)  
  Aa=array(0,dim = c(N,N,Nz))  
  for(kkk in (1:Nz)){Aa[, , kkk] =  
    (omegalmat+omega2mat)+(kkk-1)}  
  omega=c(2*Aa*2*pi/N)  
  complexV=array(complex(length.out = 0, real =0,  
    imaginary =omega),dim=c(N,N,Nz))  
  Afft=fft(Aarray)*exp(complexV)  
  u=array(rnorm(n=N*N*Nz),dim=c(N,N,Nz))  
  xfft=fft(u)/Afft  
  xarray=Re(fft(xfft,inverse=t))/(N*N*Nz)  
  xarray  
}  
  
# Generate 3-D images with the specified autoregressive  
# structures  
AcfMod3Dcl=function(ax2,ax1,ay2,ay1,az2,az1,c1,c2, N, Nz)  
{  
  A3=matrix(0,ncol=5,nrow=5)  
  A3[1,3]=ay2;A3[2,3]=ay1;A3[3,3]=1;A3[4,3]=ay1;A3[5,3]=ay2  
  A3[3,1]=ax2; A3[3,2]= ax1;A3[3,4]=ax1;A3[3,5]=ax2  
  A3[2,2]=c1; A3[2,4]=c1;A3[4,2]=c1; A3[4,4]=c1  
  A2=matrix(0,ncol=5,nrow=5)  
  A2[2,3]= c2;A2[3,3]=az1;A2[4,3]=c2;  
  A2[3,2]= c2;A2[3,4]=c2;  
  A5=matrix(0,ncol=5,nrow=5)  
  A5[3,3]=az2
```

## B. R CODE

```
Amod=array(0,dim=c(5,5,5))
Amod[, , 3]=A3;Amod[, , 2]=A2;Amod[, , 4]=A2; Amod[, , 5]=A5
Amod[, , 1]=A5
Aarray=array(0,dim = c(N,N,Nz))
Aarray[1:5,1:5, 1:5]=Amod

fftimage <- fft(Aarray)
congfft <- Conj(fftimage)
ans1 <- fftimage * congfft
pans=Re(ans1)
npans1=pans[c((N/2):2,1:(N/2)), , ]
npans2=npans1[,c((N/2):2,1:(N/2)), ]
npans3=npans2[, , c(ceiling(Nz/2):2,1:ceiling(Nz/2))]
N=dim(npans3)[1]
omegalmat=matrix(rep(c(0:(N-1))),times=N),ncol=N)
omega2mat=t(omegalmat)
Aa=array(0,dim = c(N,N,Nz))
for ( kkk in (1:Nz)){
Aa[, , kkk]= (omegalmat+omega2mat)+(kkk-1) }
omega=c(-(N-1)/2)*Aa*2*pi/N)
complexV=array(complex(length.out = 0, real =0,
                        imaginary =omega),dim=c(N,N,Nz))
Afft=fft(1./npans3,inverse=T)*exp(complexV)
Acfarray=Re(Afft)
Acfarray=Acfarray/Acfarray[1,1,1]
acf=rotation3d(Acfarray,N,Nz)
acf[m]
}

rotation <- function(m) {
if(is.integer(dim(m)[1]/2)){
  dims <- dim(m)
  m1 <- cbind(m[, (dims[2]/2+1):dims[2]],m[,1:(dims[2]/2)])
  rbind(m1[(dims[1]/2+1):dims[1],],m1[1:(dims[1]/2),])
}
else {
  dims <- dim(m)
```

## B. R CODE

```

    m1 <- cbind(m[, (ceiling(dims[2]/2)+1):dims[2]],
               m[, 1:(ceiling(dims[2]/2))])
    rbind(m1[(ceiling(dims[1]/2+1)):dims[1],],
          m1[1:(ceiling(dims[1]/2)),])
  }
}

rotation3d<-function(acf,nxy,nz){
acf0=acf
for(i in 1:nz){
acf0[, ,i]=rotation(acf[, ,i])
}
acf00=acf
z=ceiling(nz/2)
acf00[, ,1:z]=acf0[, ,z:1]
acf00[, , (z+1):nz]=acf0[, ,nz:(z+1)]
acf1=acf00
if(nxy%%2==0) {acf1=acf00[2:nxy,2:nxy,]}
if(nz%%2==0) {acf1=acf1[, ,1:(nz-1)]}
acf1
}

iacf <- function(image,flag){
fftimage <- fft(image)
congfft <- Conj(fftimage)
ans1 <- fftimage * congfft
ans2 <- Re(fft(ans1, inverse=TRUE))
if(flag=="1D") {acf <- ans2/ans2[1]}
if(flag=="2D") {acf <- ans2/ans2[1,1]}
if(flag=="3D") {acf <- ans2/ans2[1,1,1]}
acf
}

#####END SUBFUNCTIONS#####

# number of lags
n1=n2=n3=seq(-2,2,by=1)
count=0;ind=NULL

```

## B. R CODE

```
for(i in 1:5){
  for(j in 1:5){
    for(k in 1:5){
      if((abs(n1[i])+abs(n2[j])+abs(n3[k]))<=2) {
        count=count+1
        ind=rbind(ind,c(n1[i],n2[j],n3[k]))}
      }
    }
  }
  ind=ind[c(1:12,14:25),]

  dl=l=ll=NULL
  for(i in 1:24){
    for(j in 1:24){
      dl=rbind(dl,ind[i,]-ind[j,])
      l=rbind(l,ind[i,])
      ll=rbind(ll,ind[j,])
    }
  }
  udl=unique(dl)
  factor=apply(dl,1,as.vector)

  library(dplyr)

  match=plyr::count(dl, names(dl))

  freq= match
  for(i in 1:129){
    for(j in 1:129){
      if(all(udl[i,]==as.vector(match[j,1:3]))) freq[i,]=match[j,]
    }
  }
  lfreq=freq
  l0=l[!duplicated(dl),];ll0=ll[!duplicated(dl),]

  fftimage <- fft(xarray)
  congfft <- Conj(fftimage)
  ans1 <- fftimage * congfft
  ans2 <- Re(fft(ans1, inverse=TRUE))/(N*N*Nz)
```



## B. R CODE

```
ans = ans2/ans2[1,1,1]
acf=rotation3d(ans,30,45) #acf[15,15,23]=1
m=cbind(udl[,1]+15,udl[,2]+15,udl[,3]+23) # Find index
cl=acf[m]

source("ACFfuns3D.txt")
acfl=AcfMod3Dcl(ax2,ax1,ay2,ay1,az2,az1,c1,c2,N,Nz)
wr=lfreq[,4] # weights

nlsobj1=nls(cl~AcfMod3Dcl(ax2,ax1,ay2,ay1,az2,az1,c1,c2,N,Nz),
            control=list(tol=1e-5,minFactor=0.000000176562),
            start=list(ax2=0.015,ax1=-0.2,ay2=0.014,ay1=-0.2,
            az2=0.04,az1=-0.2,c1=0.02,c2=0.037),
            weights=sqrt(wr))

# Compute the model residuals

ax1=coef(nlsobj)[1]; ax2=coef(nlsobj)[2]
ay1=coef(nlsobj)[3]; ay2=coef(nlsobj)[4]

az1=coef(nlsobj)[5];az2=coef(nlsobj)[6]
c1=coef(nlsobj)[7];c2=coef(nlsobj)[8]

A3=matrix(0,ncol=5,nrow=5)
A3[1,3]=ay2; A3[2,3]= ay1;A3[3,3]=1;A3[4,3]=ay1;A3[5,3]=ay2
A3[3,1]=ax2; A3[3,2]= ax1;A3[3,4]=ax1;A3[3,5]=ax2
A3[2,2]=c1; A3[2,4]= c1;A3[4,2]=c1;A3[4,4]=c1

A2=matrix(0,ncol=5,nrow=5)
A2[3,3]=az1
A2[2,3]=c2; A2[4,3]= c2;A2[3,2]=c2;A2[3,4]=c2

A5=matrix(0,ncol=5,nrow=5)
A5[3,3]=az2

Amod=array(0,dim=c(5,5,5))
```

## B. R CODE

```
Amod[, , 3]=A3;Amod[, , 2]=A2;Amod[, , 4]=A2;  
Amod[, , 5]=A5; Amod[, , 1]=A5;
```

```
resiarrray=xarray
```

```
for ( ix in (3:(N-2))) {  
  for ( iy in (3:(N-2))) {  
    for ( iz in (3:(Nz-2))) {  
      resival=0.0  
      for ( lx in (-2:2))  
        {for (ly in (-2:2))  
          { for (lz in (-2:2))  
            {  
              resival=resival+Amod[lx+3,ly+3,lz+3]*  
                xarray[ix-lx,iy-ly,iz-lz]  
            }  
          }  
        }  
      resiarrray[ix,iy,iz]=resival  
    }  
  }  
}
```

```
acf=iacf(resiarrray[3:(N-2),3:(N-2),3:(Nz-2)],"3D")  
racf=rotation3d(acf,dim(acf)[1],dim(acf)[3])
```

```
# Figure 5.8 bottom
```

```
par(mfrow=c(2,3),font=2,font.axis=2,font.lab=2)
```

```
ci=1.96/sqrt(N*N*Nz)
```

```
nx=ceiling(N/2)-2;nz=ceiling(Nz/2)-2
```

```
plot(c(0:12),racf[,nx,nz][nx:length(racf[,nx,nz])],  
      type="o",lty=2,col=4,pch=20,ylab="3-D ACF",xlab=  
      "x-lag",main="Horizontal")
```

```
abline(h=c(ci,-ci),col="grey",lty=3)
```

```
legend("topright",legend=c("Residuals"),col=4,lty=2,pch=20)
```

```
plot(c(0:12),racf[nx,,nz][nx:length(racf[nx,,nz])],  
      type="o",lty=2,col=2,pch=20,ylab="3-D ACF",xlab=
```

```

      "y-lag",main="Vertical")
abline(h=c(ci,-ci),col="grey",lty=3)
legend("topright",legend=c("Residuals"),col=2,lty=2,pch=20)
plot(c(0:20),racf[nx,nx,][nz:length(racf[nx,nx,])],
      type="o",lty=2,col=3,pch=20,ylab="3-D ACF",xlab=
      "z-lag",main="Axial")
abline(h=c(ci,-ci),col="grey",lty=3)
legend("topright",legend=c("Residuals"),col=3,lty=2,pch=20)

```

# Nomenclature

<i>iid</i>	Independent and Identically Distributed
1-D	One Dimension/Dimensional
2-D	Two Dimension/Dimensional
3-D	Three Dimension/Dimensional
ACF	Auto-correlation Function
ACRIN	American College of Radiology Imaging Network
AR	Auto-regressive
ASIRT	Additive Simultaneous Iterative Reconstruction Technique
CQIE	Centres for Quantitative Imaging Excellence
CT	Computed Tomography
CUH	Cork University Hospital
ECG	Electrocardiography
EEG	Electroencephalography
EM	Expectation-Maximisation
FBP	Filtered Back-projection
FDG	Fluorodeoxyglucose
FFT	Fast Fourier Transform
fMRI	functional Magnetic Resonance Imaging
FOV	Field of View

GE	General Electric
GLM	Generalised Linear Models
IR	Iterative Reconstruction/Reconstructed
IRLS	Iterative Re-weighted Least Squares
LOR	Line of Response
LS	Least Squares
LSA	Least Squares Autoregression
LSO	Lutetium Oxyorthosilicate
ML	Maximum Likelihood
ML-EM	Maximum Likelihood Expectation Maximisation
MLE	Maximum Likelihood Estimate
MRI	Magnetic Resonance Imaging
MSE	Mean Squared Error
NCI	National Cancer Institute
NLS	Non-linear Least Squares
OLS	Ordinary Least Squares
OSEM	Ordered Subset Expectation-Maximisation
PET	Positron Emission Tomography
Q-Q	Quantile-Quantile
QA	Quality Assurance
QC	Quality Control
RAMLA	Row-Action Maximum Likelihood Algorithm
ROI	Region of Interest
SAR	Spatial Auto-regressive

SNR Signal-to-noise Ratio

SPECT Single Photon Emission Computed Tomography

UCC University College Cork

VSK Vardi-Shepp-Kaufman

# Bibliography

- [1] M. Abramowitz and I. A. Stegun, *Handbook of mathematical functions: with formulas, graphs, and mathematical tables*. Courier Corporation, 1964, vol. 55.
- [2] N. Alpert, D. Chesler, J. Correia, R. Ackerman, J. Chang, S. Finklestein, S. Davis, G. Brownell, and J. Taveras, “Estimation of the local statistical noise in emission computed tomography,” *IEEE transactions on medical imaging*, vol. 1, no. 2, pp. 142–146, 1982.
- [3] H. Alzer, “On some inequalities for the Gamma and Psi functions,” *Mathematics of Computation of the American Mathematical Society*, vol. 66, no. 217, pp. 373–389, Jan. 1997.
- [4] C. D. Anderson, “The positive electron,” *Phys. Rev.*, vol. 43, pp. 491–494, Mar 1933. [Online]. Available: <https://link.aps.org/doi/10.1103/PhysRev.43.491>
- [5] M.-J. Antoine, J.-M. Travère, and D. Bloyet, “Modeling of 2D PET noise autocovariance function applied to individual activation studies,” in *Nuclear Science Symposium and Medical Imaging Conference, 1994., 1994 IEEE Conference Record*, vol. 4. IEEE, 1994, pp. 1628–1632.
- [6] E. Artin, *The Gamma Function*, ser. Athena Series : Selected Topics in Mathematics. New York, NY, USA: Holt, Rinehart and Winston, 1964.
- [7] H. H. Barrett, D. W. Wilson, and B. M. Tsui, “Noise properties of the EM algorithm. I. Theory,” *Physics in medicine and biology*, vol. 39, no. 5, pp. 833–846, 1994.
- [8] M. Bergström, C. Bohm, K. Ericson, L. Eriksson, and J. Litton, “Corrections for attenuation, scattered radiation, and random coincidences in a ring detector positron emission transaxial tomograph,” *IEEE Transactions on Nuclear Science*, vol. 27, no. 1, pp. 549–554, 1980.

- [9] T. Beyer, D. W. Townsend, T. Brun, P. E. Kinahan *et al.*, “A combined PET/CT scanner for clinical oncology,” *The Journal of nuclear medicine*, vol. 41, no. 8, p. 1369, 2000.
- [10] C. Bohm, L. Eriksson, M. Bergstrom, J. Litton, R. Sundman, and M. Singh, “A computer assisted ringdetector positron camera system for reconstruction tomography of the brain,” *IEEE Transactions on Nuclear Science*, vol. 25, no. 1, pp. 624–637, 1978.
- [11] G. E. Box, G. M. Jenkins, G. C. Reinsel, and G. M. Ljung, *Time series analysis: forecasting and control*. John Wiley & Sons, 2015.
- [12] B. F. Branstetter IV, T. M. Blodgett, L. A. Zimmer, C. H. Snyderman, J. T. Johnson, S. Raman, and C. C. Meltzer, “Head and neck malignancy: Is PET/CT more accurate than PET or CT alone?” *Radiology*, vol. 235, no. 2, pp. 580–586, 2005.
- [13] L. Breiman, “The  $\Pi$  method for estimating multivariate functions from noisy data,” *Technometrics*, vol. 33, no. 2, pp. 125–143, May 1991.
- [14] D. J. Brenner and E. J. Hall, “Computed tomography—an increasing source of radiation exposure,” *New England Journal of Medicine*, vol. 357, no. 22, pp. 2277–2284, 2007.
- [15] P. J. Brockwell and R. A. Davis, *Time Series: Theory and Methods*. New York, NY, USA: Springer, 1991.
- [16] A. K. Buck, K. Herrmann, T. Stargardt, T. Dechow, B. J. Krause, and J. Schreyögg, “Economic evaluation of PET and PET/CT in oncology: evidence and methodologic approaches,” *Journal of nuclear medicine technology*, vol. 38, no. 1, pp. 6–17, 2010.
- [17] C. Burnham, J. Bradshaw, D. Kaufman, D. Chesler, and G. Brownell, “Positron source position sensing detector and electronics,” Jul. 23 1985, uS Patent 4,531,058. [Online]. Available: <https://www.google.com/patents/US4531058>
- [18] I. Buvat, “A non-parametric bootstrap approach for analysing the statistical properties of SPECT and PET images,” *Physics in medicine and biology*, vol. 47, no. 10, pp. 1761–1775, 2002.



- [19] R. E. Carson, Y. Yan, M. E. Daube-Witherspoon, N. Freedman, S. L. Bacharach, and P. Herscovitch, "An approximation formula for the variance of PET region-of-interest values," *IEEE transactions on medical imaging*, vol. 12, no. 2, pp. 240–250, Jun. 1993.
- [20] M. Casey and R. Nutt, "A multicrystal two dimensional BGO detector system for positron emission tomography," *IEEE transactions on nuclear science*, vol. 33, no. 1, pp. 460–463, 1986.
- [21] A. F. Chatziioannou, S. R. Cherry, Y. Shao, R. W. Silverman, K. Meadors, T. H. Farquhar, M. Pedarsani, and M. E. Phelps, "Performance evaluation of microPET," *Journal of Nuclear Medicine*, vol. 40, no. 7, pp. 1164–1175, 1999.
- [22] Y. Chen, R. Chen, X. Zhou, J. Liu, and G. Huang, "Report on the development and application of PET/CT in mainland China." *Oncotarget*, 2017.
- [23] T. Cheng and B. Anbaroglu, "Methods on defining spatio-temporal neighbourhoods," in *The 10th International Conference of GeoComputation*, Sydney, Australia, Nov 30th–Dec 2nd 2009.
- [24] D. A. Chesler, "Three-dimensional activity distribution from multiple positron scintigraphys," *Journal of nuclear medicine*, vol. 12, pp. 347–348, 1971.
- [25] D. A. Chesler, B. Hoop, and G. L. Brownell, "Transverse section imaging of myocardium with  $^{13}\text{NH}_4$ ," in *Journal of Nuclear Medicine*, vol. 14, no. 8, 1973, pp. 623–623.
- [26] D. A. Chesler, "Positron tomography and three-dimensional reconstruction technique," in *Proc. Symp. on Tomographic Proc. Symp. on Tomographic Imaging in Nuclear Medicine*. New York: Society of Nuclear Medicine, 1973, pp. 176–183.
- [27] A. P. Dempster, N. M. Laird, and D. B. Rubin, "Maximum likelihood from incomplete data via the EM algorithm," *Journal of the royal statistical society. Series B (methodological)*, vol. 39, pp. 1–38, 1977.
- [28] A. J. Einstein, M. J. Henzlova, and S. Rajagopalan, "Estimating risk of cancer associated with radiation exposure from 64-slice computed tomography coronary angiography," *Jama*, vol. 298, no. 3, pp. 317–323, 2007.

- [29] Eurostat, “Healthcare resource statistics—technical resources and medical technology,” [http://ec.europa.eu/eurostat/statistics-explained/index.php/Healthcare\\_resource\\_statistics\\_-\\_technical\\_resources\\_and\\_medical\\_technology](http://ec.europa.eu/eurostat/statistics-explained/index.php/Healthcare_resource_statistics_-_technical_resources_and_medical_technology), 2016.
- [30] K. Faulkner and B. Moores, “Noise and contrast detection in computed tomography images,” *Physics in medicine and biology*, vol. 29, no. 4, p. 329, 1984.
- [31] A. G. Filler, “The history, development and impact of computed imaging in neurological diagnosis and neurosurgery: CT, MRI, and DTI,” *Internet Journal of Neurosurgery*, vol. 7, no. 1, p. 5, 2010.
- [32] H. L. Fred, “Drawbacks and limitations of computed tomography: views from a medical educator,” *Texas Heart Institute Journal*, vol. 31, no. 4, p. 345, 2004.
- [33] H. Friebolin and J. K. Becconsall, *Basic one-and two-dimensional NMR spectroscopy*. VCH Weinheim, 1993.
- [34] A. E. Gelfand, P. Diggle, P. Guttorp, and M. Fuentes, *Handbook of spatial statistics*. Boca Raton, Florida, US: Chapman Hall/CRC Press,, 2010.
- [35] P. J. Green, “Iteratively reweighted least squares for maximum likelihood estimation, and some robust and resistant alternatives,” *Journal of the Royal Statistical Society. Series B (Methodological)*, vol. 46, no. 2, pp. 149–192, 1984.
- [36] X. Guyon, “Parameter estimation for a stationary process on ad-dimensional lattice,” *Biometrika*, vol. 69, no. 1, pp. 95–105, 1982.
- [37] D. Hawe, “Statistical considerations in the kinetic analysis of PET-FDG brain tumour studies,” Ph.D. dissertation, University College Cork, 2016.
- [38] R. E. Henkin, *Nuclear medicine*, 2nd ed. Elsevier Mosby, 2006.
- [39] C. Heyde and R. Gay, “Smoothed periodogram asymptotics and estimation for processes and fields with possible long-range dependence,” *Stochastic Processes and their Applications*, vol. 45, no. 1, pp. 169–182, 1993.
- [40] J. Holden, J. Halama, and B. Hasegawa, “The propagation of stochastic pixel noise into magnitude and phase values in the fourier analysis of digital images,” *Physics in medicine and biology*, vol. 31, no. 4, p. 383, 1986.

- [41] A. Houghton and D. Gray, *Making sense of the ECG: a hands-on guide*. CRC Press, 2014.
- [42] G. N. Hounsfield, “Computerized transverse axial scanning (tomography): Part 1. description of system,” *The British journal of radiology*, vol. 46, no. 552, pp. 1016–1022, 1973.
- [43] H. Hricak, B. I. Choi, A. M. Scott, K. Sugimura, A. Muellner, G. K. von Schulthess, M. F. Reiser, M. M. Graham, N. R. Dunnick, and S. M. Larson, “Global trends in hybrid imaging,” *Radiology*, vol. 257, no. 2, pp. 498–506, 2010.
- [44] B. Huang, M. W.-M. Law, and P.-L. Khong, “Whole-body PET/CT scanning: estimation of radiation dose and cancer risk,” *Radiology*, vol. 251, no. 1, pp. 166–174, 2009.
- [45] H. M. Hudson and R. S. Larkin, “Accelerated image reconstruction using ordered subsets of projection data,” *IEEE transactions on medical imaging*, vol. 13, no. 4, pp. 601–609, 1994.
- [46] R. Huesman, “The effects of a finite number of projection angles and finite lateral sampling of projections on the propagation of statistical errors in transverse section reconstruction,” *Physics in Medicine and Biology*, vol. 22, no. 3, pp. 511–521, 1977.
- [47] R. H. Huesman, “A new fast algorithm for the evaluation of regions of interest and statistical uncertainty in computed tomography,” *Physics in Medicine and Biology*, vol. 29, no. 5, pp. 543–552, 1984.
- [48] S. A. Huettel, A. W. Song, and G. McCarthy, *Functional magnetic resonance imaging*. Sinauer Associates Sunderland, 2004, vol. 1.
- [49] G. J. Husak, J. Michaelsen, and C. Funk, “Use of the gamma distribution to represent monthly rainfall in africa for drought monitoring applications,” *International Journal of Climatology*, vol. 27, no. 7, pp. 935–944, 2007.
- [50] M. Ibaraki, K. Matsubara, K. Nakamura, H. Yamaguchi, and T. Kinoshita, “Bootstrap methods for estimating PET image noise: experimental validation and an application to evaluation of image reconstruction algorithms,” *Annals of nuclear medicine*, vol. 28, no. 2, pp. 172–182, Feb. 2014.

- [51] INTERNATIONAL ATOMIC ENERGY AGENCY, *Quality Assurance for PET and PET/CT Systems*, ser. IAEA Human Health Series. Vienna: INTERNATIONAL ATOMIC ENERGY AGENCY, 2009, no. 1. [Online]. Available: <http://www-pub.iaea.org/books/IAEABooks/8002/Quality-Assurance-for-PET-and-PET-CT-Systems>
- [52] H. Jadvar and P. M. Colletti, “Competitive advantage of PET/MRI,” *European journal of radiology*, vol. 83, no. 1, pp. 84–94, 2014.
- [53] S. M. Kim, A. M. Alessio, B. De Man, and P. E. Kinahan, “Direct reconstruction of CT-based attenuation correction images for PET with cluster-based penalties,” *IEEE Transactions on Nuclear Science*, vol. 64, no. 3, pp. 959–968, 2017.
- [54] P. E. Kinahan and J. W. Fletcher, “Positron emission tomography-computed tomography standardized uptake values in clinical practice and assessing response to therapy,” in *Seminars in Ultrasound, CT and MRI*, vol. 31, no. 6. Elsevier, Dec. 2010, pp. 496–505.
- [55] P. E. Kinahan, D. W. Townsend, T. Beyer, and D. Sashin, “Attenuation correction for a combined 3D PET/CT scanner,” *Medical physics*, vol. 25, no. 10, pp. 2046–2053, 1998.
- [56] D. E. Kuhl and R. Q. Edwards, “Image separation radioisotope scanning,” *Radiology*, vol. 80, no. 4, pp. 653–662, 1963.
- [57] D. Kundu and A. Manglick, “Discriminating between the log-normal and gamma distributions,” *Journal of the Applied Statistical Sciences*, vol. 14, pp. 175–187, 2005.
- [58] C. S. Levin and E. J. Hoffman, “Calculation of positron range and its effect on the fundamental limit of positron emission tomography system spatial resolution,” *Phys. Med. Biol*, vol. 44, pp. 781–799, 1999.
- [59] Y. Li, “Noise propagation for iterative penalized-likelihood image reconstruction based on Fisher information,” *Physics in medicine and biology*, vol. 56, no. 4, pp. 1083–1103, 2011. [Online]. Available: <http://stacks.iop.org/0031-9155/56/i=4/a=013>
- [60] Z. Li and P. S. Conti, “Radiopharmaceutical chemistry for positron emission tomography,” *Advanced drug delivery reviews*, vol. 62, no. 11, pp. 1031–1051, 2010.

- [61] A. M. Loening and S. S. Gambhir, “Amide: a free software tool for multimodality medical image analysis,” *Molecular imaging*, vol. 2, no. 3, pp. 131–137, 2003.
- [62] R. Maitra and F. O’sullivan, “Variability assessment in positron emission tomography and related generalized deconvolution models,” *Journal of the American Statistical Association*, vol. 93, no. 444, pp. 1340–1355, Dec. 1998.
- [63] D. A. Mankoff, M. Muzi, and H. Zaidi, “Quantitative analysis in nuclear oncologic imaging,” in *Quantitative analysis in nuclear medicine imaging*. New York, NY, USA: Springer, 2006, pp. 494–536.
- [64] G. Mariani, L. Bruselli, T. Kuwert, E. E. Kim, A. Flotats, O. Israel, M. Dondi, and N. Watanabe, “A review on the clinical uses of SPECT/CT,” *European journal of nuclear medicine and molecular imaging*, vol. 37, no. 10, pp. 1959–1985, 2010.
- [65] P. McCullagh and J. A. Nelder, *Generalized Linear Models*, 2nd ed. London, UK: CRC Press, 1989.
- [66] D. L. Miglioretti, E. Johnson, A. Williams, R. T. Greenlee, S. Weinmann, L. I. Solberg, H. S. Feigelson, D. Roblin, M. J. Flynn, N. Vanneman *et al.*, “The use of computed tomography in pediatrics and the associated radiation exposure and estimated cancer risk,” *JAMA pediatrics*, vol. 167, no. 8, pp. 700–707, 2013.
- [67] J. Miller and *et. al.*, “Earliest known uses of some of the words of mathematics,” 2017. [Online]. Available: <http://jeff560.tripod.com/g.html>
- [68] P. W. Miller, N. J. Long, R. Vilar, and A. D. Gee, “Synthesis of  $^{11}\text{C}$ ,  $^{18}\text{F}$ ,  $^{15}\text{O}$ , and  $^{13}\text{N}$  radiolabels for positron emission tomography,” *Angewandte Chemie International Edition*, vol. 47, no. 47, pp. 8998–9033, 2008.
- [69] J. Mohapl, “On maximum likelihood estimation for Gaussian spatial autoregression models,” *Annals of the Institute of Statistical Mathematics*, vol. 50, no. 1, pp. 165–186, 1998.
- [70] T. Mou, J. Huang, and F. O’Sullivan, “The gamma characteristic of reconstructed pet images: Implications for roi analysis,” *IEEE Transactions on Medical Imaging*, vol. 37, no. 5, pp. 1092–1102, May 2018.

- [71] T. Mou, J. Huang, Y. Zhang, B. Elston, P. Kinahan, M. Muzi, A. Opanowski, and F. O’Sullivan, “Spatial covariance characteristics in a collection of 3-D PET scanners used in clinical imaging trials,” in *Nuclear Science Symposium and Medical Imaging Conference (NSS/MIC)*, 2014 IEEE. Seattle, WA USA: IEEE, Nov. 2014, pp. M10–22.
- [72] T. Mou, J. Huang, Y. Zhang, P. Kinahan, and F. O’Sullivan, “An improved statistical approach to the estimation of spatial bias and variability in reconstructed PET data,” in *2015 IEEE Nuclear Science Symposium and Medical Imaging Conference (NSS/MIC)*, San Diego, CA 92108, USA, Oct. 2015, pp. 1–3.
- [73] K. Mullinger and R. Bowtell, “Combining EEG and fMRI,” *Magnetic Resonance Neuroimaging: Methods and Protocols*, pp. 303–326, 2011.
- [74] K. Myers, H. Barrett, M. Borgstrom, D. Patton, and G. Seeley, “Effect of noise correlation on detectability of disk signals in medical imaging,” *Journal of Optical Society of America A*, vol. 2, no. 10, pp. 1752–1759, 1985.
- [75] E. Niedermeyer and F. L. da Silva, *Electroencephalography: basic principles, clinical applications, and related fields*. Lippincott Williams & Wilkins, 2005.
- [76] M. Normandin, R. Koeppe, and E. Morris, “Selection of weighting factors for quantification of PET radioligand binding using simplified reference tissue models with noisy input functions,” *Physics in medicine and biology*, vol. 57, no. 3, pp. 609–629, 2012.
- [77] R. Nutt, “The history of positron emission tomography,” *Molecular Imaging & Biology*, vol. 4, no. 1, pp. 11–26, 2002.
- [78] S. Ogawa, T.-M. Lee, A. S. Nayak, and P. Glynn, “Oxygenation-sensitive contrast in magnetic resonance image of rodent brain at high magnetic fields,” *Magnetic resonance in medicine*, vol. 14, no. 1, pp. 68–78, 1990.
- [79] J. M. Ollinger and J. A. Fessler, “Positron-Emission Tomography,” *IEEE Signal Processing Magazine*, vol. 14, no. 1, pp. 43–55, Jan 1997.
- [80] F. O’Sullivan, Y. Pawitan, and D. Haynor, “Reducing negativity artifacts in emission tomography: post-processing filtered backprojection solutions,” *IEEE transactions on medical imaging*, vol. 12, no. 4, pp. 653–663, 1993.

- [81] S. Pajevic, M. E. Daube-Witherspoon, S. L. Bacharach, and R. E. Carson, "Noise characteristics of 3-D and 2-D PET images," *IEEE transactions on medical imaging*, vol. 17, no. 1, pp. 9–23, Feb. 1998.
- [82] W. D. Penny and K. J. Friston, "Functional imaging," *Scholarpedia*, vol. 2, no. 5, p. 1478, 2007, revision #91281.
- [83] M. Phelps, E. Hoffman, N. Mullani, and M. Ter-Pogossian, "Application of annihilation coincidence detection to transaxial reconstruction tomography." *Journal of nuclear medicine: official publication, Society of Nuclear Medicine*, vol. 16, no. 3, pp. 210–224, 1975.
- [84] M. E. Phelps, E. J. Hoffman, N. A. Mullani, C. S. Higgins, and M. M. Ter Pogossian, "Design considerations for a positron emission transaxial tomograph (PETT III)," *IEEE Transactions on Nuclear Science*, vol. 23, no. 1, pp. 516–522, 1976.
- [85] J. Qi and R. M. Leahy, "Resolution and noise properties of map reconstruction for fully 3-d pet," *IEEE transactions on medical imaging*, vol. 19, no. 5, pp. 493–506, 2000.
- [86] R Core Team, *R: A Language and Environment for Statistical Computing*, R Foundation for Statistical Computing, Vienna, Austria, 2013. [Online]. Available: <http://www.R-project.org/>
- [87] C. R. Rao, *Linear statistical inference and its applications*. New York, NY, USA: John Wiley & Sons, 1973.
- [88] P. Razifar, "Novel approaches for application of principal component analysis on dynamic PET images for improvement of image quality and clinical diagnosis," Ph.D. dissertation, Acta Universitatis Upsaliensis, 2005.
- [89] P. Razifar, M. Lubberink, H. Schneider, B. Långström, E. Bengtsson, and M. Bergström, "Non-isotropic noise correlation in pet data reconstructed by fbp but not by osem demonstrated using auto-correlation function," *BMC medical imaging*, vol. 5, no. 1, p. 3, 2005.
- [90] C. Riddell, R. E. Carson, J. A. Carrasquillo, S. K. Libutti, D. N. Danforth, M. Whatley, and S. L. Bacharach, "Noise reduction in oncology FDG PET images by iterative reconstruction: a quantitative assessment," *Journal of Nuclear Medicine*, vol. 42, no. 9, pp. 1316–1323, 2001.

- [91] P. Ritter and A. Villringer, “Simultaneous EEG-fMRI,” *Neuroscience & Biobehavioral Reviews*, vol. 30, no. 6, pp. 823–838, 2006.
- [92] C. Roobottom, G. Mitchell, and G. Morgan-Hughes, “Radiation-reduction strategies in cardiac computed tomographic angiography,” *Clinical radiology*, vol. 65, no. 11, pp. 859–867, 2010.
- [93] M. Rosen, P. E. Kinahan, J. F. Gimpel, A. Opanowski, B. A. Siegel, G. Hill, L. Weiss, and L. Shankar, “Performance observations of scanner qualification of NCI-designated cancer centers: Results from the centers of quantitative imaging excellence (CQIE) program,” *Academic Radiology*, vol. 24, no. 2, pp. 232–245, 2017.
- [94] M. Rosenblatt, *Stationary Sequences and Random Fields*. Birkhäuser Boston, 1985.
- [95] R. W. Rowe and S. Dai, “A pseudo-Poisson noise model for simulation of positron emission tomographic projection data,” *Medical physics*, vol. 19, no. 4, pp. 1113–1119, 1992.
- [96] G. B. Saha, *Basics of PET Imaging: Physics, Chemistry, and Regulations*, 2nd ed. Springer Science & Business Media, 2010.
- [97] C. Schabel, S. Gatidis, M. Bongers, F. Hüttig, G. Bier, J. Kupferschlaeger, F. Bamberg, C. la Fougère, K. Nikolaou, and C. Pfannenberger, “Improving CT-based PET attenuation correction in the vicinity of metal implants by an iterative metal artifact reduction algorithm of CT data and its comparison to dual-energy—based strategies: A phantom study,” *Investigative Radiology*, vol. 52, no. 1, pp. 61–65, 2017.
- [98] J. Scheuermann, A. Opanowski, J. Maffei, D. H. Thibeault, J. Karp, B. Siegel, M. Rosen, and P. Kinahan, “Qualification of NCI-designated comprehensive cancer centers for quantitative PET/CT imaging in clinical trials,” *Journal of Nuclear Medicine*, vol. 54, no. supplement 2, pp. 334–334, 2013.
- [99] J. S. Scheuermann, J. S. Reddin, A. Opanowski, P. E. Kinahan, B. A. Siegel, L. K. Shankar, and J. S. Karp, “Qualification of NCI-designated cancer centers for quantitative PET/CT imaging in clinical trials,” *Journal of Nuclear Medicine*, pp. jnumed–116, 2017.



- [100] J. S. Scheuermann, J. R. Saffer, J. S. Karp, A. M. Levering, and B. A. Siegel, “Qualification of PET scanners for use in multicenter cancer clinical trials: the American College of Radiology Imaging Network experience,” *Journal of Nuclear Medicine*, vol. 50, no. 7, pp. 1187–1193, 2009.
- [101] H.-P. W. Schlemmer, B. J. Pichler, M. Schmand, Z. Burbar, C. Michel, R. Ladebeck, K. Jattke, D. Townsend, C. Nahmias, P. K. Jacob *et al.*, “Simultaneous MR/PET imaging of the human brain: feasibility study,” *Radiology*, vol. 248, no. 3, pp. 1028–1035, 2008.
- [102] H. A. Schwarz, “Über ein flächen kleinsten flächeninhalts betreffendes problem der variationsrechnung,” *Acta Societatis Scientiarum Fennicae*, vol. XV: 318, 1888.
- [103] L. A. Shepp and Y. Vardi, “Maximum likelihood reconstruction for emission tomography,” *IEEE transactions on medical imaging*, vol. 1, no. 2, pp. 113–122, 1982.
- [104] R. H. Shumway and D. S. Stoffer, *Time series analysis and its applications: with R examples*. Springer Science & Business Media, 2010.
- [105] Y. Song, W. Cai, H. Huang, X. Wang, Y. Zhou, M. J. Fulham, and D. D. Feng, “Lesion detection and characterization with context driven approximation in thoracic fdg pet-ct images of nscl studies,” *IEEE transactions on medical imaging*, vol. 33, no. 2, pp. 408–421, 2014.
- [106] W. H. Sweet, “The uses of nuclear disintegration in the diagnosis and treatment of brain tumor,” *New England Journal of Medicine*, vol. 245, no. 23, pp. 875–878, 1951, pMID: 14882442. [Online]. Available: <http://dx.doi.org/10.1056/NEJM195112062452301>
- [107] E. Tanaka and H. Murayama, “Properties of statistical noise in positron emission tomography,” in *International Workshop on Physics and Engineering in Medical Imaging*. International Society for Optics and Photonics, 1982, pp. 158–164.
- [108] M. M. Ter-Pogossian, M. E. Phelps, E. J. Hoffman, and N. A. Mullani, “A positron-emission transaxial tomograph for nuclear imaging (PETT),” *Radiology*, vol. 114, no. 1, pp. 89–98, 1975, pMID: 1208874. [Online]. Available: <https://doi.org/10.1148/114.1.89>

- [109] A. Teymurazyan, T. Riauka, H.-S. Jans, and D. Robinson, “Properties of noise in positron emission tomography images reconstructed with filtered-backprojection and row-action maximum likelihood algorithm,” *Journal of digital imaging*, vol. 26, no. 3, pp. 447–456, 2013.
- [110] D. W. Townsend, “Multimodality imaging of structure and function,” *Physics in medicine and biology*, vol. 53, no. 4, p. R1, 2008.
- [111] D. W. Townsend and M. Defrise, “Image reconstruction methods in positron tomography,” CERN (European Organization for Nuclear Research), Geneva, Switzerland, Tech. Rep., 1993.
- [112] D. W. Townsend, “Combined positron emission tomography–computed tomography: the historical perspective,” in *Seminars in Ultrasound, CT and MRI*, vol. 29, no. 4. Elsevier, 2008, pp. 232–235.
- [113] D. W. Townsend, T. Beyer, and T. M. Blodgett, “PET/CT scanners: a hardware approach to image fusion,” *Seminars in nuclear medicine*, vol. 33, no. 3, pp. 193–204, 2003.
- [114] C. S. van der Vos, D. Koopman, S. Rijnsdorp, A. J. Arends, R. Boellaard, J. A. van Dalen, M. Lubberink, A. T. Willemsen, and E. P. Visser, “Quantification, improvement, and harmonization of small lesion detection with state-of-the-art pet,” *European journal of nuclear medicine and molecular imaging*, vol. 44, no. 1, pp. 4–16, 2017.
- [115] Y. Vardi, L. Shepp, and L. Kaufman, “A statistical model for positron emission tomography,” *Journal of the American statistical Association*, vol. 80, no. 389, pp. 8–20, 1985.
- [116] W. N. Venables and B. D. Ripley, *Modern applied statistics with S-PLUS*. Springer Science & Business Media, 2013. [Online]. Available: <http://www.stats.ox.ac.uk/pub/MASS4>
- [117] W. Wadsak and M. Mitterhauser, “Basics and principles of radiopharmaceuticals for PET/CT,” *European journal of radiology*, vol. 73, no. 3, pp. 461–469, 2010.
- [118] W. Wang and G. Gindi, “Noise analysis of map-em algorithms for emission tomography,” *Physics in Medicine and Biology*, vol. 42, no. 11, pp. 2215–2232, 1997.

- [119] C. E. Weatherburn, *A first course mathematical statistics*. Cambridge Univ. Press, 1949.
- [120] S. Weisberg, *Applied linear regression*. New York, NY, USA: John Wiley & Sons, 1985.
- [121] P. Whittle, “On stationary processes in the plane,” *Biometrika*, pp. 434–449, 1954.
- [122] D. W. Wilson, B. M. W. Tsui, and J. A. Terry, “Non-stationary noise characteristics for SPECT images,” in *Conference Record of the 1991 IEEE Nuclear Science Symposium and Medical Imaging Conference*, vol. 3, Nov 1991, pp. 1736–1740.
- [123] D. W. Wilson and B. M. Tsui, “Noise properties of filtered-backprojection and ML-EM reconstructed emission tomographic images,” *IEEE transactions on nuclear science*, vol. 40, no. 4, pp. 1198–1203, 1993.
- [124] D. W. Wilson, B. M. Tsui, and H. H. Barrett, “Noise properties of the EM algorithm. II. Monte Carlo simulations,” *Physics in medicine and biology*, vol. 39, no. 5, p. 847, 1994.
- [125] F. R. Wrenn, M. L. Good, and P. Handler, “The use of positron-emitting radioisotopes for the localization of brain tumors,” *Science*, vol. 113, no. 2940, pp. 525–527, 1951.
- [126] Q. Yao and P. J. Brockwell, “Gaussian maximum likelihood estimation for ARMA models II: spatial processes,” *Bernoulli*, vol. 12, no. 3, pp. 403–429, 2006.
- [127] Z. Yin and R. Collins, “Belief propagation in a 3d spatio-temporal mrf for moving object detection,” in *IEEE Conference on Computer Vision and Pattern Recognition*. IEEE, 2007, pp. 1–8.
- [128] H. Zaidi, Ed., *Quantitative Analysis in Nuclear Medicine Imaging*. Springer US, 2006.
- [129] P. Zanzonico, “Routine quality control of clinical nuclear medicine instrumentation: a brief review,” *Journal of Nuclear Medicine*, vol. 49, no. 7, pp. 1114–1131, 2008.